PLASMA FLOW VELOCITY MEASUREMENTS WITH A GUNDESTRUP PROBE IN THE STOR-M TOKAMAK

A Thesis Submitted to the College of
Graduate Studies and Research
In Partial Fulfillment of the Requirements
For the Degree of Master of Science
In the
Department of Physics and Engineering Physics
University of Saskatchewan
Saskatoon

By
Geoffrey Martin Reginald St. Germaine
Saskatoon, Saskatchewan
Canada

In presenting this thesis in partial fulfilment of the requirements for a Postgraduate degree from the University of Saskatchewan, I agree that the Libraries of this University may make it freely available for inspection. I further agree that permission for copying of this thesis in any manner, in whole or in part, for scholarly purposes may be granted by the professor or professors who supervised my thesis work or, in their absence, by the Head of the Department or the Dean of the College in which my thesis work was done. It is understood that any copying or publication or use of this thesis or parts thereof for financial gain shall not be allowed without my written permission. It is also understood that due recognition shall be given to me and to the University of Saskatchewan in any scholarly use which may be made of any material in my thesis.

Requests for permission to copy or to make other use of material in this thesis in whole or part should be addressed to:

Head of the Department of Physics and Engineering Physics
116 Science Place
University of Saskatchewan
Saskatoon, Saskatchewan
Canada
S7N 5E2

Dedicated to

Sarah

Abstract

The profile of the poloidal velocity in the edge region of tokamak plasmas has been identified as playing a major role in the confinement of particles and energy. It has been suggested that a strongly sheared poloidal flow can reduce particle and energy losses by the stabilization of unstable modes and decorrelation of turbulence the edge region of the plasma. A Gundestrup probe, a Mach probe array, is used to measure both the parallel and perpendicular flow velocities in the Saskatchewan Torus-Modified (STOR-M) tokamak during several discharge conditions. It is observed that during Ohmic discharges there is no velocity shear and the direction of the parallel flow is independent of the direction of the toroidal magnetic field. During H-mode induced by a turbulent heating current pulse, a region of strong velocity shear develops in the plasma edge and an edge transport barrier develops. This results in a short period of improved particle and energy confinement with reduced fluctuation amplitudes. During electrode biasing experiments, a stainless steel biasing electrode is inserted into the plasma up to r = 82 mm and biased to +500 V relative to the vacuum chamber. It is observed that the particle confinement improves during the biasing phase while the energy confinement is degraded. A region of weak shear in the poloidal flow is observed in the plasma scrape-off layer (SOL). The results from STOR-M are compared with results from data taken in the Czech Academy of Sciences Torus (CASTOR) tokamak during both Ohmic discharges and discharges with electrode biasing.

Acknowledgements

I would like to express thanks to Prof. A. Hirose for guidance and support during this work. I am in debt to Dr. A. Singh for many hours of technical assistance and his invaluable thoughts and comments on these experiments. Additionally, the assistance of Prof. C. Xiao on many technical matters was greatly appreciated. I am also indebted to Prof. C. Boucher for his work in arranging for the manufacture Gundestrup probe for STOR-M and for many hours of discussion via video conferencing from INRS-EMT in Varennes, QC. I would also like to thank Dr. J. Stöckel, head of the Tokamak Department in the Institute of Plasma Physics of the Academy of Sciences of the Czech Republic, for his hospitality and assistance while attending the IAEA/ICTP Joint Experiment on CASTOR tokamak in Prague, CR.

Technical assistance provided by Dave McColl, Perry Balon, Blair Chomyshen and Ted Toporowski was appreciated. I would also like to graciously acknowledge assistance from fellow graduate students Dazhi Liu and JT Steenkamp on several matters.

This work was supported by funds from the Natural Sciences and Engineering Research Council of Canada and through financial aid from the University of Saskatchewan. The work on CASTOR tokamak was supported by funds from the International Atomic Energy Agency and the International Centre for Theoretical Physics.

Contents

List of Tables

List of Figures

List of Abbreviations and Terms

STOR-M	Saskatchewan Torus-Modified
STOR-1M	Saskatchewan Torus-1 Modified
CASTOR	Czech Academy of Sciences Torus
SOL	Scrape-Off Layer
H-Mode	Improved confinement discharge
L-Mode	Normal discharge
RF	Radio Frequency
OH	Ohmic Heating
TH	Turbulent Heating
CT	Compact Torus
MHD	Magnetohydrodynamics
MPSE	Magnetic Pre-Sheath Entrance
TZM	Titanium Zirconium Molybdenum alloy
CAMAC	Computer Automated Measurement And Control
τ_E	Energy confinement time
Q	Fusion power gain
q_s	Safety factor
a, R_o	Minor and major radii
r, R	Minor and major radial coordinates
B_ϕ	Toroidal magnetic field
B_θ	Poloidal magnetic field
I_p	Plasma current
V_l	Loop voltage
ε_0	Permittivity of free space
μ_0	Permeability of free space
ω	Frequency
ε	Aspect ratio ($\varepsilon = a/R_0$)
$n_{i,e}$	Plasma density of ions and electrons

n_∞	Unperturbed ion density of the plasma (far from any electrostatic probe)
$m_{i,e}$	Ion and Electron mass
e	Elementary charge
$T_{i,e}$	Ion and electron temperature (in eV unless otherwise specified)
H	Confinement improvement factor
$p_{i,e}$	Ion and electron pressure
V_p	Plasma potential
V_f	Floating potential
E_r	Radial electric field
v_ϕ	Toroidal plasma velocity
v_θ	Poloidal plasma velocity
$v_{\|\|}$	Plasma velocity parallel to the total magnetic field
$v_\perp$	Plasma velocity perpendicular to the total magnetic field
c_s	Ion sound speed
$M_{\|\|}$	Mach number of the plasma flow parallel to the total magnetic field
$M_\perp$	Mach number of the plasma flow parallel to the total magnetic field
$J_{i0,e0}$	Ion and Electron saturation current density
Z	Atomic number
Z_{eff}	Effective (average) atomic number of plasma ions

Chapter 1

Introduction

1.1 Fusion

Controlled thermonuclear fusion promises to provide a clean power source with sufficient fuel reserves to last far into the future [1]. In nuclear fusion two light nuclei fuse together to form a heavier nucleus and releases energy. For two nuclei to fuse, they must collide with enough energy to overcome the repulsive electrostatic force between them. In stars, hydrogen nuclei are fused thanks to high densities and long confinement times created by the intense pressure in the stellar core. In the laboratory, it is practically impossible to recreate the conditions necessary to fuse hydrogen.

The most promising method of harnessing nuclear fusion is to heat a fuel mixture of deuterium and tritium to a sufficiently high temperature that the thermal velocities of the nuclei are high enough to overcome the Coulomb repulsion between them. For deuterium-tritium fusion, the reaction cross-section reaches a maximum at 100 keV, and has the largest cross-section of the possible fusion reactions at this energy (see Figure 1.1). The reaction between deuterium and tritium is [2]:

$$ {}^{2}_{1}\mathrm{D} + {}^{3}_{1}\mathrm{T} \rightarrow {}^{4}_{2}\alpha\ (3.5\ \mathrm{MeV}) + {}^{1}_{0}\mathrm{n}\ (14.1\ \mathrm{MeV}), \qquad (1\text{-}1) $$

which releases 17.6 MeV per reaction. Though the cross-section has a maximum at 100 keV, it is sufficient to heat the plasma to about 20 keV because the required reactions occur in the high-energy tail of the Maxwellian distribution. Additionally, due to the scaling of confinement time (see section 1.2), the Lawson criterion, presented below, is best met at plasma temperatures of around 10 to 20 keV. At temperatures of 20 keV, the

fuel becomes a fully ionized plasma, where the electrostatic charge of the ions is balanced by that of electrons.

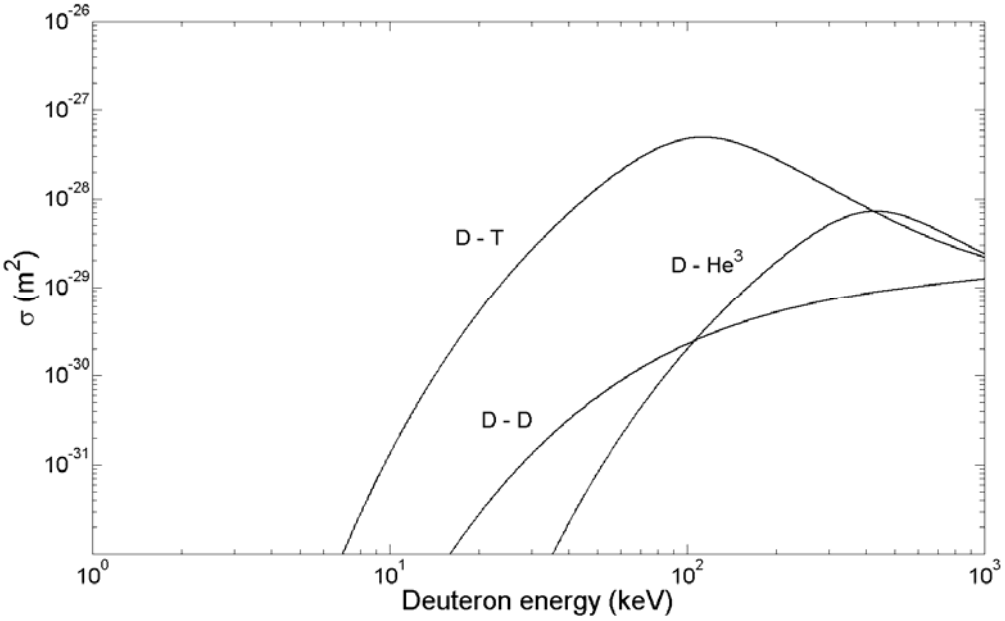

Figure 1.1: Nuclear fusion cross-section as a function of deuteron energy for several possible fusion reactions. It is clear that the largest cross-section is for the D – T reaction at about 100 keV.

Deuterium is readily available; it exists in a weight ratio of 1:5000 with hydrogen. Tritium does not occur naturally, as it undergoes β-decay with a half-life of 12.3 years. Therefore, the tritium necessary for fusion must be bred by bombarding lithium with neutrons as follows [3]:

$$ {}^{6}_{3}\mathrm{Li} + {}^{0}_{1}\mathrm{n} \rightarrow {}^{4}_{2}\mathrm{He} + {}^{3}_{1}\mathrm{T} + 4.8\ \mathrm{MeV}\,, \tag{1-2} $$

$$ {}^{7}_{3}\mathrm{Li} + {}^{0}_{1}\mathrm{n} \rightarrow {}^{4}_{2}\mathrm{He} + {}^{3}_{1}\mathrm{T} + {}^{0}_{1}\mathrm{n} - 2.47\ \mathrm{MeV}\,, \tag{1-3} $$

The ratio of ^{7}Li to ^{6}Li must be regulated in order to ensure that the amount of tritium bred exceeds that consumed in the reactor.

The Lawson criterion [4] places a lower boundary on the product of density and confinement time that a thermonuclear reactor would require in order to produce enough fusion power to be practical as a power station. The Lawson criterion can be expressed as

$$n\tau_E > 0.6\times10^{20}\,\mathrm{m^{-3}s}, \tag{1-4}$$

where n is the fuel density and τ_E is the energy confinement time. When a D-T plasma is heated to thermonuclear conditions, an increasing fraction of the total heating is provided by α-particles. If the energy confinement time is suitably high, it is possible to maintain the plasma temperature solely with α-particle heating and external heating can be removed. By analogy with combustion, this condition is referred to as ignition. The criterion for ignition is the fusion triple product [2]:

$$\hat{n}\hat{T}\tau_E > 5\times10^{21}\,\mathrm{m^{-3}\,keV\cdot s}, \tag{1-5}$$

where $\hat{n}$ and $\hat{T}$ are the peak values of the fuel density and temperature, and the temperature is understood to be in units of keV.

A measure of the success in approaching reactor conditions is

$$Q = \frac{P_F}{P_H} = \frac{5P_\alpha}{P_H}, \tag{1-6}$$

where P_F is the fusion power released, P_H is the external heating power and P_α is the power released in the α-particles. The term $5P_\alpha$ arises since the energy released from each D-T reaction is five times the α-particle energy. Q = 1 is called break-even. At ignition, P_H is reduced to zero and Q becomes infinite. Although an infinite Q is ideal, a power station could be constructed using a fusion reactor with a large Q, but without ignition.

The progress in developing a working fusion reactor has been slow but steady. The trend has been to build larger and larger machines using knowledge gained from the previous generation of machines. The current generation of large tokamaks has made significant progress towards the goal of harnessing fusion power. In 1997, the Joint European Torus (JET) achieved a Q of 0.6 [5] with a fusion power of 13 MW and in 1998 the Japan Tokamak-60 Upgrade (JT-60U) achieved an equivalent Q of 1.25 and a fusion triple product of 1.53×10^{21} m^{-3} keV·s with an ion temperature of 45 keV [6]. The equivalent Q value from JT-60U is based on the measurement of the Q value from D-D fusion and is then related to the equivalent Q value for D-T fusion [7].

1.2 Tokamak

The word tokamak is an acronym derived from the Russian phrase describing it: "***tor***oidalnaya ***ka***mera ee ***ma***gnitnaya ***k***atushka" which means "toroidal chamber and magnetic coil". This idea was proposed by Andrei Sakharov and Igor Tamm in the 1950's [8]. The first tokamak, TMB, was built in Russia in 1955. Since it was believed that the neutrons produced by a fusion reactor could be used to breed weapons grade plutonium, the idea was kept top secret. Early tokamak experiments showed that it was so difficult to achieve plasma discharges lasting even a few milliseconds that the Soviet Union declassified its research at the 2nd UN International Conference on Peaceful Uses of Atomic Energy in Geneva, Switzerland, 1958 [9].

A tokamak is a torus-shaped device that uses magnetic fields to confine a plasma. The main component of the magnetic field is provided by a set of magnetic coils that encircle the torus-shaped vacuum chamber and produce the toroidal magnetic field, B_ϕ. The typical geometry of a tokamak is shown in Figure 1.2.

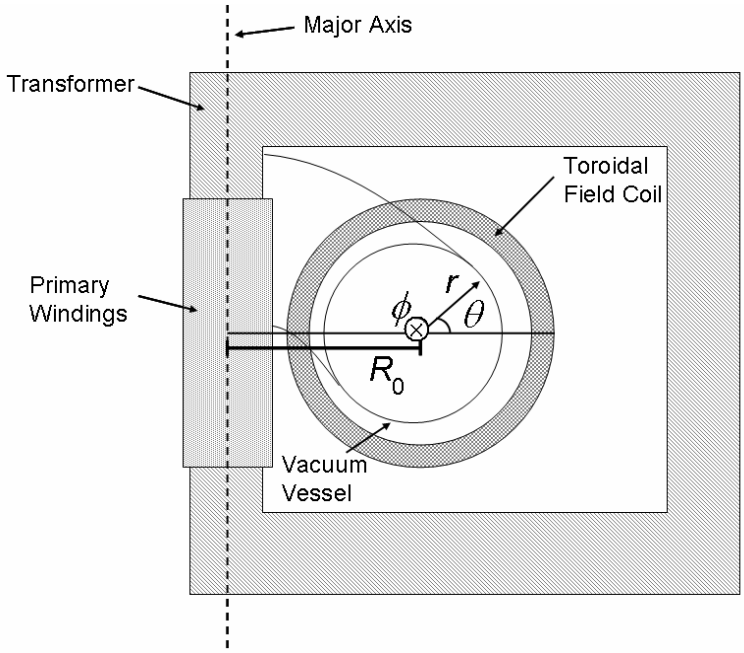

Figure 1.2: Cross-section of a tokamak showing the toroidal coordinates (r,θ,ϕ), the major radius (R_0) as well as the major components: the transformer, the primary windings, the vacuum vessel, the toroidal field coil. The major axis of the machine is shown for reference.

There is, however, no stable equilibrium to a purely toroidal magnetic field. This is because such a field causes two particle drifts, the curvature and gradient drifts which are given by [10] as:

$$\vec{v}_R + \vec{v}_{\nabla B} = \frac{m}{q}\frac{\vec{R}_c \times \vec{B}}{R_c^2 B^2}\left(v_{\parallel}^2 + \frac{1}{2}v_{\perp}^2\right), \tag{1-7}$$

where $\vec{v}_R$ is the curvature drift velocity, $\vec{v}_{\nabla B}$ is the gradient drift velocity, m is the particle's mass, q the particle's charge, $\vec{R}_c$ is the radius of curvature of the magnetic field, $\vec{B}$ is the magnetic field, $v_{\perp}$ is the velocity component of the particle in the plane perpendicular to the magnetic field and $v_{\parallel}$ is the velocity component of the particle in the direction parallel to the magnetic field. The magnetic drifts are in opposite directions for ions and electrons and in a toroidal magnetic field this causes a vertical charge separation. This vertical charge separation creates a vertical electric field $\vec{E}$. An electric field perpendicular to the magnetic field causes another particle drift known as the $\vec{E}\times\vec{B}$ drift which is given by [10] as:

$$\vec{v}_{E\times B} = \frac{\vec{E}\times\vec{B}}{B^2}, \tag{1-8}$$

where $\vec{v}_{E\times B}$ is the $\vec{E}\times\vec{B}$ drift velocity. This drift causes particles to drift towards the outer wall, and the plasma is not confined. This can be seen schematically in Figure 1.3.

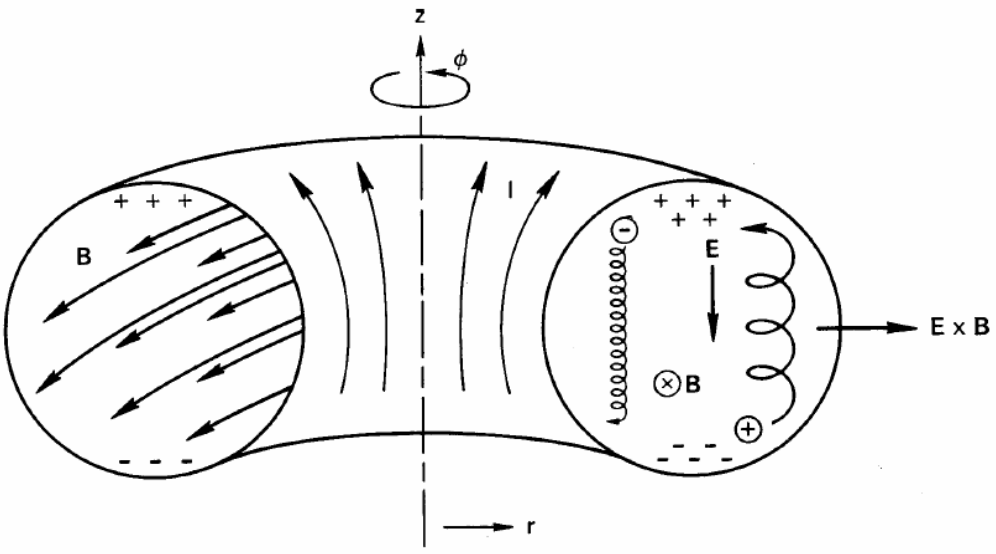

Figure 1.3: Particle motion in a toroidal field. Due to charge separation caused by the magnetic curvature and gradient drifts, the particles are pushed outward due to the $\vec{E} \times \vec{B}$ drift Chen [11].

It is possible to have a stable equilibrium by superimposing a poloidal magnetic field B_θ onto the toroidal magnetic field. In tokamaks, this is primarily done by driving a toroidal current through the plasma (see Figure 1.4) using transformer action or several non-inductive current drive methods. The helical magnetic field lines define a set of nested toroidal magnetic surfaces in the plasma. The helicity of the magnetic field is described by the rotational transform angle ι (iota) which is the poloidal angle traversed by the magnetic field line after one rotation in the toroidal direction. The rotational transform angle is given by [1] as:

$$\iota = \frac{2\pi R_0}{r}\frac{B_\theta}{B_\phi} = \frac{2\pi}{q_s} \tag{1-9}$$

where R_0 is the major radius of the plasma, r is the minor radius, and q_s is the safety factor. The safety factor q, which is the number of toroidal rotations a field line makes before returning to its starting position in the poloidal plane, is [2]:

$$q_s(r) = \frac{rB_\phi}{R_0 B_\theta}. \tag{1-10}$$

The safety factor plays a critical role in stability and generally higher values of q_s lead to greater stability. Consequently q_s appears as an important factor in transport theory. The resultant helical magnetic field can neutralize the charge separation in the following way. Assume that a particle near the top of the torus has a drift velocity that is vertically upward and thus away from the axis of the torus due to the gradient and curvature drifts. Due to its velocity along the helical field line, the particle will eventually be at the bottom of the torus. At the bottom of the torus, the drift velocity is still vertically upward but is now toward the axis of the torus. The particle drifts away from the axis part of the time and toward the axis part of the time. Thus for a sufficiently large rotational transform angle the outward and inward drifts cancel and the particle can be confined by the helical magnetic field. In addition to the toroidal magnetic field and the poloidal field due to the plasma current, additional horizontal and vertical magnetic fields are required for plasma positioning (see sections 2.3.4 and 2.3.5). The toroidal, poloidal and resultant helical magnetic fields, the plasma current and the nested toroidal magnetic surfaces are shown in Figure 1.4.

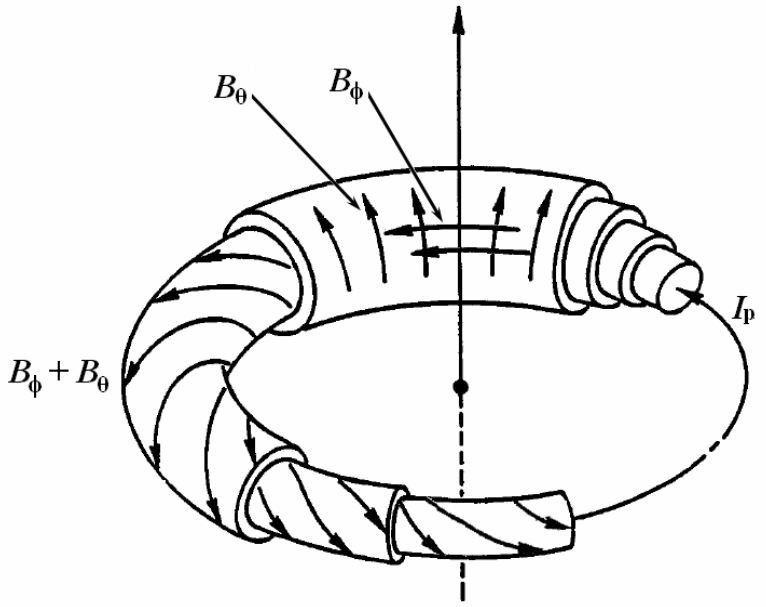

Figure 1.4: Schematic of the plasma in a tokamak showing the toroidal magnetic field (B_θ), the poloidal magnetic field, the resultant helical magnetic field ($B_\phi + B_\theta$), the plasma current I_p and the nested toroidal magnetic surfaces, Chen [11].

The current used to create the poloidal magnetic field is also used to Ohmically heat the plasma. Due to the strong dependence of the plasma resistivity on the electron temperature ($\eta \propto T_e^{-3/2}$), Ohmic heating is ineffective beyond an electron temperature of about 1 keV (at which the plasma resistivity becomes comparable with that of copper) and alternative heating techniques such as neutral beam injection [12] or radio-frequency wave heating [13] are required.

Despite the seemingly simplistic operation of a tokamak to confine a thermonuclear plasma, experiments show that in reality it is exceedingly difficult. The experimentally observed confinement time is orders of magnitude shorter than what is predicted by neoclassical theory [2]. Many explanations of the lower than expected energy confinement time focus on increased cross-field transport caused by turbulence and micro-instabilities in the plasma [14]. This anomalous transport is one of the major obstacles in achieving the plasma performance necessary for a power producing fusion reactor.

Additionally, the observed scaling of energy confinement time from the ITER-like dataset is [15]:

$$\tau_E^{ITER} \sim 0.0232 I^{0.90} B_\phi^{0.19} R_0^{1.31} n^{0.38} a^{-1.07} A^{0.85} M^{0.13} P^{-0.69}, \tag{1-11}$$

where I is the plasma current (MA), B_ϕ is the toroidal magnetic field (T), R_0 is the major radius (m), n is the line averaged density (10^{19} m^{-3}), a is the minor radius (m), A is the cross-sectional area (m^2), M is the isotope mass of the fuel (atomic mass units) and P is the input power (MW). This scaling has been empirically deduced from observations on nine of the most advanced tokamaks (the Axisymmetric Divertor Experiment (ASDEX) Upgrade, Alcator C-Mod, Compass-D, Doublet III-D , JET, JT-60U, the Megaampere Spherical Tokamak (MAST), the National Spherical Torus Experiment (NSTX) and Tokamak à Configuration Variable (TCV)) [16]. This is radically different from the scaling predicted by neoclassical theory:

$$\tau_E^{nc} \sim \frac{T^{1/2} B_\theta^2 \ell^2}{n}, \tag{1-12}$$

where ℓ is the plasma size [2]. Equations 1-11 and 1-12 predict very different scaling for the energy confinement time. Equation 1-11 indicates that τ_E increases for increasing density n, while 1-12 predicts that τ_E decreases for increasing n. Additionally, 1-11 indicates that for increasing input power P τ_E decreases while 1-12 predicts that τ_E should increase for increasing temperature T, where T and P should be positively related.

An operating regime known as high confinement mode (H-mode) has been discovered in tokamaks [17] which can significantly improve confinement. Advanced tokamaks have been able to suppress the transport of ions to the level predicted by neoclassical theory [18]. The next generation tokamak ITER will operate in H-mode where it is designed to produce fusion plasmas with $Q \geq 10$ [19].

A clear understanding of the mechanism of H-mode is critical to tokamaks. It has been suggested that a sheared poloidal flow causes decorrelation of turbulence in the plasma and causes the observed improvements in confinement [20]. Sheared poloidal flows have been observed in many tokamaks during H-mode [21, 22, 23, 24], though the mechanism for these flows has not yet been resolved.

In order to study sheared poloidal flows on the STOR-M tokamak during both Ohmic mode and H-mode, an advanced Langmuir probe array known as a Gundestrup probe [25] is used. This probe allows for the simultaneous measurement of both the toroidal and poloidal flow velocities and measurements of the floating potential and electron density and temperature as well as floating potential and electron density fluctuations.

1.3 Thesis Goals and Objectives

The goals and objectives of this thesis are summarized below:

1) Install the Gundestrup probe on STOR-M tokamak modifying and repairing the probe as necessary. Build and test the electronics necessary for the probe.
2) Perform plasma flow velocity measurements during the normal Ohmic discharge on STOR-M. Reverse the orientation of the toroidal magnetic field B_ϕ and plasma current I_p to determine the effect on the flow velocity.
3) Use the turbulent heating and electrode biasing systems on STOR-M to study the effects of these systems on the plasma flow velocity.

4) Consider future experiments on STOR-M tokamak using the Gundestrup probe.

1.4 Thesis Outline

The thesis is organized into 7 chapters. The first chapter has described the basics of nuclear fusion, the tokamak and has outlined the goals and objectives of this thesis.

Chapter 2 describes the major components of the STOR-M tokamak. This includes the vacuum and gas feed systems and the various magnetic windings.

Chapter 3 describes the major diagnostics used on STOR-M. These include Rogowski coils, the position sensing coils, the 4 mm microwave interferometer, the spectrometer and Mirnov coils.

Chapter 4 presents the theory of the present experiments. H-mode is explained and discussed in section 4.2. Section 4.3 describes the role of plasma drifts and the radial electric field in H-mode and the effect of plasma flow on turbulence. Mechanisms of flow generation in the edge region of a tokamak are discussed in section 4.4. These include ion orbit loss, anomalous Stringer drive and Reynolds stress. The theoretical model used for the analysis of the Gundestrup probe data used in this analysis is presented in section 4.5.

Chapter 5 describes the new probes used for these experiments. Section 5.2 describes the Gundestrup probe used for flow measurements in detail. The rake probe which is used for floating potential and density measurements is described in section 5.3.

Chapter 6 presents the relevant results of this investigation. Section 6.2 discusses the results obtained during the normal Ohmic discharge. Section 6.3 discusses the results obtained with the reversal of the toroidal magnetic field. The results from the turbulent heating experiments are examined in section 6.4. Section 6.5 presents the results from the electrode biasing results. The results of experiments done on the Czech Academy of Sciences Torus (CASTOR) tokamak during the IAEA/ICTP Joint Experiment in Prague, CR are presented in section 6.6 for comparative purposes.

Chapter 7 summarizes the work done in this thesis and presents suggestions for future work including flow measurements during Compact Torus Injection and the use of a new biasing electrode.

Chapter 2

STOR-M

2.1 Introduction

The Saskatchewan Torus-Modified (STOR-M) tokamak is the upgraded version of STOR-1M tokamak (major radius R_0 = 22 cm, minor radius a = 3.5 cm) which was also built for turbulent heating (TH) studies. STOR-M has a major radius of 46 cm and a plasma (limiter) radius of 12 cm. The machine was completed in 1987 and has been involved in numerous studies: turbulent heating [26], AC operation [27], electrode biasing [28] and Compact torus (CT) injection [29], to name a few. The larger size of STOR-M was meant to show a more clear-cut preferential edge heating associated with the skin effect of TH and to be less susceptible to plasma impurity problems than STOR-1M [30].

2.2 Vacuum and Gas Feed Systems

The vacuum chamber consists of two 0.1566" (4 mm) thick type 304L stainless steel elbows of circular cross-section with a minor diameter of 12.75" (324 mm). Each half of the chamber is connected at one end to a stainless steel bellows to reduce mechanical stress on the chamber. The two halves of the chamber are separated by two 20 mm thick alumina (Al_2O_3) ceramic breaks. The breaks prevent current induction into the vacuum chamber by the Ohmic coils. This creates a discharge chamber with a major radius R_0 of 46 cm and minor radius a_0 of 15.8 cm.

The chamber is equipped with 10 horizontal, 11 vertical and 2 tangential ports that are used for pumping, gas feed and diagnostics. The stainless steel limiter is a combination of circular and horizontal rail limiters. It determines the 12 cm minor radius

of the plasma and allows for up to 1 cm of horizontal displacement without additional scrape off.

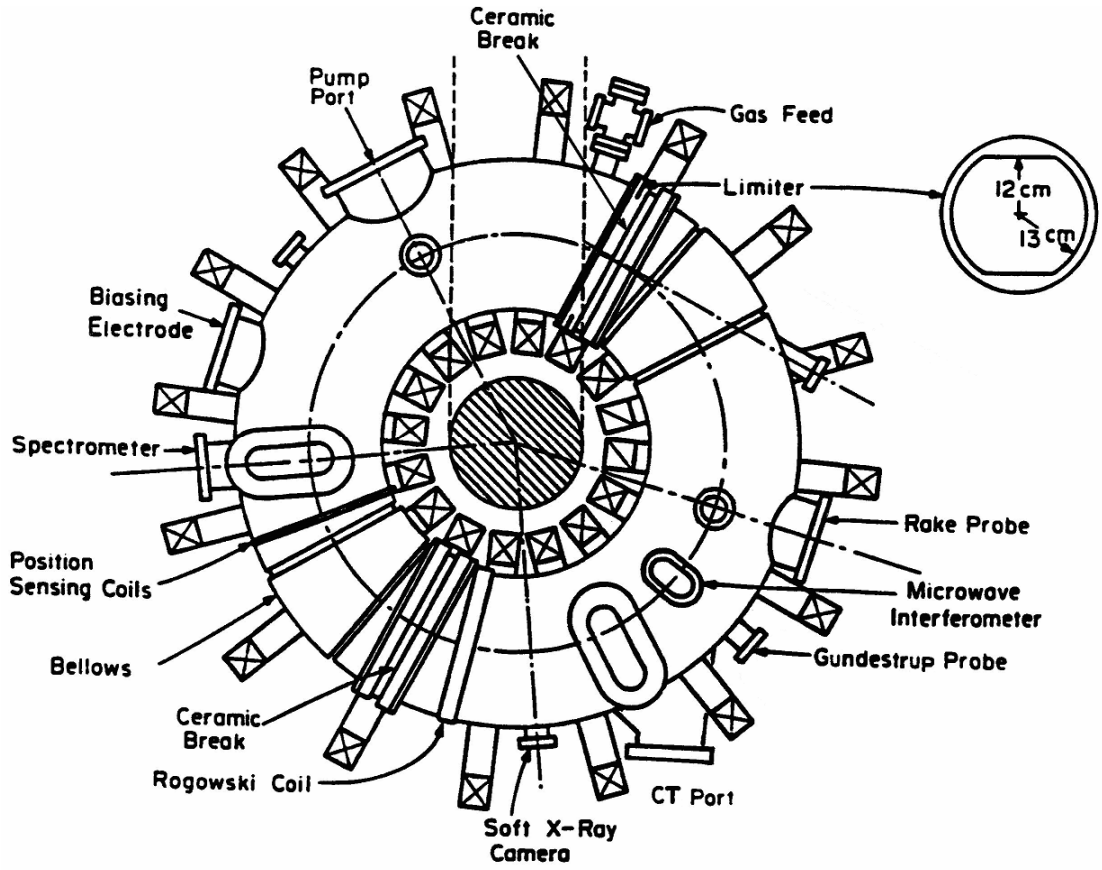

Figure 2.1: The STOR-M tokamak chamber and limiter. Diagnostic locations are shown.

The vacuum chamber is evacuated by a turbomolecular pump with a pumping speed of 1000 L/s backed by a rotary vane pump. The chamber is typically pumped to a base pressure of 1×10^{-7} Torr and then filled to 1.8×10^{-4} Torr with ultra high purity (99.999%) hydrogen. The pressure is held constant using a Veeco Automatic Pressure Controller and the chamber is filled through a Veeco PV-10 piezoelectric valve. Two ionization gauges, one on the chamber and one on the pump inlet, monitor the gas pressure. Two additional PV-10 valves, separated toroidally by 180°, are used with a preprogrammed open loop controller for the purpose of gas puffing during the discharge to control the plasma density.

2.3 Toroidal and Poloidal Field Systems

Magnetic fields are used both to confine and position the plasma inside of the vacuum chamber. These magnetic fields are produced both by external windings (Figure 2.2) and by the plasma current.

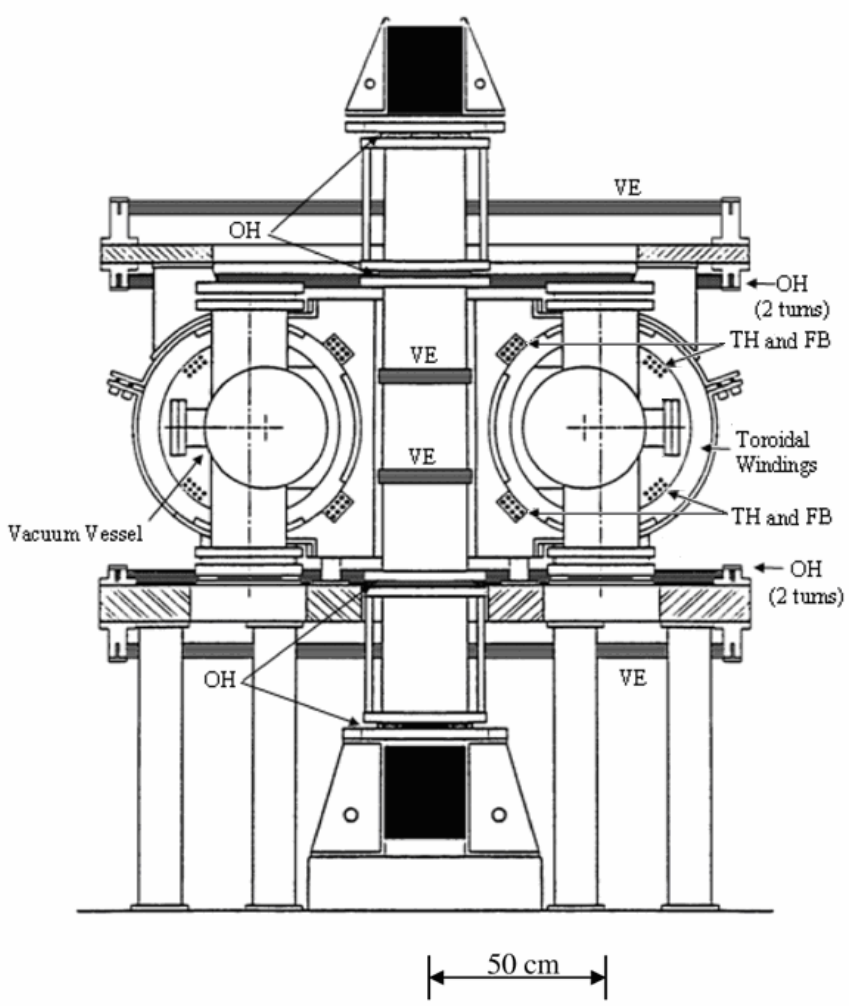

Figure 2.2: A vertical cross-section of STOR-M showing the locations of the Vertical Equilibrium (VE) windings, the Ohmic Heating (OH) windings, the Turbulent Heating (TH) and Feedback (FB) winding and the Toroidal windings.

2.3.1 Toroidal Field Coils

The vacuum chamber is surrounded by the toroidal field winding. This winding consists of 16 spools spaced evenly in the toroidal direction, each having 9 turns of ¼" × 2 ¾" copper for a total of N = 144 turns. The coils are connected in series with a total inductance of 2.06 mH and a resistance of 13.5 mΩ (at room temperature) [30]. The toroidal field at the center of the chamber is

$$B_\phi = \frac{\mu_0 N I_{B_\phi}}{2\pi R} = 0.0626 I_{B_\phi}, (\mathrm{T}), \tag{2-1}$$

where I_{B_ϕ} is the current in the toroidal magnet in kA. The maximum current is about 12 kA which corresponds to $B_\phi \approx 0.7$ T. The toroidal field current has a rise time of 6.5 ms and a decay time of 400 ms.

2.3.2 Pre-ionization

A radio frequency (RF) field is induced by two parallel windings near the vacuum chamber. This is done to create a weakly ionized 'seed' plasma in the chamber prior to the main Ohmic discharge. This pre-ionization improves shot-to-shot reproducibility and saves magnetic flux (V·s) in the iron core transformer.

2.3.3 Ohmic Heating (OH) System

The vacuum chamber encloses one leg of the iron core transformer. The weakly ionized plasma serves as a secondary winding on the transformer. The Ohmic heating windings (transformer primary windings) enclose the same leg of the transformer and consist of 8 turns of ¼ " × 1 ½" copper busbar. These windings are shown in Figure 2.2 (labeled OH). Three capacitor banks are used to produce a preprogrammed primary waveform, the bias bank, the fast bank and the slow bank. The bias bank (450 V, 20 mF) is used to negatively bias the transformer. This is done to maximize the flux available for driving plasma current. The fast bank (450 V, 200 mF) is used for the current ramp-up phase of the discharge and the slow bank (100 V, 10 F) is used to maintain the plasma current. The OH circuit is shown in Figure 2.3.

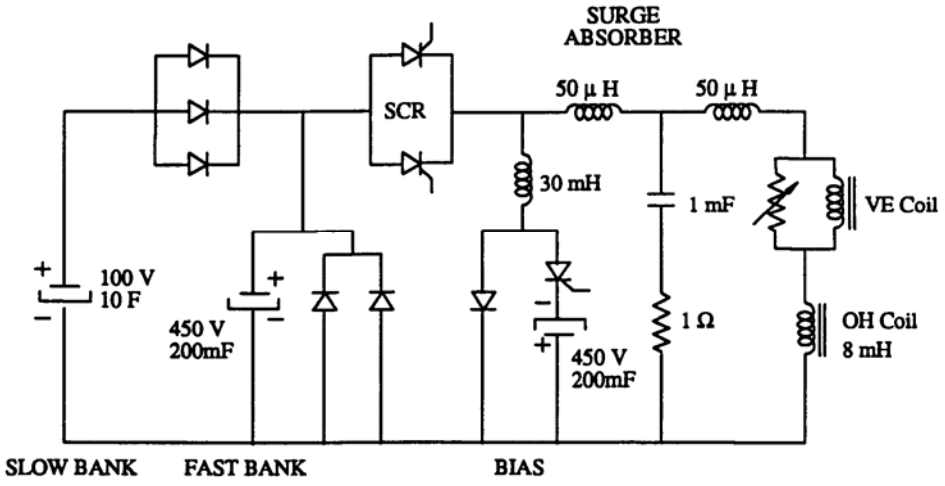

Figure 2.3: Schematic of the Ohmic heating circuit on STOR-M.

The surge absorber and diodes shown in Figure 2.3 are necessary to protect vital components of the OH circuit. The three diodes connected in parallel which are in series with the slow capacitor bank ensure that the slow bank will only fire when the voltages on the slow bank and fast bank are the same. Typically the fast bank is charged to 150 V while the slow bank is charged to 60 V. The surge absorber inductors and capacitor are used to prevent large induced voltages on the OH coil and VE coil from damaging the OH power supply during turbulent heating experiments or in the case of a disruption.

2.3.4 Vertical Magnetic Field

The horizontal position of the plasma is controlled by the vertical magnetic field, which has two components. The first is a preprogrammed field produced by the 4 turns of ¼ " × 1 ½" copper busbar (labeled VE in Figure 2.2). These winding are in series with the OH windings and are powered by the OH capacitor bank. These windings share the same power supply as in the lowest order the required vertical field is proportional to the plasma current. The second is a smaller "correction" field for more precise plasma position control. These windings (labeled FB in Figure 2.2) are constructed from 2 AWG stranded copper cable and are powered by an active feedback system [30].

Approximately half of the vertical magnetic field is provided by the plasma current itself through the image current in the iron transformer core [31].

2.3.5 Horizontal Magnetic Field

The vertical position of the plasma is controlled by the horizontal magnetic field. This field was only required after the upgrade to STOR-M in 1994-1995 when the toroidal field coils were replaced. The new coils have a larger stray than the original coils due to slight errors in alignment, making a horizontal compensation field necessary for ionization and smooth current build up [32]. A preprogrammed circuit controls the horizontal magnetic field.

2.3.6 Turbulent Heating System

Turbulent heating is the application of a short, intense spike in the plasma current. In STOR-M, this is done by applying a current to 4 windings (labeled TH in Figure 2.2) that induce a large electric field in the plasma. These 4 winding are connected in parallel to a 5 kV, 1 mF capacitor bank through an ignitron switch. The current pulse has a rise time of 40 μs and a pulse length of 100 μs. The peak plasma current can be as high as 50 kA with the use of the turbulent heating system.

2.4 Electrode Biasing Circuit

Plasma biasing is done with a stainless steel electrode inserted beyond the limiter at the outboard midplane of STOR-M. The electrode is cylindrical with a length of 23 mm and a diameter of 20 mm. The electrode is mounted to a stainless steel shaft that is insulated with an alumina tube. The radial position of the electrode can be moved inward to a minimum minor radius of 67 mm and can be moved outside of the limiter where it remains when not in use. The electrode is connected to a 900 V, 11.25 mF capacitor bank that is charged with a 2000 V, 1.5 A power supply. This system can be used for either positive or negative biasing of the electrode. The electrode is switched on by applying a trigger pulse to a silicon controlled rectifier (SCR).

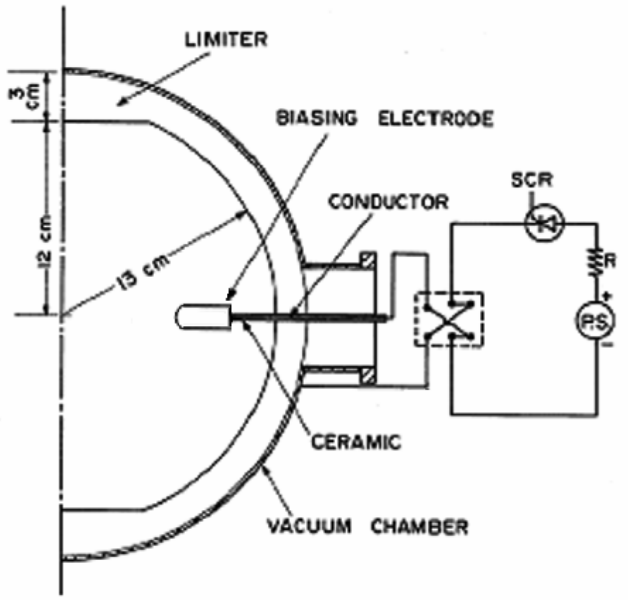

Figure 2.4: Schematic of the electrode biasing circuit.

Chapter 3

Diagnostic Equipment

3.1 Introduction

The STOR-M tokamak is equipped with a standard set of diagnostic equipment for monitoring plasma and machine parameters during operation. Most of the diagnostics are passive and non-invasive as it is desirable to monitor the plasma parameters without disturbing the plasma. Langmuir probes are invasive, but are kept near the plasma edge ($r/a \approx 1$) so that they are not destroyed by the hot central plasma, which will erode the probe, introducing significant impurities into the system. These impurities can significantly degrade the quality of the plasma discharges and can result in plasma disruptions.

The diagnostic equipment on STOR-M include a 4-mm microwave interferometer [33], a hard X-ray detector [30], a double-array soft X-ray detector camera [30], an optical spectrometer [34], Mirnov Coils [34], Rogowski coils [35] and various Langmuir and magnetic probes. The hard X-ray detector and the soft X-ray camera are not routinely used and are not discussed further.

3.2 Rogowski Coils

Rogowski coils are used to measure currents in the plasma and the various windings on STOR-M. A Rogowski coil is an N-turn coil wound on a non-magnetic former. The windings completely encircle a conductor carrying a time-varying current. If the current is varying with time, the Rogowski coil produces a voltage, V_{RC}, that is proportional to the number of turns, N, on the coil and the time rate of change of the magnetic flux ϕ, linking it

$$V_{RC} = -N\frac{d\phi}{dt}. \tag{3-1}$$

The magnetic flux as a function of time can be obtained by integrating V_{RC}. For a Rogowski coil having a major radius, R_R, width, a_R, and thickness, b_R, the current can be determined using Ampere's law:

$$I = \oint_c \vec{H}\cdot d\vec{l} = \frac{\frac{\phi}{a_R b_R}2\pi R_R}{\mu_0} = -\frac{2\pi R_R}{\mu_0 N a_R b_R}\int V_{RC}dt, \tag{3-2}$$

where μ_0 is the permeability of free space. An example of a Rogowski coil is shown in Figure 3.1. A Rogowski coil monitors a current enclosed by the coil regardless of the current position.

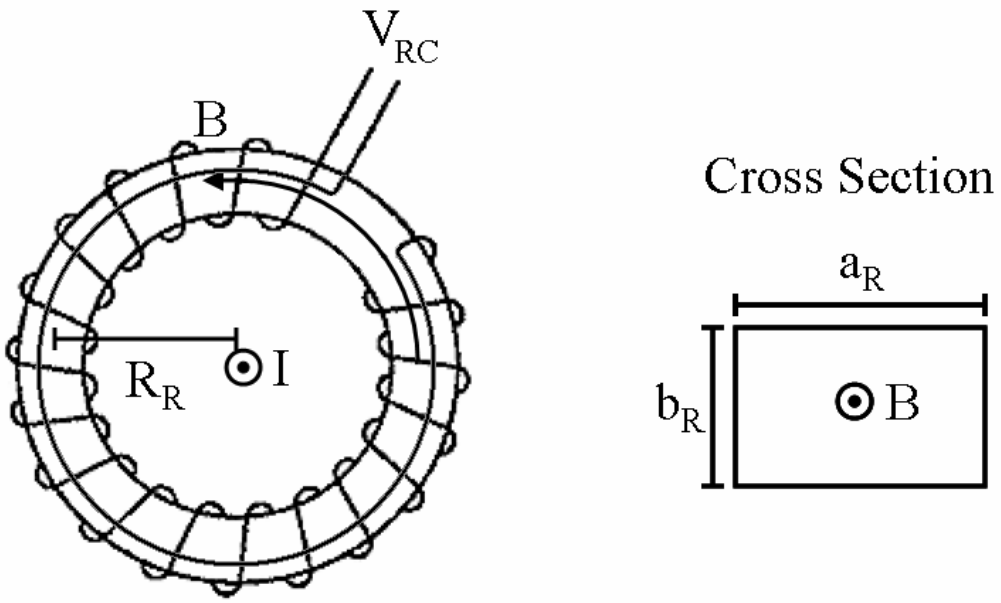

Figure 3.1: A typical Rogowski coil used for current measurements.

On STOR-M, the Rogowski coils are constructed with 26 AWG enameled wire except for the plasma current Rogowski coil, which is constructed, with 18 AWG wire. They are wound on toroidal formers with rectangular cross-sections. To reduce the pickup of magnetic flux from external sources, a return winding is also wound on the

former in the opposite toroidal direction. The output signal of each Rogowski coil is brought to the control room on 20 m of RG 58/U where it is integrated with a gated, active integrator and then connected to the data acquisition system. The frequency response of each coil is linear up to 800 kHz, which is sufficient for the parameters of STOR-M they monitor. The coils have been absolutely calibrated with a commercial Rogowski coil from Pearson Electronics [30].

3.3 Plasma Loop Voltage

Measuring the plasma loop voltage is the simplest of all diagnostics on STOR-M. It is done by measuring the voltage around a toroidal loop of wire that is parallel to the plasma. The voltage picked up by this loop is has both resistive and inductive components. The voltage V_l, picked up by the loop is given by

$$V_l = R_p I_p + \frac{d}{dt}\left(L_p I_p\right), \tag{3-3}$$

where I_p is the plasma current, R_p is the plasma resistance and L_p is the plasma inductance. The plasma resistance is given by

$$R_p = \eta \frac{2R_0}{a^2}, \tag{3-4}$$

where R_0 is the plasma major radius, a the minor radius and η is the average plasma resistivity. The plasma inductance is given by [30]

$$L_p = \mu_0 R_0 \left[\ln\left(\frac{8R_0}{a}\right) + \frac{l_i}{2} - 2 \right], \tag{3-5}$$

where l_i is the plasma internal inductance parameter defined by [2]

$$l_i = \frac{\overline{B_\theta^2}}{B_\theta^2(a)} = \frac{2\int_0^a B_\theta^2(r) r dr}{a^2 B_\theta^2(a)}. \tag{3-6}$$

Here, $B_\theta(r)$ is the poloidal magnetic field at a distance r from the axis of the plasma column and $B_\theta(a)$ is the poloidal magnetic field at the edge of the plasma column. The internal inductance parameter depends on the toroidal current density profile and ranges

from zero for a skin current to 0.5 for a uniform current density profile to greater than 1 for a centrally peaked current density profile [36].

The plasma current and loop voltage can be used to estimate the plasma resistivity. In the quasisteady state of the discharge, the plasma resistance is $R_p \approx V_l/I_p$. From this, the average temperature can be calculated using the neoclassical resistivity [2]. The neoclassical resistivity, η_{nc}, which takes into account trapped electrons, can be approximated with the expression

$$\eta_{nc} = \frac{\eta_S}{1 - 1.95\sqrt{\varepsilon} + 0.95\varepsilon}, \tag{3-7}$$

where η_S is the Spitzer resistivity,

$$\eta_S = 1.65 \times 10^{-9} \frac{Z_{eff} \ln \Lambda}{T_e^{3/2}} \ \text{ohm} \cdot \text{m}, \tag{3-8}$$

ε is the inverse aspect ratio of the machine ($\varepsilon = a/R_0$), Z_{eff} is the effective ion charge number, T_e is the electron temperature in keV and $\ln\Lambda$ is the Coulomb logarithm, which is a term that accounts for the multiple small angle collisions in the plasma and Debye shielding. Λ (essentially the number of electrons in a Debye sphere) is given by

$$\Lambda = 12\pi n_e \left(\frac{\varepsilon_0 T_e}{n_e e^2} \right)^{3/2}. \tag{3-9}$$

For the typical conditions in STOR-M ($n_e \approx 5\times10^{18}$ m^{-3}, $T_e \approx 220$ eV), $\ln\Lambda$ is approximately 17. The terms involving the inverse aspect ratio ε accounts for trapped electrons, which do not carry a current and thus effectively increase the plasma resistivity.

The electron temperature can be estimated from the measured resistivity as

$$T_e \approx \left(\frac{2.6\times10^{-4}}{\left(1 - 1.95\sqrt{\varepsilon} + 0.95\varepsilon\right)} \frac{2Z_{eff} I_p R_0 \ln\Lambda}{V_l a^2} \right)^{2/3} \approx \left(\frac{0.01326}{\left(1 - 1.95\sqrt{\varepsilon} + 0.95\varepsilon\right)} \frac{I_p R_0}{V_l a^2} \right)^{2/3}, \tag{3-10}$$

where R_0 and a are the major and minor radii. For a typical discharge in STOR-M plasma parameters ($I_p \approx 20$ kA, $Z_{eff} \approx 1.5$ and $V_l \approx 4$ V) the average electron temperature is about 220 eV.

3.4 Position Sensing Coils

Accurate measurements of the plasma position are very important since relatively small displacements of the plasma column position within the vacuum chamber can cause disruptions. The quality of the discharge is dictated by the quality of the position of the plasma column. Six magnetic probes are mounted around the outside of the vacuum chamber at a minor radius of 170 mm to monitor the plasma position. Four of these coils are used to detect the poloidal magnetic field, B_θ. These four coils are located at the same toroidal position, but are separated poloidally by 90°. Two other probes detect the radial component of the magnetic field at poloidal angles of ±90°. The orientation of these coils is shown in Figure 3.2. The coils are composed of 460 turns of 34 AWG enameled wire wound on a cylindrical Teflon former and have a resistance of about 23 Ω and an inductance of about1 mH. The coils have a length of 6 mm and an average radius of 3.5 mm. The coils have a linear response up to 200 kHz when terminated with 2 kΩ.

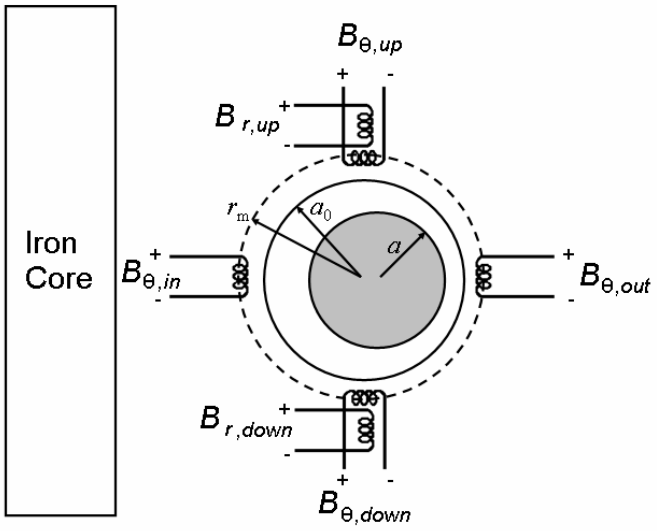

Figure 3.2: The plasma position sensing coils.

Due to the imperfect alignment of the coils with respect to the poloidal and radial directions, the coils pickup unwanted field components. The outputs of the coils must be compensated by adding a signal proportional to the current through the toroidal field coils to each of them. The amount of each waveform to be added to the position sensor outputs is determined by adjusting the gains of each waveform in the absence of a plasma until the coil signals are as close to zero as possible. It is not possible to cancel the contribution due to the Ohmic heating leakage magnetic field because this quantity is a complicated function of time due to the iron core hysteresis. However, this field is sufficiently small that it does not affect most of the magnetic measurements. The probe signals from the position sensors are sent to the control room by 20 m of RG 58/U coaxial cable where they are compensated and then integrated by gated, active integrators. An analog circuit then performs a comparison of the signals and yields an output proportional to the plasma displacement [35] which is used to drive current through the feedback coils.

3.5 4-mm Microwave Interferometer

The microwave interferometer is a standard tool for electron density measurements in plasmas. The STOR-M interferometer uses a 76 GHz (λ = 4 mm), 100 mW IMPATT (Impact Ionization Avalanche Transit-Time) oscillator to generate microwaves. These microwaves are divided amongst three paths, two reference paths (E_{R1} and E_{R2}) and a plasma path (E_p). The portion passing through the plasma (O-mode propagation) undergoes a phase shift of $\Delta\varphi$, which is proportional to the plasma density. After passing through the plasma, the microwaves pass through an E-H tuner and are split into two components, E_{s1} and E_{s2}. E_{R1} and E_{R2} pass through an attenuator and phase shifter before being mixed with E_{s1} and E_{s2} in hybrid tees. A schematic of the system is shown in Figure 3.3.

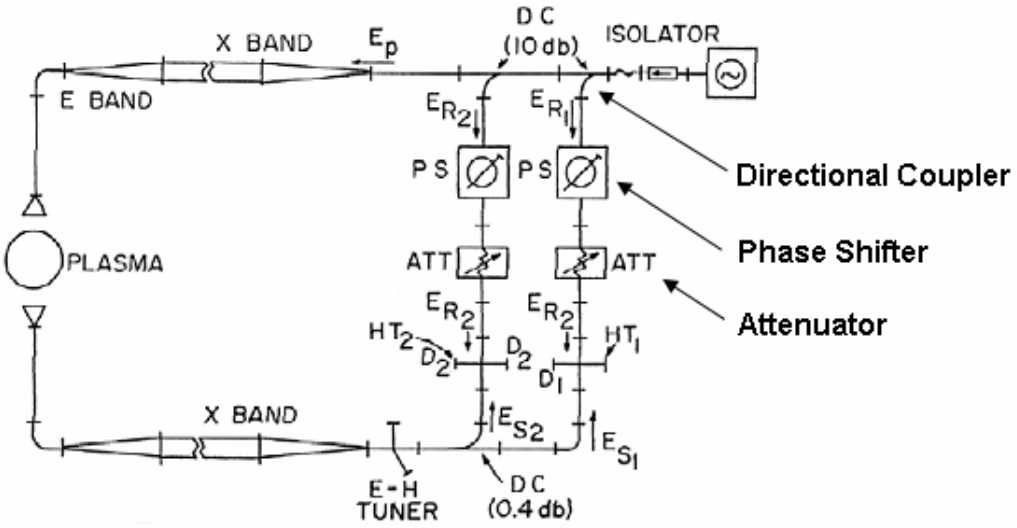

Figure 3.3: The 4mm microwave interferometer used for line averaged density measurements on STOR-M.

The microwave detectors (D1 and D2 in Figure 3.3) are 1N53 silicon point-contact diodes. The output signals of the diodes are fed into buffer amplifiers with adjustable gains to compensate for different efficiencies. If the phase shifts are adjusted correctly, the two signals are

$$V_1 = K_1 \sin \Delta\varphi \,, \tag{3-11}$$

$$V_2 = K_2 \cos \Delta\varphi \,. \tag{3-12}$$

The chord averaged density can be determined from [37]

$$\Delta\varphi = \int k_{plasma} dl - \int k_0 dl = \int (N-1)\frac{\omega}{c} dl \,, \tag{3-13}$$

where k_{plasma} is the wavenumber for the microwaves in the plasma, k_0 is the wavenumber in free space, ω is the microwave frequency and c is the speed of light. N is the index of refraction in the plasma and is given by

$$N \equiv \frac{kc}{\omega} = \sqrt{1 - \left(\frac{\omega_p}{\omega}\right)^2} \approx 1 - \frac{n_e}{2n_c} \,, \tag{3-14}$$

where $\omega_{pe} = \left(n_e e^2 / \varepsilon_0 m_e\right)^{\frac{1}{2}}$ is the plasma frequency and $n_c = m_e \varepsilon_0 \omega^2 / e^2$ is the cut-off density at which the O-mode wave can no longer propagate in the plasma. Equation 3-14 assumes that n_e is much less than n_c. For the STOR-M interferometer, n_c is about 7×10^{19} m^{-3} and n_e is about 5×10^{18} m^{-3}, so this assumption is reasonable. The density is then determined by counting fringes between the $\cos\Delta\varphi$ and $\sin\Delta\varphi$ The fringe counting circuit in STOR-M has a resolution of a quarter fringe [33].

3.6 Optical Spectrometer

A qualitative indication of the quality of confinement and plasma purity can be obtained by measuring the intensity of line emissions from hydrogen and impurity elements in the plasma. The H_α radiation represents the recycling of process of plasma particles in the plasma edge region. A lower H_α emission intensity is an indication of better plasma confinement.

STOR-M is equipped with a SPEX-1702, 0.75 m focal length Czerny-Turner scanning spectrometer with a relative aperture of f/7 and a dispersion of 10 Å/mm at 5000 Å. The Bausch & Lomb diffraction grating has 1200 lines/mm and is blazed at 5000 Å. A fiber optic probe, composed of bundles of glass fibers with optical lenses at each end, is used to transmit the light from the plasma to the entrance slit of the spectrometer. The optical probe is mounted on a side port to monitor the H_α line, which is viewed through a horizontal chord at the plasma edge. The entrance and exit slits of the spectrometer have a height of 10 mm and a width of 100 μm. The dispersed light is detected using a photomultiplier, which is shielded from the magnetic field with μ-metal and enclosed in a brass and copper housing. The photocathode and shield are negatively biased with 1.2 kV and the anode is grounded through a 5.6 kΩ output resistor. Since this is a qualitative diagnostic, only the relative intensity is necessary and it is not crucial to have a calibrated output. The signal is sent to the control room on 20 m of RG 58/U coaxial cable where it is amplified to an appropriate level before being received by the data acquisition system.

3.7 Langmuir Probes

A Langmuir probe is a small conductor tip (or an arrangement of conductors) that is inserted into a plasma and biased relative to the vacuum chamber. The potential drop is restricted to a region around the conductor tip known as the sheath that is a few Debye lengths λ_D in thickness. The Debye length is given by $\lambda_D = \left(\varepsilon_0 T_e / e^2 n_0\right)^{1/2}$, where n_0 is the plasma density. In the sheath, charge neutrality is violated and a strong electric field exists. The probe current is measured and the current-voltage (I-V) characteristic can be used to determine the electron temperature T_e, density n_e and the plasma potential V_p. If the unperturbed ions and electrons have a Maxwellian distribution, then the current density J that flows to the probe is given by

$$J = J_e(V) - J_{i0} = J_{e0}\left(\mathrm{e}^{-e(V-V_p)/T_e} - \sqrt{\frac{2\pi}{\mathrm{e}}}\sqrt{\frac{m_e}{m_i}}\right), \tag{3-15}$$

where $J_{e0} = en_0\sqrt{T_e/2\pi m_e}$ is the electron saturation current density, $J_{i0} = en_0\sqrt{T_e/\mathrm{e}m_i}$ is the ion saturation current density, V is the probe potential and V_p is the plasma space potential. Note that e = 2.718…, not to be confused with the electronic charge e. An example of a I-V characteristic curve for a Langmuir probe is shown in Figure 3.4. The potential adopted by a floating probe is called the floating potential V_f.

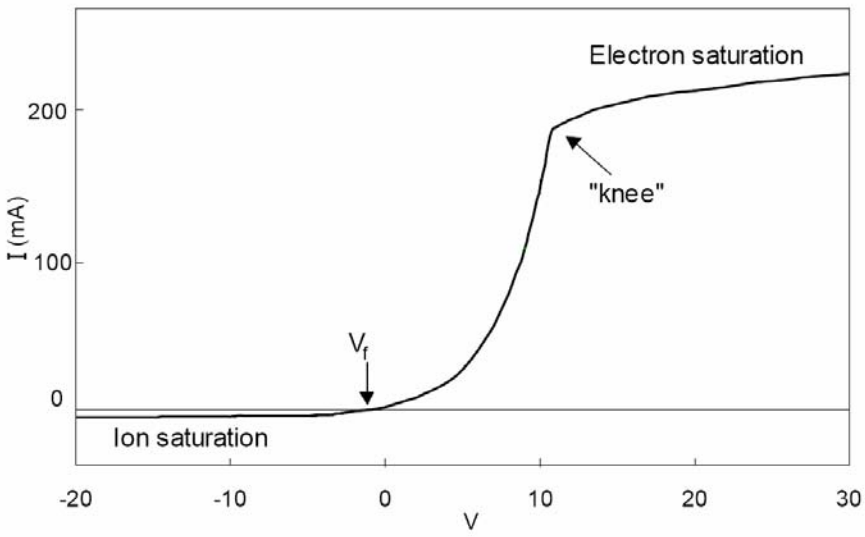

Figure 3.4: An example of an I-V curve for a Langmuir Probe.

The electron temperature T_e can be obtained from an experimentally obtained I-V curve by taking the slope of the $\ln(I\text{-}I_{i0})$ curve, where I is the measured current and is simply the product of J and the probe area A and I_{i0} is the ion saturation current. The slope of this curve is equal to e/T_e. An example of this is shown in Figure 3.5.

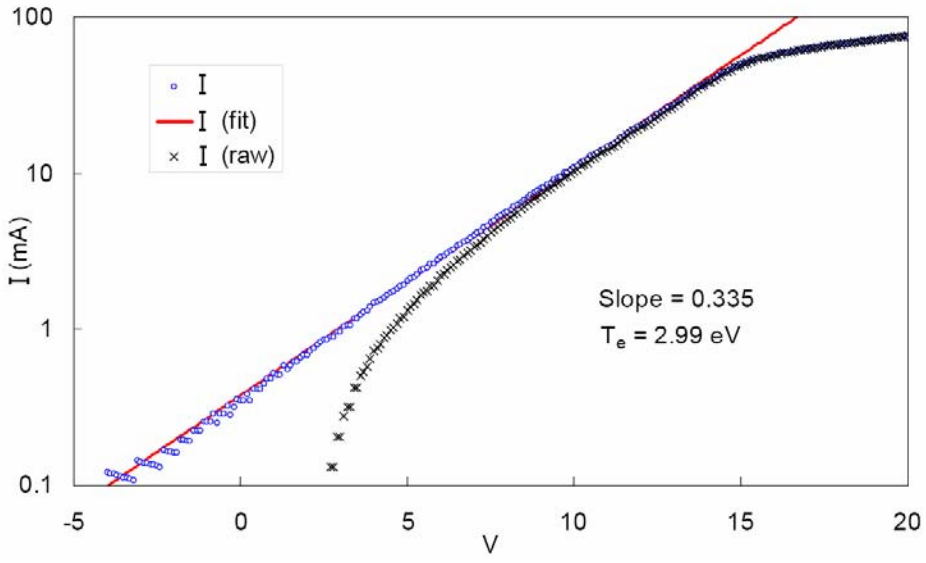

Figure 3.5: An example of a graphical measurement of T_e from the slope of $\ln(I - I_{i0})$ vs the probe voltage V. The black crosses indicate the raw data, the blue circles represent the corrected data $I\text{-}I_{i0}$ and the red line is the fit to the slope [38].

The plasma space potential V_p is taken as the point where the electron current I_e deviates from exponential growth. This point can be determined by taking the derivative of the measured current with respect to the probe voltage, dI/dV. The voltage corresponding to the minimum of dI/dV, or where d^2I/dV^2 is zero is the plasma space potential V_p (see Figure 3.6).

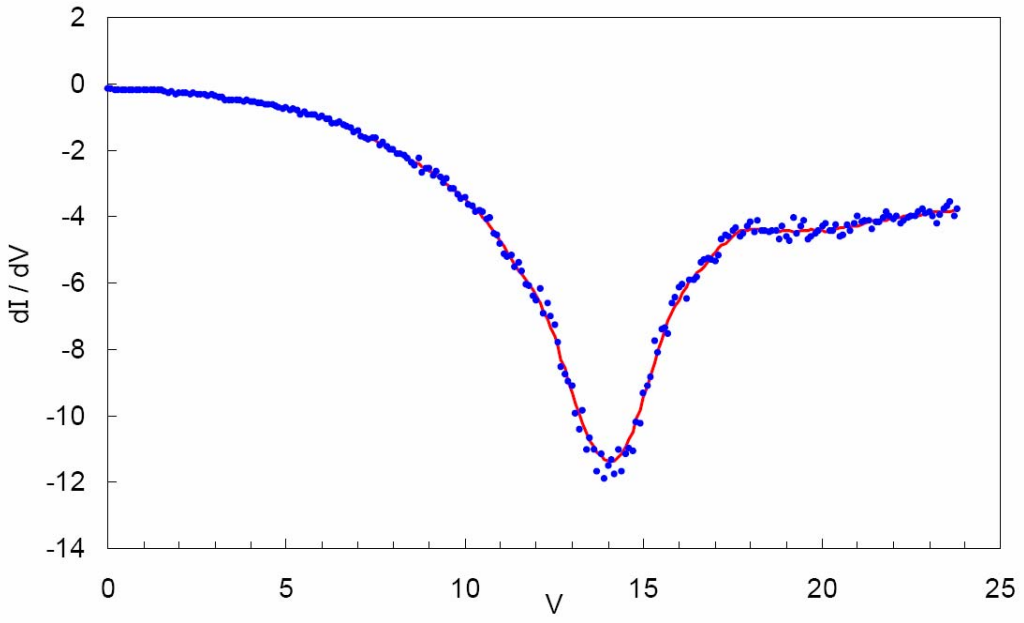

Figure 3.6: An example of a plot of dI/dV versus V. The minimum corresponds to the plasma space potential [38].

Since measurements of V_p require the complete I-V curve, the time resolution of measurements of V_p is severely limited. Therefore, it is sometimes necessary to estimate V_p using the floating potential V_f and the electron temperature T_e using the expression

$$V_f = V_p - T_e \ln \sqrt{\frac{em_i}{2\pi m_e}} \simeq V_p - 3.3T_e, \qquad (3\text{-}16)$$

for a hydrogen plasma [39]. Here the electron temperature is in eV.

Langmuir probes can be used for measurements of density, temperature, plasma floating potential, plasma space potential as well as density and potential fluctuations.

The use of Langmuir probes is restricted to the edge and SOL (scape-off layer) of the plasma so that the plasma is not seriously perturbed and to avoid damage to the probes.

3.8 Mirnov Coils

A Mirnov coil is a modified Rogowski coil with variable winding density. The coil can be wound to measure different modes of fluctuation in the poloidal magnetic field. The poloidal magnetic field B_θ can be Fourier expanded as follows:

$$B_\theta(\theta) = B_{\theta 0} + \sum_{m=1}^{\infty}\left[C_m \cos\left(m\theta\right) + S_m \sin\left(m\theta\right)\right], \tag{3-17}$$

where $B_{\theta 0}$ is the unperturbed poloidal field. The periodicity of the magnetic fluctuations is because the solution must be periodic around the poloidal angle θ.

STOR-M has two Mirnov coils for $m = 2$ and $m = 3$ where the variable winding density is accomplished with a step function approximation. There is another Mirnov coil with 12 magnetic coils with individual outputs for each coil. This allows the output signals of the coils to be numerically combined to give the signal for the $m = 2$, $m = 3$ and $m = 6$ modes.

Chapter 4

Theory

4.1 Introduction

This chapter begins with a description of H-mode and mechanisms by which it can be induced in STOR-M. Following this the role of plasma flows and the radial electric field in the improved confinement observed during H-mode is explored. Next several mechanisms by which plasma flows may be generated are presented. This is followed by the theoretical model adopted for measuring plasma flows by means of a Mach probe that is inclined to the magnetic field in a tokamak.

4.2 H-Modes

It is not sufficient to use Ohmic heating alone to heat a plasma to the temperatures required for fusion. Ohmic heating becomes ineffective at temperatures above 1 keV [2]. Therefore, auxiliary heating using either beams of energetic particles or RF waves is required to further heat the plasma to the temperatures necessary for fusion. Typically in large tokamaks the plasma is first Ohmically heated up to about 1 keV at which point auxiliary heating is engaged to heat the plasma further. It is observed, however, that the energy confinement time degrades with increasing heating power [40] and the energy confinement time with auxiliary heating is less than that for a discharge with only Ohmic heating.

In 1982 a new regime of confinement was discovered on the Axially Symmetric Divertor Experiment (ASDEX) during neutral-beam-heated discharges [17]. It was observed that for neutral-beam heating power above 1.9 MW the energy confinement time abruptly increased, approaching that of the Ohmic heating phase. This is referred to

as high confinement mode (H-mode), while the normal mode with auxiliary heating is referred to as low confinement mode (L-mode) This behaviour has been subsequently observed in many other tokamaks (see, for example, [41, 42, 43]) as well as in stellarators [44]. A measure of the improvement in confinement is the improvement factor H given by [2] as

$$H = \frac{\tau_E}{\tau_E^L}, \tag{4-1}$$

where τ_E^L is the energy confinement time of L-mode. H is typically 2 or greater during H-mode.

It has been observed that the transition to H-mode occurs at a critical minimum heating power threshold. An understanding of this power threshold is necessary for the construction of future tokamaks, such as ITER, and significant efforts to understand this minimum power threshold have been made [45]. The L-H transition is quite interesting, as it is not often that a physical system organizes itself into a state of higher energy and reduced turbulence with the addition of free energy.

The change in confinement during H-mode is first apparent at the plasma edge where there is a rapid increase in the plasma pressure, mainly due to an increase in the edge plasma density. Other characteristics include an increase in the radial electric field, a decrease in density and magnetic fluctuations, a decrease in the H_α (hydrogen) emission due to improved confinement at the plasma edge (reduced particle recycling) and an increase in the poloidal plasma velocity [46]. This increase in confinement at the edge can be thought of as a transport barrier, a narrow region of reduced energy and particle diffusion near the edge of the plasma with a modified electric field and an increased pressure gradient and plasma flow (this is known as an edge transport barrier and should be distinguished from an internal transport barrier (ITB) [47]).

Operating modes similar to H-mode have also been observed on machines without the use of auxiliary heating. These improved confinement modes have been induced by both turbulent heating [26, 48], electrode biasing [28, 49, 50] and compact torus injection [29].

4.2.1 Turbulent Heating

Turbulent heating was initially put forward as a method to heat a plasma to the temperatures required for fusion. Turbulent heating is based on the principle that by driving a sufficiently large current through a plasma, instabilities in the plasma are created that give a resistivity that is much higher than the classical Spitzer resistivity [51]. If the duration of the pulse is much shorter than the anomalous magnetic diffusion time, then the current is deposited on a skin layer in the plasma [52]. This results in preferential heating of the edge region of the plasma and a rapid transport of energy from the edge region to the plasma core. On some machines [26, 48] a period of improved confinement following the current pulse has been observed.

4.2.2 Electrode Biasing

Measurements in the plasma edge region show that there is significant enhancement (increase or decrease) of the radial electric field during H-mode discharges [53, 54]. This has led to the idea of directly altering the edge radial electric field using an externally applied voltage [55]. The edge region of the plasma may be biased in a number of ways: by inserting a electrode into the plasma edge and applying a voltage to it with respect to the vacuum chamber [55] or by applying a voltage to the limiter or divertor plate with respect to the vacuum chamber [56]. Improved confinement has been observed on many tokamaks using electrode biasing.

4.3 The Role of Plasma Drifts and the Radial Electric Field in Improved Confinement

There are many theories as to how the transition from L-mode to H-mode (L-H transition) occurs in tokamaks. Most of these theories agree on the critical role played by changes in the radial electric field and the poloidal flow. Specifically, it has been shown that a sheared poloidal flow can have a strong decorrelation effect on plasma turbulence and can therefore improve energy confinement [57].

4.3.1 Plasma Flows

The fluid equation of motion for each species in a plasma can be written as

$$m_j n_j \left[\frac{\partial \vec{v}_j}{\partial t} + \left(\vec{v}_j \bullet \vec{\nabla} \right) \vec{v}_j \right] = q_j n_j \left(\vec{E} + \vec{v}_j \times \vec{B} \right) - \vec{\nabla} p_j , \tag{4-2}$$

where the subscript *j* denotes the species (hydrogen ion, electron, etc.), *m* is the mass, *n* is the density, *v* is the velocity, *q* is the charge, *E* is the electric field, *B* is the magnetic field and *p* is the pressure. For drifts that are slow compared with the time scale of the cyclotron frequency ω_{cj} the term $\partial \vec{v}_j / \partial t$ is ignorable. The term $\left(\vec{v}_j \bullet \vec{\nabla} \right) \vec{v}_j$ can be ignored if $\vec{E}$ and $\vec{\nabla} p_j$ are in the same direction. Ignoring these two terms the equation can be rewritten as

$$q_j n_j \left(\vec{E} + \vec{v}_j \times \vec{B} \right) - \vec{\nabla} p_j = 0 . \tag{4-3}$$

Taking the cross product of 4-3 with $\vec{B}$ in this limit gives the equation for the drifts perpendicular to $\vec{B}$:

$$\vec{v}_\perp = \vec{v}_{\vec{E} \times \vec{B}} + \vec{v}_{*j} , \tag{4-4}$$

where

$$\vec{v}_{\vec{E} \times \vec{B}} = \frac{\vec{E} \times \vec{B}}{B^2} \tag{4-5}$$

is the $\vec{E} \times \vec{B}$ drift velocity and

$$\vec{v}_{*j} = -\frac{\vec{\nabla} p_j \times \vec{B}}{n_j q_j B^2} \tag{4-6}$$

is the diamagnetic drift velocity. The $\vec{E} \times \vec{B}$ drift is the same in magnitude and direction for both ions and electrons whereas the diamagnetic drift is in opposite directions and generally the magnitude for different species is not the same. Hence the diamagnetic drift results in a current whereas the $\vec{E} \times \vec{B}$ drift does not.

4.3.2 The Radial Force Balance Equation

The equation of motion for ions and electrons can be used to derive the radial force balance equation for a tokamak plasma. The physics that influences the radial

electric field E_r can be discussed in terms of the lowest order radial force balance equation. This equation can be derived from 4-3 and is written as

$$E_r = \frac{1}{n_i Ze}\frac{\partial p_i}{\partial r} - \left[\vec{v}\times\vec{B}\right]_r = \frac{1}{n_i Ze}\frac{\partial p_i}{\partial r} + v_\phi B_\theta - v_\theta B_\phi, \tag{4-7}$$

where the subscripts r, ϕ and θ indicate, respectively, the radial, toroidal and poloidal directions. This equation indicates that there is a connection between the radial electric field E_r, the radial pressure gradient $\partial p_i/\partial r$, the toroidal flow velocity v_ϕ and the poloidal flow velocity v_θ. It is difficult to determine the temporal causality of these terms, that is, which causes which. This is due to the very short timescale of the L-H transition. As a result determining the trigger of H-mode has been very difficult theoretically and experimentally.

4.3.3 Decorrelation of Turbulence by Poloidal Velocity Shear

The main concept behind the decorrelation of turbulence by velocity shear is that turbulent structures in the plasma are torn apart by the relative motion of adjacent fluid layers. This results in a reduction in the correlation length of the turbulence, a reduction in the ambient turbulence level and a reduction in the turbulence driven anomalous transport.

The criterion for a velocity shear to cause a reduction in turbulence is related to the shearing rate, given by [58]

$$\omega_s = k_{0y}\Delta r_t \left|\frac{\partial v_\theta}{\partial r} - \frac{v_\theta}{r}\right|, \tag{4-8}$$

where ω_s is the shearing rate and k_{0y}^{-1} and Δr_t are the spatial correlation lengths of the ambient turbulence in the poloidal and radial directions, respectively. The term $\left|\partial v_\theta/\partial r - v_\theta/r\right|$ describes the deviation of the poloidal flow profile from that of a rigid body, for which there would be no shearing. Equation 4-8 describes the rate at which two fluid elements separated radially by Δr_t become separated by k_{0y}^{-1} poloidally. Also of importance is the decorrelation time associated with turbulent radial diffusion of fluctuations by the ambient turbulence

$$\Delta\omega_t = \frac{4D}{\Delta r_t^2}, \tag{4-9}$$

where D is the anomalous diffusion coefficient.

For the strong shear regime ($\omega_s > \Delta\omega_t$), it can be shown that the radial correlation length becomes [58]

$$\Delta r_c = \left(\frac{\Delta\omega_t}{\omega_s} \right)^{1/3} \Delta r_t, \tag{4-10}$$

where Δr_c is the radial correlation length in the presence of a velocity shear. In addition to a reduction in the radial correlation length of the turbulence, there is also a reduction in the fluctuation levels in the plasma according to

$$\frac{\left\langle \left| \tilde{\xi}/\xi_0 \right| \right\rangle_{\omega_s}}{\left\langle \left| \tilde{\xi}/\xi_0 \right| \right\rangle_{\omega_s=0}} \approx \left(\frac{\Delta\omega_t}{\omega_s} \right)^{2/3}, \tag{4-11}$$

where the subscript ω_s refers to the strong shear case and $\omega_s = 0$ refers to the ambient turbulence case and ξ is the fluctuating field (T_i in the case of ion-temperature-gradient-driven turbulence or p in the case of resistive pressure-gradient-driven turbulence for instance). Also, since the turbulent diffusion coefficient is given by $D = \sum_{\vec{k}} F \left[\left\langle \left| \tilde{\xi}/\xi_0 \right|^2 \right\rangle_{\vec{k}} \right] \tau_f$, where $\tau_f \approx \left(\omega_s^2 \Delta\omega_t \right)^{1/3}$ is the rate at which the relative separation between two adjacent fluid elements becomes comparable to the fluid blob size, the transport level is reduced in the strong shear regime.

4.3.4 Stabilization of Modes by Poloidal Velocity Shear

Poloidal velocity shear can cause linear stabilization of modes, which leads to transport reduction. Much of the physics of mode stabilization is mode specific making it difficult to discuss in general [59, 60, 61, 62]. There is one general effect that persists across a number of different modes, and that is that the presence of an $\vec{E} \times \vec{B}$ velocity shear results in enhanced damping by coupling the unstable modes to nearby stable modes [63]. For the case of long-wavelength drift waves, a velocity shear enhances ion

damping by shifting the eigenmode structure away from the resonant ($\vec{k} \cdot \vec{B} = 0$) surface [61]. The ion-temperature-gradient-driven modes are stabilized when the shearing frequency ω_s exceeds the mode growth rate as a consequence of the coupling of radial eigenmodes and absorption and damping due to resonance between the wave frequency and the shear frequency [62].

4.3.5 Destabilization of the Kelvin-Helmholtz Instability

In neutral fluid dynamics a sheared velocity is normally thought of as a source of free energy which can drive turbulence through Kelvin-Helmholtz instabilities [64]. In a magnetized plasma the Kelvin-Helmholtz instability can be rendered ineffectual by magnetic shear [63]. The physical mechanism behind this is that the magnetic shear prevents coupling of modes across the velocity gradient so that they are unable to extract energy from the velocity shear and grow. For the case of the resistive Kelvin-Helmholtz instability, the stability criterion can be written as [58]

$$\frac{1}{E_r}\frac{\partial E_r}{\partial r} < \left(\frac{1}{4\pi\varepsilon_0 \eta \Delta\omega_D}\right)^{1/4} \left(\frac{V_A k_y}{L_s c}\right)^{1/2}, \tag{4-12}$$

where η is the plasma resistivity, $\Delta\omega_D$ is the turbulence decorrelation rate, V_A is the Alfvén speed, k_y is the poloidal wave number of the turbulent mode and L_s is the magnetic shear length. This criterion would be most easily violated in the edge of the plasma during H-mode when $\partial E_r / \partial r$ and η are large. Typical H-mode parameters show that there is no significant instability [63]. However, K-H instability may play roles in the nonlinear stage of instabilities, for instance, in zonal flow formation [65] and turbulence suppression [66].

4.4 Mechanisms of Flow Generation

Although it is evident that a sheared poloidal flow results in an increase in confinement, it is not clear what causes the flow velocity (and shear) increase. Several mechanisms have been proposed, including ion orbit losses at the plasma edge [67], Stringer spin-up [68] and Reynolds Stress [69]. A brief overview of these mechanisms is given below.

4.4.1 Ion-Orbit Loss

Within about one poloidal ion gyroradius $\rho_{\theta i}$ ($\rho_{\theta i} = \sqrt{2}\, m_i v_T / q_i B_\theta$, where v_T is the thermal velocity) from the plasma boundary, the ion-orbit can either intersect the limiter or cross the separatrix, and be removed from the plasma [70, 71]. This produces an ion-orbit loss current which must be balanced by a return current driven by a negative electric field. This electric field can drive a poloidal torque, resulting in an increase in the poloidal flow velocity in the edge region of a tokamak plasma.

Low-energy collisional particles contribute to the poloidal viscosity and resist rotation. These particles are said to be in the plateau Pfirsch-Schlüter regime. High-energy collisionless particles in the banana regime contribute to the ion-orbit loss and drive a poloidal torque.

Analysis by Shaing, *et al.* [71] reveals that for decreasing collisionality ν_{*_i} there is first one solution, then three and then one solution for the poloidal flow velocity. For higher collisionality with one solution, the solution corresponds to the L-mode. For median values of collisionality, one solution is unstable and of the two other solutions one corresponds to the L-mode and the other corresponds to the H-mode. This bifurcated solution means that the plasma can exist in either L-mode or H-mode for the same set of plasma parameters. Bifurcated solutions are a common theme in the L-H transition in tokamaks and similar devices [72, 73, 74]. The solution for the lowest collisionality corresponds to the H-mode.

The typical scenario for an increase in the poloidal rotation velocity due to ion-orbit loss would be as follows. Due to plasma heating, ν_{*_i} in the edge region decreases. At some critical value of ν_{*_i} that depends on the device parameters, v_θ increases abruptly; this corresponds to the transition from L-mode to H-mode.

4.4.2 Anomalous Stringer Drive

The idea that a tokamak plasma can spontaneously begin rotating poloidally (spin-up) was first put forward by Stringer who showed that, in the presence of Pfirsch-Schlüter particle diffusion, poloidal rotation is unstable [75, 76]. That is, if a state with no poloidal rotation were perturbed by a small amount the poloidal rotation would grow exponentially. It was later shown that the damping rate

of poloidal rotation due to either parallel viscosity or magnetic pumping was so large that Stringer spin up was considered an unimportant mechanism of flow generation [77, 78, 79]. An important feature of the Pfirsch-Schlüter diffusion required to drive the Stringer spin-up is that it must be poloidally asymmetric [68]. A substantial amount of circumstantial evidence indicates that the anomalous particle transport in tokamaks is poloidally asymmetric [80, 81]. Since the anomalous particle diffusion greatly exceeds the Pfirsch-Schlüter particle diffusion, the anomalous Stringer drive is large and can exceed the damping rates due to parallel viscosity or magnetic pumping.

A more rigorous study of Stringer spin-up [68, 82, 83] shows the non-linear interplay between the poloidal spin-up and turbulence driven anomalous transport leads to a bifurcation in the density equilibrium similar to that observed in the L-H transition in tokamaks. A non-linear simulation of the equilibrium and stability of axisymmetric toroidal edge plasma in the presence of anomalous ballooning-like transport shows that for weak magnetic pumping, a large poloidal rotation on the order of the ion sound speed c_s ($c_s = \sqrt{(T_e + T_i)/m_i}$) is driven, forming a localized shear layer [84]. Additionally, poloidally asymmetric particle and toroidal momentum sources such as pellet injection, neutral beam injection and compact torus injection may trigger the Stringer instability and drive poloidal rotation [85].

4.4.3 Reynolds Stress

The Reynolds stress is a measure of the degree of anisotropy in the structure of fluctuations in a fluid. A radially varying Reynolds stress allows the turbulence to rearrange the profile of the poloidal momentum generating sheared poloidal flows [86]. The poloidal flow profile evolution equation can be written as [69]

$$\frac{\partial v_\theta}{\partial t} = -\frac{\partial}{\partial r}\left\langle \tilde{v}_r \tilde{v}_\theta \right\rangle - \mu_\theta v_\theta , \tag{4-13}$$

where $\tilde{v}_r$ and $\tilde{v}_\theta$ are the fluctuating values of the radial and poloidal flow velocities, μ_θ is the damping rate of the poloidal flow and $\langle ... \rangle$ denotes time averaging. The dominant contribution to the poloidal damping is due to magnetic pumping as the plasma passes through the inhomogeneous magnetic field [79]. The poloidal flow damping rate can be expressed as:

$$\mu_\theta \approx \gamma_{mp} \simeq \frac{3}{4}\left(1+\frac{1}{2q^2}\right)^{-1}\left(\frac{l}{qR}\right)^2 \nu_{ii}, \tag{4-14}$$

where γ_{mp} is the magnetic pumping rate, q is the safety factor, l is the mean-free path, R is the distance from the major axis of the torus and ν_{ii} is the ion-ion collision rate.

From 4-13 it is evident that if the Reynolds stress ($\langle \tilde{v}_r \tilde{v}_\theta \rangle$) is non-zero and has a radial gradient then the poloidal flow may be accelerated. A dilemma appears since the stress is produced by fluctuations and fluctuations are suppressed during H-mode. This may be resolved in a few ways. The poloidal acceleration arises as a result of the radial gradient of the Reynolds stress, which is not necessarily correlated with the fluctuation amplitudes. Additionally, the phases of $\tilde{v}_r$ and $\tilde{v}_\theta$ may be more important than their amplitudes, meaning that $\langle \tilde{v}_r \tilde{v}_\theta \rangle$ could be larger despite a reduction in the fluctuation amplitudes. Observations on several machines indicate that $\partial/\partial r \langle \tilde{v}_r \tilde{v}_\theta \rangle$ is in fact enhanced during H-mode [87, 88] and may be dominant in driving the observed poloidal flow during H-mode.

The Reynolds stress can be experimentally measured using a Langmuir probe with three tips oriented such that two tips are separated poloidally and the third is separated radially from the other two to measure the radial and poloidal gradient of the floating potential. The probes are used to measure the floating potential in the plasma. The term $\langle \tilde{v}_r \tilde{v}_\theta \rangle$ can then be related to the floating potential through

$$\langle \tilde{v}_r \tilde{v}_\theta \rangle = \left\langle -\frac{\nabla_\theta \tilde{V}_p \nabla_r \tilde{V}_p}{B^2} \right\rangle = \left\langle -\frac{\nabla_\theta \tilde{V}_f \nabla_r \tilde{V}_f}{B^2} \right\rangle \tag{4-15}$$

since the plasma potential fluctuations are expected to be the same as floating potential fluctuations. This makes the Reynolds stress the most practical to measure of the three flow generation mechanisms described here.

4.5 Fluid model of Ion Collection by a Mach Probe

The parallel plasma flow velocity is often measured by means of a Mach probe, with two collecting areas oriented perpendicular to $\vec{B}$ and separated by an insulator. Hutchinson has shown that the ratio of the upstream to downstream saturation currents collected by the probe can be related to the unperturbed parallel flow velocity [89, 90]. The basic idea in this one-dimensional modeling is that particle transport consists of fast parallel flow balanced by a slow, cross-field diffusion into the quasineutral presheath, terminating on the magnetic presheath entrance (MPSE). The quasineutral presheath has the form of a magnetic flux tube as shown in Figure 4.1.

It is also of interest to measure the perpendicular flow velocity (a perpendicular flow being in the magnetic surface, but perpendicular to $\vec{B}$). Hutchinson has shown that for a probe oriented perpendicular to $\vec{B}$ the saturation current does not depend on the specific cross-field process, whether it is cross-field diffusive, or a coherent flow [91]. These processes simply adjusts the length of the presheath, the distance over which the density and parallel velocity adjust themselves from their values at infinity to those imposed by the boundary conditions at the MPSE. The one-dimensional viscous diffusive cross-field model [89, 90] and coherent cross-field flow model [91] give essentially the same results.

In order to measure the perpendicular flow velocity, the collecting surfaces must be inclined with respect to the plane normal to the magnetic field. Several experiments have reported that the ratio of upstream to downstream saturation current collected by an inclined Mach probe is affected by a perpendicular flow [25, 92, 93, 94].

Van Goubergen [95] presents an extension of Hutchinson's one-dimensional theory [89, 90] to allow for the determination of perpendicular flow. The following is a derivation of this model.

4.5.1 Formulation

The model probe consists of two flat conductors separated by an insulator. The probe is oriented such that the normal to the surface of either conductor lies in the magnetic flux surface; the surface normal of the collector is perpendicular to the radial direction. The probe is inclined to the magnetic field and the angle θ of inclination is

measured between $\vec{B}$ and the surface of the probe (see Figure 4.1). The parallel, perpendicular and radial coordinates are referred to as Z, X and r respectively; the coordinates x and y are parallel and perpendicular to the probe surface.

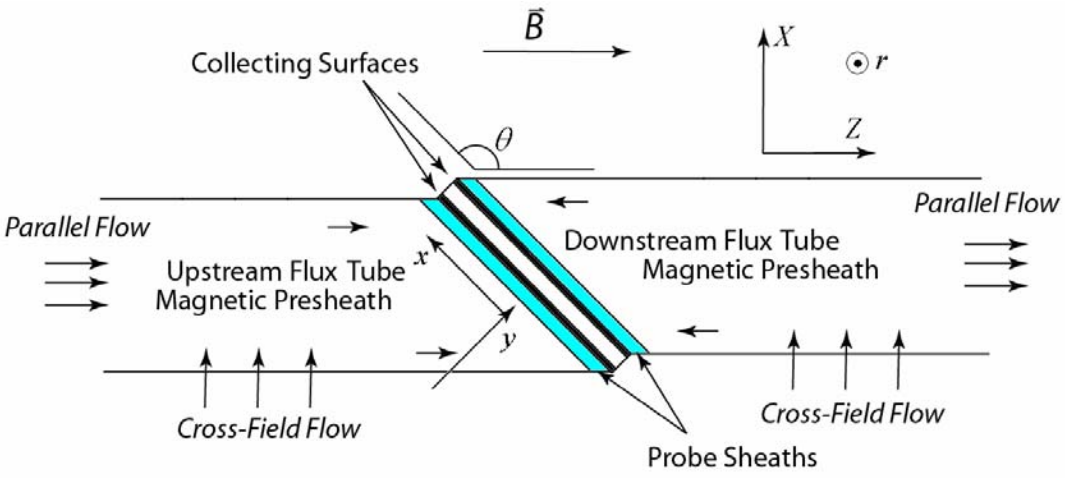

Figure 4.1: Geometry of a Mach probe inclined to the magnetic field.

The probe size a is much larger than the ion gyroradius ρ_i. The equations governing the probe are the three-dimensional ion continuity (4-16) and the parallel projection of the total momentum (4-17).

$$\frac{\partial}{\partial Z}\left(n_i v_{\parallel}\right)+\frac{\partial}{\partial X}\left(n_i v_{\perp}\right)+\frac{\partial}{\partial r}\left(n_i v_r\right)=0\,, \tag{4-16}$$

$$\frac{\partial}{\partial Z}\left(m_i n_i v_{\parallel}^2\right)+\frac{\partial}{\partial X}\left(m_i n_i v_{\parallel} v_{\perp}\right)+\frac{\partial}{\partial r}\left(m_i n_i v_{\parallel} v_r\right)-\eta\frac{\partial^2 v_{\parallel}}{\partial r^2}=-\nabla_{\parallel} p_i+Zen_i E_{\parallel}\,, \tag{4-17}$$

Here, n_i, m_i, p_i and v are the ion density, ion mass, ion pressure and fluid velocity. Ze is the effective charge on the ion and E is the electric field. The subscripts || and $\perp$ denote the directions parallel and perpendicular to the magnetic field. The shear viscosity η is given by $\eta = \alpha m_i n_i D$, where D is constant anomalous cross-field diffusion coefficient and α is the ratio of the shear-viscosity to the diffusivity and can take values between 0 and 1. An assumption is made that in the cases of interest (e.g. collecting ion saturation current) the majority of electrons are repelled by the negatively biased probe so that their density is governed by a Boltzmann factor. The electron density can be written as

$$n_e = Zn_\infty \exp\left(\frac{eV}{T_e}\right), \tag{4-18}$$

where n_e, n_∞, V and T_e are the electron density, unperturbed ion density, potential and the electron temperature. In the quasineutral plasma region the electric field can be related to the ion density through

$$E_\parallel = -\nabla_\parallel\left(\frac{T_e}{e}\right)\ln\left(\frac{n_i}{n_\infty}\right) = -\left(\frac{T_e}{e}\right)\nabla_\parallel n_i . \tag{4-19}$$

The following non-dimensionalizing transformations are made:

$$n = \frac{n_i}{n_\infty},\ M_\parallel = \frac{v_\parallel}{c_s},\ M_\perp = \frac{v_\perp}{c_s},\ Z' = \left(\frac{D}{c_s a^2}\right)Z,\ X' = \left(\frac{D}{c_s a^2}\right)X,\ r' = \frac{r}{a}. \tag{4-20}$$

The primes on the new coordinates are dropped after transformation. Equations 4-16 and 4-17 can now be transformed into a one-dimensional model. The cross-field gradients over the radial dimension are linearized by replacing $\partial\psi/\partial r$ by $(\psi_\infty - \psi)/a$ and $\partial^2\psi/\partial r^2$ by $(\psi_\infty - \psi)/a^2$, where ψ is a general variable for the flow velocity and density. The probe acts as a sink for particles, so the radial diffusive influx can be given by $n_i v_r = -D\partial n_i/\partial r$. The equations are then transformed to the (x,y) coordinate system using the transformations:

$$Z = x\sin\theta - y\cos\theta,\ X = x\cos\theta + y\sin\theta . \tag{4-21}$$

The main assumption is that the parameters do not vary along the probe surface, $\partial/\partial x = 0$. Transport equations in the y-direction are obtained and are transformed back into the (Z,X) coordinate system. It is assumed that the perpendicular velocity does not vary along the probe surface, $\partial M_\perp / \partial x = 0$. With these assumptions and transformations, the transport equations can now be written as

$$\frac{\partial n}{\partial Z} = \frac{\left(M_\parallel - M_\perp\cot\theta\right)\left(1-n\right) - \left(M_{\parallel\infty} - M_\parallel\right)\left[1 - n\left(1-\alpha\right)\right]}{\left[\left(M_\parallel - M_\perp\cot\theta\right)\right]^2 - 1}, \tag{4-22}$$

$$\frac{\partial M_{\parallel}}{\partial Z} = \frac{-(1-n)+\left[\left(M_{\parallel}-M_{\perp}\cot\theta\right)\left(M_{\parallel\infty}-M_{\parallel}\right)\left[1-n(1-\alpha)\right]\right]}{n\left[\left[\left(M_{\parallel}-M_{\perp}\cot\theta\right)\right]^2-1\right]}. \tag{4-23}$$

Hutchinson has shown that α (the shear-viscosity/ diffusivity ratio) is on the order unity for the modeling of a probe in the presence of a coherent cross-field flow [90, 91]. Combining 4-22 and 4-23 and setting $\alpha = 1$ gives the transport equation

$$\frac{\partial n}{\partial M_{\parallel}} = \frac{n\left[\left(M_{\parallel}-M_{\perp}\cot\theta\right)(1-n)-\left(M_{\parallel\infty}-M_{\parallel}\right)\right]}{-(1-n)+\left[\left(M_{\parallel}-M_{\perp}\cot\theta\right)\left(M_{\parallel\infty}-M_{\parallel}\right)\right]}. \tag{4-24}$$

4.5.2 The Bohm-Chodura Boundary Condition

The results of Hutchinson [90] are recovered from 4-24 for the cases $M_{\perp} = 0$ and θ = 90º, 270º. Also, by analogy with the results of [90] the singularities in the denominators of 4-22 and 4-23 determine the parallel velocity at the MPSE. From the denominators it is seen that the maximum velocity of the parallel flow at the MPSE is given by

$$M_{\parallel,MPSE} = M_{\perp}\cot\theta \pm 1. \tag{4-25}$$

This boundary condition implies that with a probe oriented at an angle θ with a perpendicular flow with Mach number $M_{\perp}$, the parallel flow has to adapt itself so that 4-25 is fulfilled. In order to obtain the results of Hutchinson [90] for the cases $M_{\perp} = 0$ and θ = 90º, 270º, the sign in equation 4-25 must be positive to give $M_{||,MPSE} = 1$ for the probe surface facing upstream in the toroidal flow and negative to give $M_{||,MPSE}$ = -1 on the downstream side. The value of $M_{||,MPSE}$ for an inclined probe is plotted against the inclination angle of the probe in Figure 4.2. Equation 4-25 is known as the Bohm-Chodura boundary condition [96] and has been previously been derived by both Stangeby and Chankin [97] and Hutchinson [98]. It is important to note that 4-25 implies that there are no solutions to this model for values of $M_{||\infty}$, $M_{\perp}$ and θ such that $\left|M_{\parallel\infty}-M_{\perp}\cot\theta\right| > 1$ (for angles near θ = 0º, 180º). Additionally, the use of the fluid equations restricts the probe inclination to angles larger than 5º [95]. Figure 4.2 shows the Mach number for the parallel flow at the MPSE versus the inclination angle of the probe.

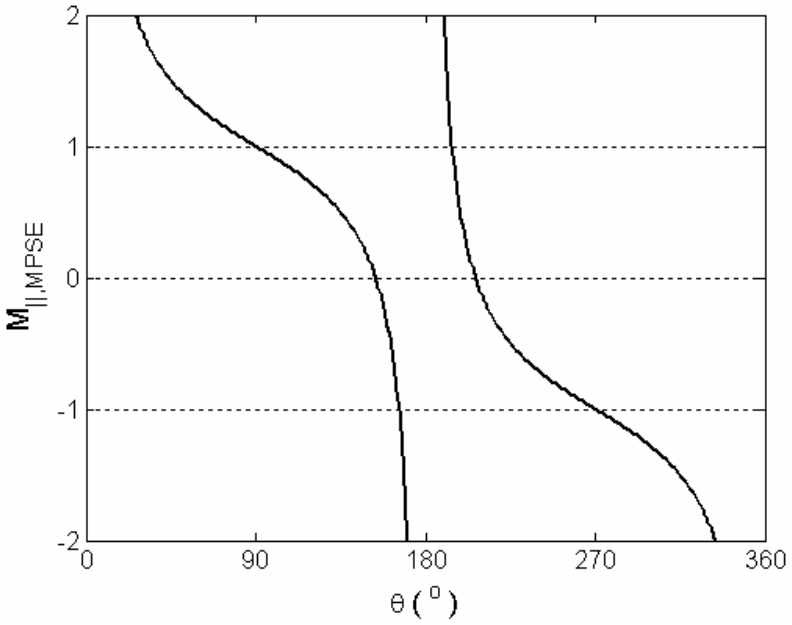

Figure 4.2: The parallel Mach number at the MPSE as a function of the inclination of the probe surface. As expected the Bohm-Chodura boundary condition gives $M_{||,MPSE} = 1$ for $\theta = 90^{o}$ and $M_{||,MPSE} = -1$ for $\theta = 270^{o}$.

4.5.3 Effective Area of Collecting Surface

It is important to understand the effect of the angle between the collecting surface and the magnetic field on the effective area of the probe A_{eff}. Since the ions collected by the collecting surface are only those traveling down the flux tube that terminates on that surface, the area of the parallel projection of the surface is the effective collecting area of the surface. A simple geometric analysis reveals that since the ions collected by the probe are moving along $\vec{B}$ and the probe is inclined to the magnetic field by an angle θ that A_{eff} is related to the actual probe area A through $A_{eff} = A\sin(\pi - \theta) = A\sin\theta$. This can be seen in Figure 4.3.

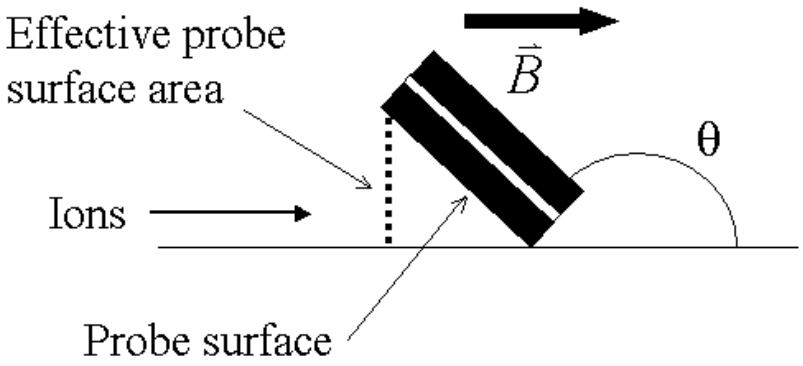

Figure 4.3: Depiction of the effective probe surface area for a probe inclined to the magnetic field at an angle θ.

4.5.4 Solving the Transport Equation

The solutions of 4-24 give $n(M_{||})$ in the presheath. This equation can be solved by starting with $n = 1$ (the density outside the presheath), a chosen parallel and perpendicular flow mach number $M_{||\infty}$ and $M_{\perp}$ and an inclination angle θ for the probe. The equation can be numerically integrated to obtain the corresponding pairs of n and $M_{||}$. Equation 4-25 is then used to find the value of $M_{||,MPSE}$, the parallel Mach number at the magnetic presheath entrance. The density n_{MPSE}, the ion density at the MPSE, is the density corresponding to this value of $M_{||,MPSE}$, which was found from the integration. Since the flow speed of ions toward the collecting surface in the sheath is the ion sound speed c_s, the current collected by the probe is

$$I_{sat} = n_{MPSE} e c_s A_{eff} = n_{MPSE} e c_s A \sin\theta \,. \tag{4-26}$$

The ratio of the saturation currents collected by two probe surfaces facing in opposite directions is normally used for analysis. This ratio can be written as

$$R = \frac{I_{sat}(\theta)}{I_{sat}(\theta+\pi)} = \frac{n_{MPSE}(\theta)}{n_{MPSE}(\theta+\pi)}, \tag{4-27}$$

since the effective areas of the two collectors are the same.

4.5.5 Approximate Analytical Solution

It is difficult to use 4-24 to relate the ratio of ion saturation currents collected by a Mach probe to $M_{||}$ and $M_{\perp}$. This is because 4-24 has to be separately integrated for every possible combination of values of $M_{||\infty}$, $M_{\perp}$ and θ and assembled into a calibration table, or used with an iterative technique. A simpler method is to adopt an approximate analytical solution as outlined by Hutchinson [89, 90] of the form

$$n \approx \exp\left(\pm M_{||\infty} \mp M_{||}\right), \tag{4-28}$$

where the sign depends on whether the probe is looking upstream or downstream.

To bring the approximate relation from 4-28 into agreement with the results of the numerical integration of 4-24, a fitting parameter $c_{\mathrm{up,down}}$ is introduced. To solve for the ion density at the MPSE, $M_{||}$ is replaced by $M_{\perp} \cot\theta \pm 1$ and 4-28 becomes

$$n_{MPSE,up,down} = \exp\left(c_{up,down}\left(\pm M_{||\infty} \mp M_{\perp}\cot\theta\right) - c_0\right), \tag{4-29}$$

where the subscripts *up* and *down* represent either the upstream or downstream side of the collector and $c_0 = -\ln(n_{\mathrm{sh}}) \approx 1.05$.

Gunn, *et. al.* [99] have shown that $c = c_{\mathrm{up}} + c_{\mathrm{down}}$ is well fitted by the expression

$$c = 2 + 0.28\exp\left(\frac{M_{||\infty}}{0.862}\right). \tag{4-30}$$

However, this form of the fitting parameter only gives an accurate fit for small values of $M_{||,\infty}$ and angles θ close to 90º. Peleman, *et al*. [100] have shown that the fitting parameter is better fit by the expression

$$c(M_{||,\infty}, M_{\perp}, \theta) = a_1\left(a_2\theta^{-1} + a_3\right), \tag{4-31}$$

where a_1, a_2 and a_3 are given by

$$a_i = a_{i,1}Z^2 + a_{i,2}Z + a_{i,3} \quad (i = 1,2,3) \quad \text{for} \begin{cases} i = 1 \Rightarrow Z = M_{||,\infty} \\ i \neq 1 \Rightarrow Z = e^{M_{\perp}} \end{cases}, \tag{4-32}$$

where the values of $a_{i,j}$ are given by the following table:

$a_{i,j}$	1	2	3
1	2.291	0	0.192
2	11.450	-18.929	7.043
3	-0.136	0.224	0.918

Table 4.1: Values of $a_{i,j}$ for 4-32 [100].

Using 4-29, 4-27 can be rewritten as

$$R = \frac{I_{sat}(\theta)}{I_{sat}(\theta+\pi)} = \exp\left(c\left(M_{||\infty} - M_{\perp}\cot\theta\right)\right). \tag{4-33}$$

Equation 4-33 can be used to obtain $M_{||\infty}$ and $M_{\perp}$ from experimental Mach probe data. Typically, the logarithm of the current ratio is used as it allows for linear fitting of the data with the expression

$$\ln(R) = c\left(M_{||\infty} - M_{\perp}\cot\theta\right). \tag{4-34}$$

A comparison of the results of the numerical integration of 4-24 with the analytical expression of 4-34 is shown in Figure 4.4.

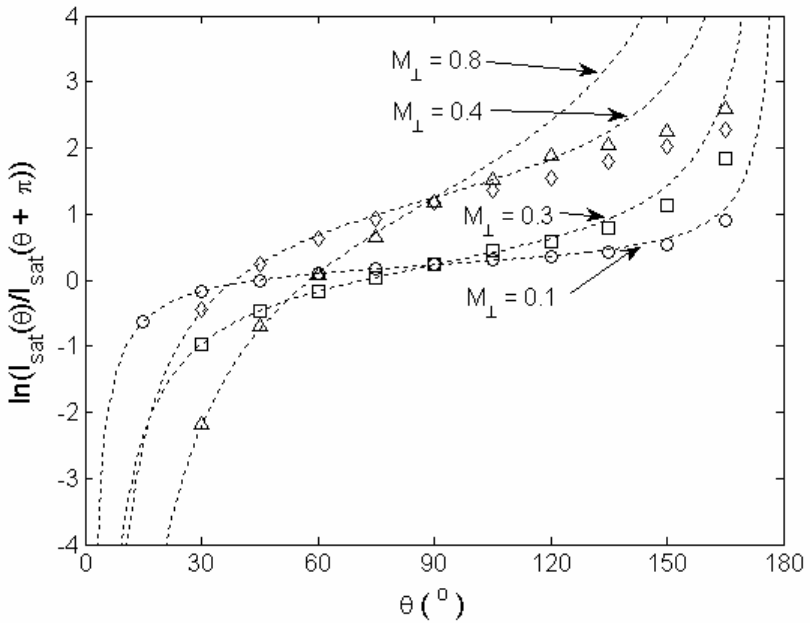

Figure 4.4: Natural logarithm of current ratio against θ for various values of $M_{||\infty}$ and $M_{\perp}$. The markers indicate the numerical solutions of 4-24 with ○, $M_{||\infty}$ = 0.1 and $M_{\perp}$ = 0.1; □, $M_{||\infty}$ = 0.1 and $M_{\perp}$ = 0.3; ◊, $M_{||\infty}$ =0.5 and $M_{\perp}$ = 0.4; Δ, $M_{||\infty}$ = 0.5 and $M_{\perp}$ = 0.8. The dashed curves are the corresponding fitted results of 4-34.

4.5.6 Round Collecting Surfaces

The Mach probe model presented is valid for mach probes with flat collectors; the angle between the collecting surface and $\vec{B}$ is constant across the surface. From a manufacturing point of view, it is easier to manufacture collectors for the Gundestrup probe with round collecting surfaces. The analysis for a probe with round conductors is significantly more complicated [101]. This is because the flux tubes change along the surface as the angle between the surface and the magnetic field changes. This means that for a round collector, the current collected is proportional to the integral of n_{MPSE} along the surface of the collector whereas for a flat collector n_{MPSE} is constant over the surface. The current collected by a round collector can be written, using 4-26 and 4-29 as

$$I_{sat,up} = br_G n_\infty e c_s e^{-c_0} e^{c_{up}|M_{||,\infty}|} \int_{\beta_0-\frac{\alpha}{2}}^{\beta_0+\frac{\alpha}{2}} \cos(\beta) e^{-c_{up}|M_\perp|\tan(\beta)} d\beta \,, \qquad (4\text{-}35)$$

where b is the radial extent of the collector, r_G is the radius of the collector surface, α is the angular extent of the collecting surface, β_0 is the angle between the normal at the middle of the collecting surface and the direction opposite to $\vec{B}$. β is the variable of integration and takes values between β_0 - $\alpha/2$ and β_0 + $\alpha/2$. Note that for the geometry of this integration, tan β = cot θ. The geometry of the curved collector is shown in Figure 4.5.

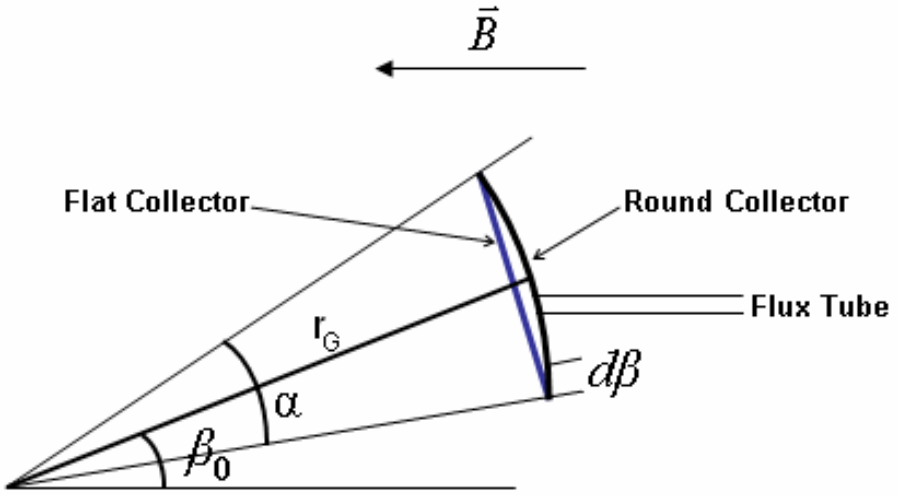

Figure 4.5: Comparison of the geometries of flat and round collectors.

The current ratio measured by round collectors and flat collectors agree very well for all but inclination angles near 0º and 180º with large perpendicular flow (see Figure 4.6 and Figure 4.7). For the Gundestrup probe on STOR-M, the collectors are centered at 0º, 45º, 90º, 135º, 180º, 225º, 270º and 315º and so it is unnecessary to use the round collector model to fit the data to theory since the deviation between 45º and 135º is small. The data from the collectors at 0 º and 180 º cannot be used with this model and are intended only for investigating the relationship between the current collected by these collectors and the flow velocities.

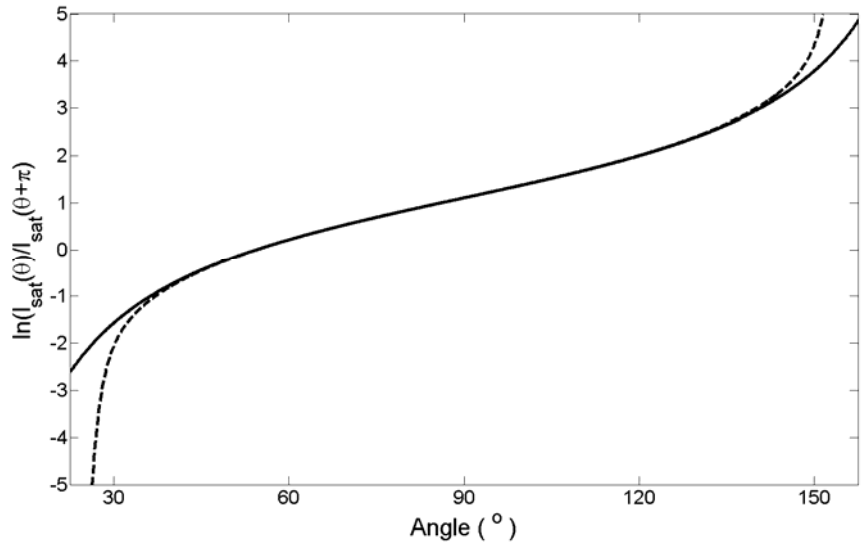

Figure 4.6: Natural logarithm of the ratio of upstream and downstream ion saturation current versus the inclination angle of the collectors for a flat collector (solid line) and a round collector (dashed line) for a flow with $M_{||\infty} = 0.5$ and $M_{\perp} = 0.7$.

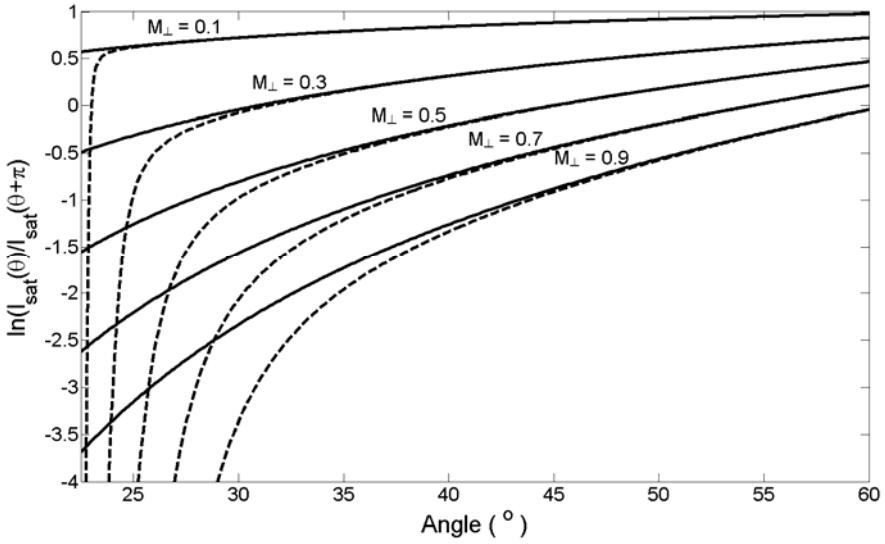

Figure 4.7: Natural logarithm of the ratio of upstream and downstream ion saturation current versus the inclination angle of the collectors for a flat collector (solid line) and a round collector (dashed line) for fixed $M_{||\infty} = 0.5$ and several values of $M_{\perp}$ (0.1, 0.3, 0.5, 0.7, 0.9).

Chapter 5

Experiment

5.1 Introduction

This chapter details the new probes that are installed in STOR-M for the purpose of this study. The Gundestrup probe is presented first, followed by the rake probe. Both the probe construction and electronic systems are described in detail.

5.2 Gundestrup Probe

5.2.1 Probe Mount

The Gundestrup probe mount on STOR-M is based around an LSM series linear shift mechanism built by UHV Design [102] (see Figure 5.1). The shifting mechanism is sealed inside of STOR-M with a stainless steel bellows. The probe mount allows 100 mm of travel and the position is adjusted with a manual handwheel. There is a 70 mm Conflat (CF) flange on each end of the bellows; One connected to a stiffer bellows, for connection to the STOR-M chamber and the other is sealed, with a 10 pin electrical feedthrough welded to the flange. The Gundestrup probe is mounted on an 86 mm port between toroidal field coils 10 and 11, so an adapter flange is used to connect the probe to the machine.

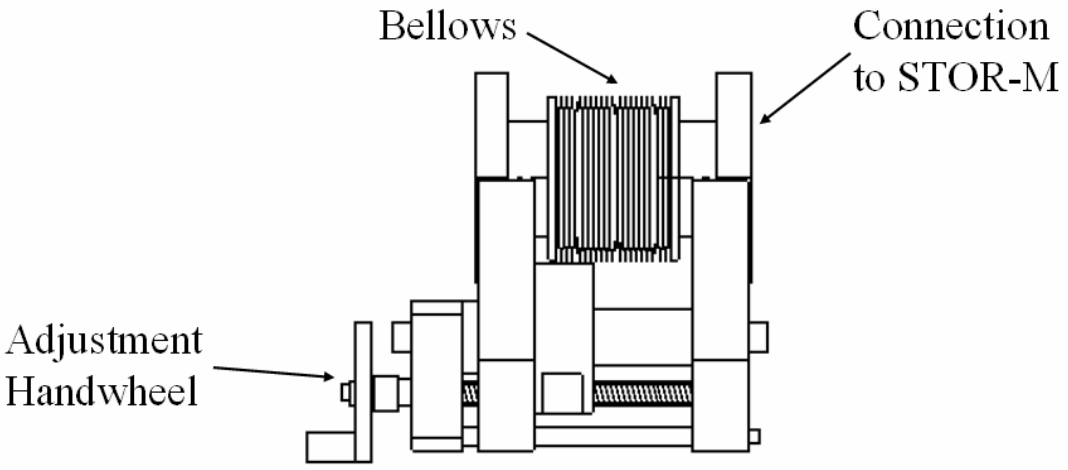

Figure 5.1: Schematic of the linear shift mechanism of the Gundestrup probe mount [102].

Since the linear shift mechanism is heavy and the 70 mm CF flange on the mount attached to a bellows, the assembly cannot be supported by the connection to the diagnostic port that it is connected to like the other electrostatic and magnetic probes on STOR-M. A 6 mm thick aluminum bracket was machined to support the probe assembly. This bracket is mounted to an upright support of the STOR-M structure (see Figure 5.2).

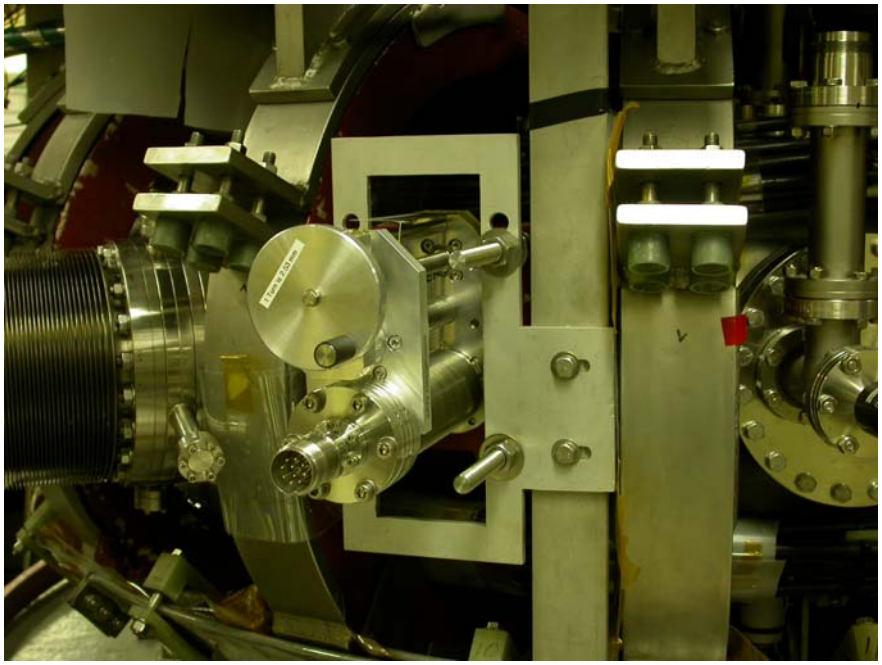

Figure 5.2: Photograph of the Gundestrup probe mount on STOR-M.

5.2.2 Probe Head

The Gundestrup probe head components were machined by Plasmionique Inc. and were assembled by technicians at INRS-EMT (Institut National de la Recherche Scientific – Énergie, Matériaux et Télécommunications) in Varennes, Quebec. The probe head has five main components: the insulating housing which forms the basic structure of the probe, the eight collectors for measuring the polar current distribution, the insulating cap, the Langmuir probe tip and its insulating sleeve. A schematic of the probe head is shown in Figure 5.3 and a photograph is shown in Figure 5.4.

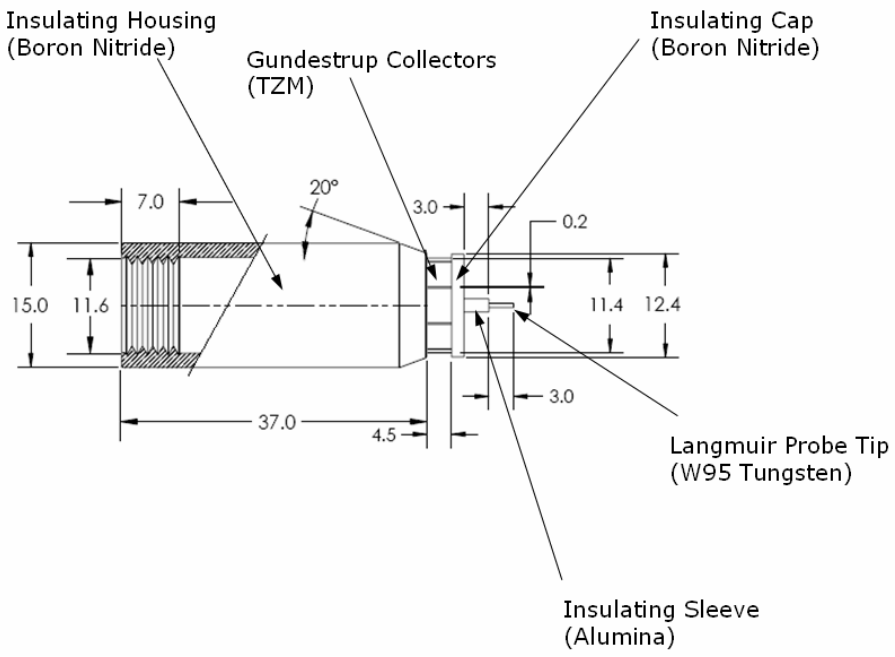

Figure 5.3: Partially cutaway schematic of the Gundestrup probe head. All dimensions are in millimeters.

The eight Gundestrup collectors form a cylinder with a radius of 11.4 mm and have an exposed length of 4.5 mm. Each collector spans approximately 44° around the circumference of the probe head; the centers of adjacent collectors are separated by 45° with a 0.2 mm gap between each collector. The collectors are made from the Molybdenum alloy TZM (Chemical Formula: Mo + 0.40-0.55% Ti + 0.06-.012% Zr + 0.01-0.04% C). This alloy has excellent high temperature properties, the melting point is 2623°C [103] and it is twice as strong as pure Molybdenum at temperatures above 1300°C [104], making it a suitable choice for use in the edge region of STOR-M.

The Langmuir probe tip is made of 0.5 mm diameter tungsten wire (W95), which has a melting point of 3422°C and offers good heat resistance [103]. The tip has a length of 3 mm and is radially separated from the collectors by 7.5 mm.

The insulating housing and cap are made from Boron Nitride, a high-temperature machinable ceramic. Boron Nitride has a high heat tolerance (temperature limit is 2500°C), making it resistant to the heat load presented by the plasma edge, is easily machinable, is an excellent electrical insulator (resistivity $\approx 10^{13}$ Ω·m) and does not outgas in ultra-high vacuum environments [105]. The insulating sleeve for the Langmuir

tip is made from alumina ceramic (AL_2O_3) which is also very good insulator (resistivity ≈ 10^{12} Ω·m), has a maximum operating temperature of approximately 1750°C [106] and is readily available as tubes suitable for holding tungsten wire.

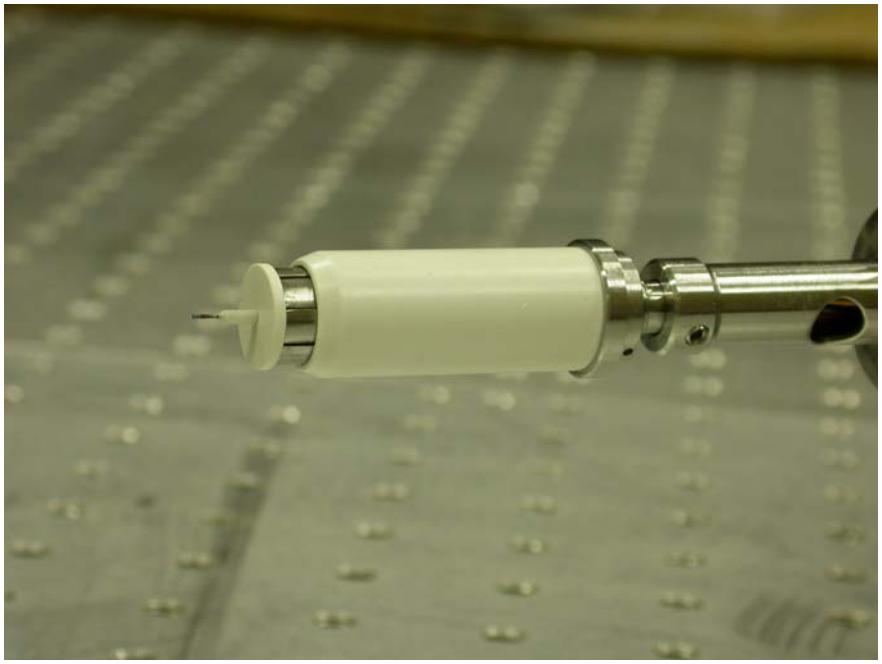

Figure 5.4: Photograph of the Gundestrup probe on STOR-M.

The alignment of the collectors on STOR-M is shown in Figure 5.5. This alignment is chosen as it provides 6 collectors to be used to analyse the plasma flow velocity and also provides data for the current collected by collectors that are inclined at 0° and 180° to the magnetic field. This data could be useful in analysing the physics of these collectors which are outside the range of the adopted model.

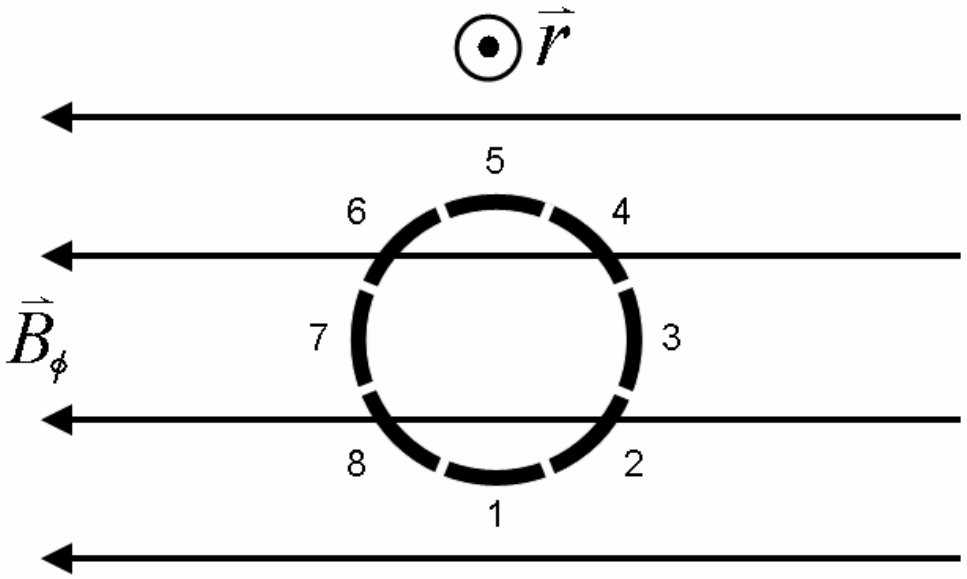

Figure 5.5: Orientation of the Gundestrup probe collectors on STOR-M relative to the toroidal magnetic field as viewed from the outside of the vacuum chamber.

5.2.3 Probe Biasing

In order to make measurements with the Gundestrup probe, the collectors and tip must have a potential bias applied to them. The collectors are biased with a Kepco BOP 200-1M bipolar power supply that has a DC voltage output range of ±200 V and a current range of ±1 A [107]. The tip is biased with a Kepco BOP 100-4M bipolar power supply has a DC voltage output range of ±100 V and a current range of ±4 A [107]. The power supply can either be set to supply a constant DC voltage, or be driven by another voltage source, such as a signal generator to provide an AC output. For the Gundestrup collectors, the Kepco BOP 200-1M is set to provide a constant -100V in order to collect the ion saturation current. In order to make measurements of the electron temperature, the voltage applied to the proud tip must be swept and so the Kepco BOP 100-4M is driven with a Data Royal Model F230 waveform/sweep generator [108]. When being driven with a signal generator, the Kepco BOP 100-4M has a gain of -5. The voltage on the proud tip is swept between -80 V and 20 V and so the input is driven with a saw-tooth wave with an amplitude of 10 V and a frequency of 200 Hz. The BOP 100-4M is able to provide the -30 V DC offset to the signal.

5.2.4 Data Acquisition

For measurements with the Gundestrup probe head, the current drawn by the collectors and tip are measured. For the collectors, the voltage does not matter, so long as it is sufficiently negative that the collectors collect the ion saturation current. For the tip, the I-V curve is needed to determine the electron temperature and density and so both the current and voltage are measured. This is accomplished with a series of components. The output from the Kepco amplifiers are sent to a resistance box ("boîtier de résistances"), which contains 16 channels [109]. Eight of these channels are used to measure the current collected by the Gundestrup collectors. The voltage across a resistor in series with the collector is measured and used to determine the current in the circuit. The value of the resistor can be selected between four values, 2 Ω, 1 Ω, 0.5 Ω and 0.3 Ω. Since the output should not exceed ±100 mV to avoid saturating the data acquisition system, the resistance can be selected to maximize the dynamic range of the system while also avoiding saturating any of the components. Of the eight other channels, only one is used to measure the voltage on the Langmuir tip and the current it draws from the plasma. This channel has the same selectable resistor as the other 8 channels (2 Ω, 1 Ω, 0.5 Ω and 0.3 Ω), across which the voltage drop is measured to determine the current in the circuit, as well as a 1000:1 voltage divider that is in parallel with the output to the probe that is used to monitor the voltage. The probe biasing circuits are shown in Figure 5.6 and Figure 5.7. The Langmuir tip is also used to measure the floating potential of the plasma. In this mode of operation, the voltage is read across a 1000:1 voltage divider consisting of a 100 kΩ and a 100 Ω resistor in series with the probe. The voltage is read across the 100 Ω resistor. This circuit is shown in Figure 5.8.

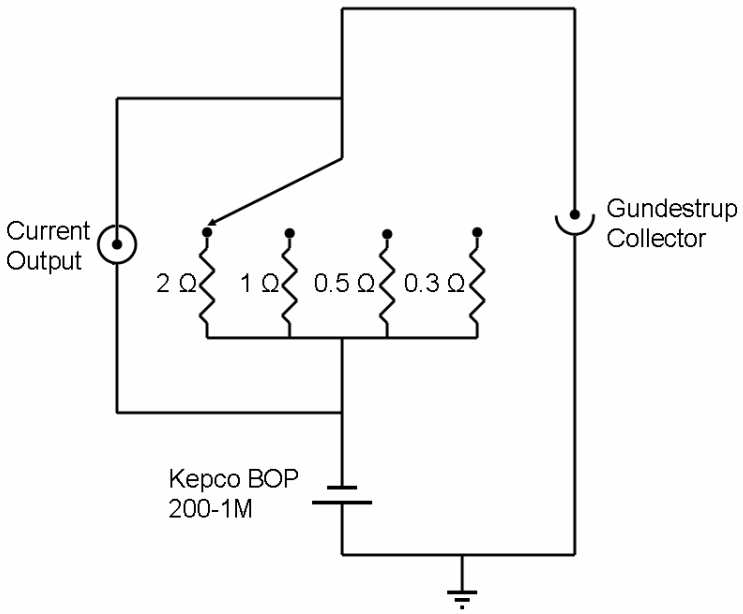

Figure 5.6: The circuit in the resistance box for measuring current drawn by the Gundestrup collectors. There are 8 identical circuits like this in the resistance box.

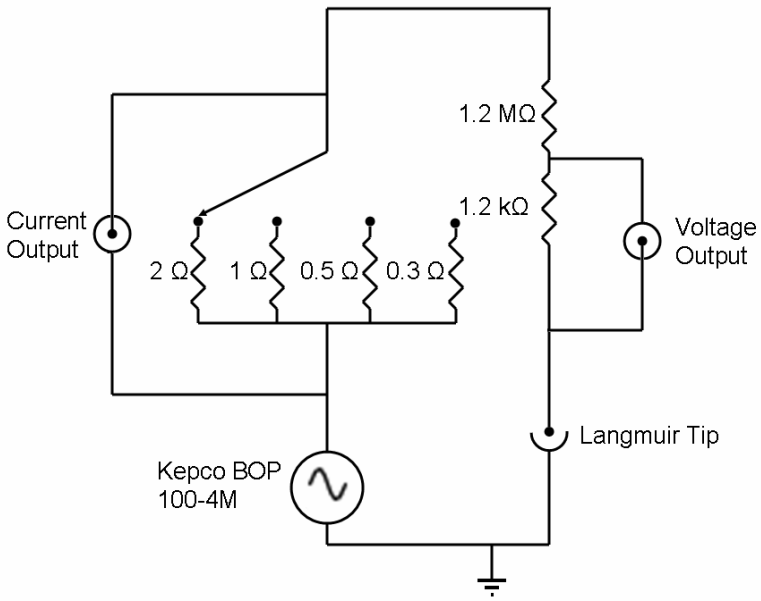

Figure 5.7: The circuit in the resistance box for measuring the current and voltage on the Langmuir tip.

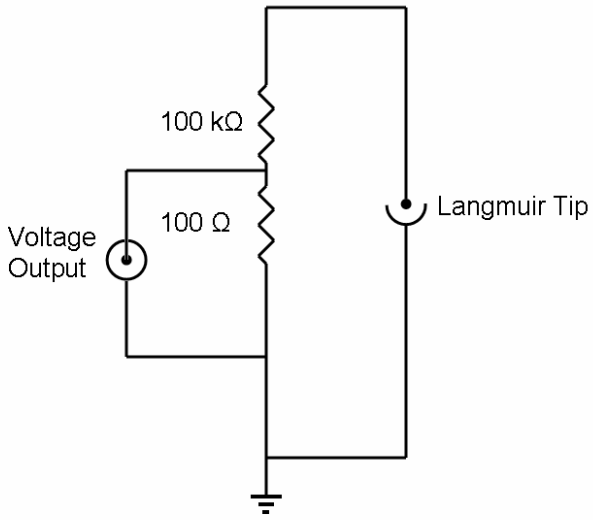

Figure 5.8: The circuit used for measuring the plasma floating potential with the Langmuir tip.

The outputs of the resistance box are sent to a set of 16 isolation amplifiers, which are necessary to measure the current without disturbing the biasing circuit. The isolation amplifiers used are Analog Devices 5B40 Signal Conditioning Modules which accept an input voltage of ±100 mV and have a maximum output voltage of ±5 V [110]. The isolation amplifiers are mounted to an Analog devices 5B01 backplane which has screw terminals to accept inputs and has two redundant 26 pin outputs [111]. The output from the isolation amplifiers is then sent to a 26 pin breakout box which connects each pin to a screw terminal allowing the output signals to be easily connected to coaxial cables.

The ten signals from the Gundestrup probe are sent across the room on 12 m of coaxial cable to a LeCroy CAMAC model 8212A fast data logger module. The 8212A is a 32 channel 12-bit ADC with full-scale input range of ±5 V [112]. While capable of simultaneous sampling of up to 40 kHz, this is reduced to 10 kHz when 9-16 channels are used. The 8212A is used in conjunction with a LeCroy CAMAC model 8800A memory module which can store 32 768 12-bit words [113]. This module allows for the storage of to 204.8 ms of data; since the discharge duration of STOR-M is typically 40 ms, this is sufficient to monitor the entire discharge. The data stored on the LeCroy 8800A is then

transferred to a Windows PC through a LeCroy Model 8901A CAMAC to General Purpose Interface Bus (GPIB) interface which allows transfers of up to 500 kB/s [114]. A block diagram of the data acquisition system is shown in Figure 5.9.

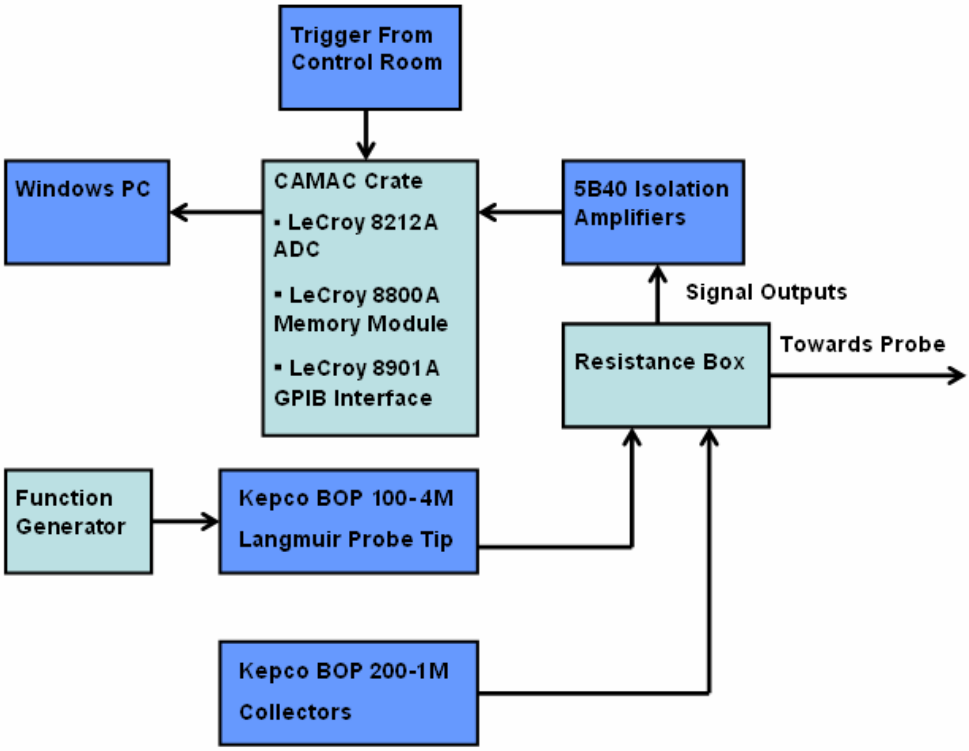

Figure 5.9: Block diagram of the data acquisition system for the Gundestrup probe.

The Windows PC reads the data from the CAMAC module through a DOS-based program called Catalyst. Catalyst is able to read and display data collected on various LeCroy Modules and saves it in binary format.

5.2.5 Modifications to the Probe Head

Following an initial set of experiments the proud tip on the Gundestrup probe was almost completely eroded and the boron nitride insulating cap was damaged. Once a probe becomes damaged it cannot be inserted into the plasma as the probe surface is quickly eroded by the plasma. This results in contamination of the plasma and leads to disruptions. Therefore the probe was removed for repair. The design was modified by removing the proud tip from the probe. This allows the Gundestrup probe collectors to

be inserted further into the plasma with a lower risk of damage to the probe. A schematic of the modified probe is shown in Figure 5.10.

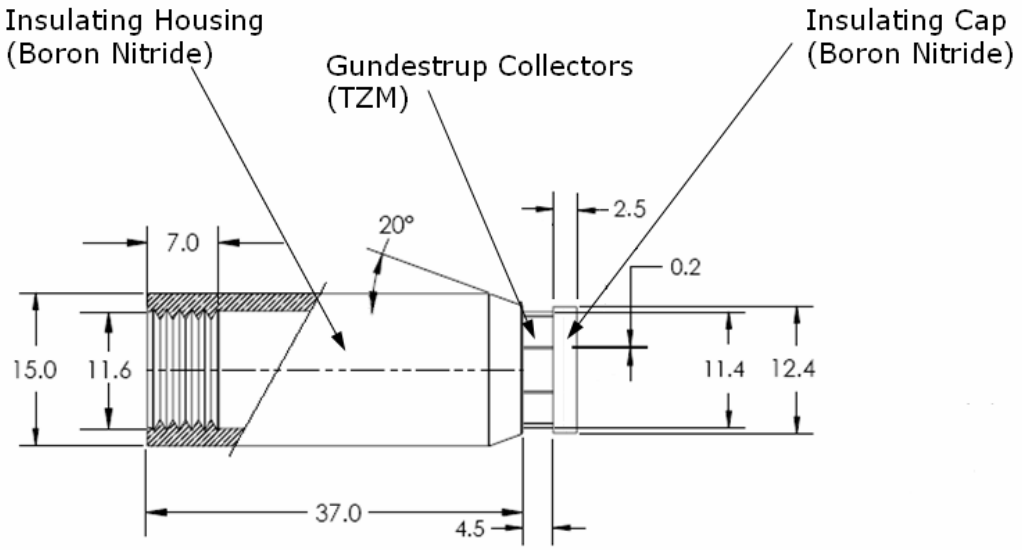

Figure 5.10: Schematic of the modified Gundestrup probe head.

5.3 Rake Probe

5.3.1 Probe Mount

The double rake probe mount is based around a Huntington® Mechanical Laboratories LR-2200-2 rotary/linear feedthrough. This UHV feedthrough allows 50 mm or linear motion and unlimited rotational motion [115]. The probe's electrical connections are made through a Varian 20-Pin instrumentation feedthrough. Both the rotary/linear feedthrough and the electrical feedthrough are mounted to an MDC Vacuum Products tee which connects to the STOR-M vacuum chamber on a 70 mm CF flange. The probe mount is show in Figure 5.11.

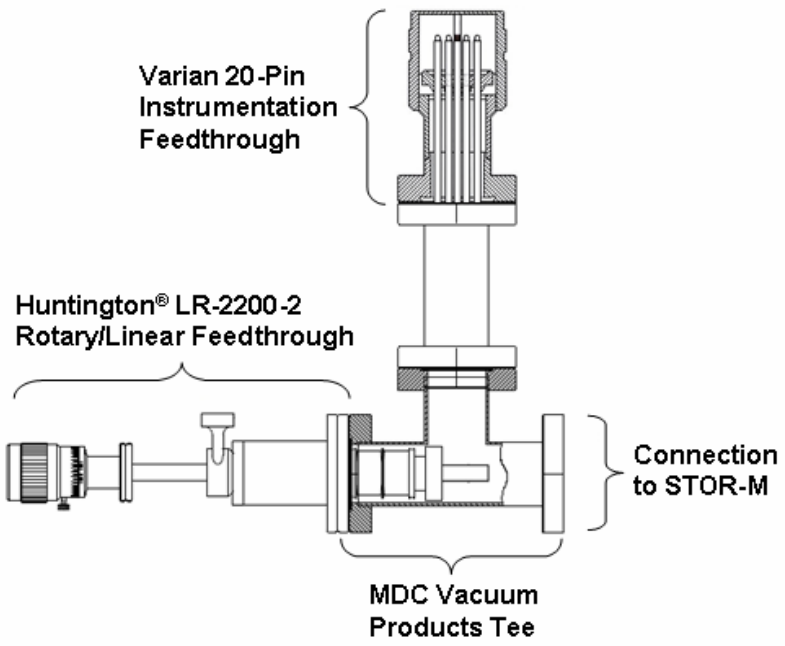

Figure 5.11: Schematic of the rake probe mount.

5.3.2 Probe Head

The rake probe head is made from AX05 grade Combat® boron nitride which is easily machinable and offers an operating temperature limit of more than 2000°C [116]. The rake probe head (shown schematically in Figure 5.12). has a diameter of 9.5 mm and a length of 29 mm. Sixteen 0.5 mm diameter holes are arranged in two rows along the length of the head. The rows are separated by 2.5 mm and along each row there is 2.5mm spacing between holes. The head is center bored from one end through to 2 mm from the opposite end to a diameter of 6.35 mm. This bore allows two rows of 0.100″ grid single-in-line (SIL) sockets to be aligned underneath the 16 holes. These sockets have 16 leads soldered to them in order to make the electrical connection to the probe tips. The sockets are held in place using Varian Torr Seal epoxy.

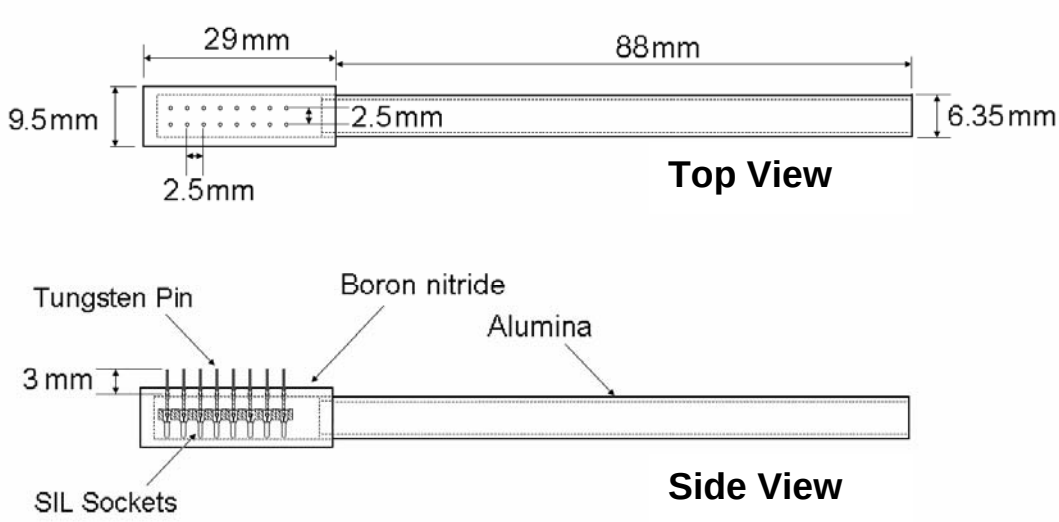

Figure 5.12: Schematic of the rake probe.

The probe tips are made of 8 mm long sections of 0.5 mm diameter tungsten wire. The wire is inserted into the sockets, which leaves a 3 mm exposed tip. These pins are pressure fit in the socket and can be removed and replaced if any are damaged by the plasma.

The rake probe head is attached to a 6.35 mm outer diameter (5 mm inner diameter), 93 mm long alumina rod. The leads from the sockets are fed through this rod and it is inserted 5 mm into the boron nitride probe head and secured with Torr Seal epoxy. This alumina rod is attached to a stainless steel cylinder with Torr Seal epoxy. This cylinder is attached to the probe mount with a machine screw. The probe mount allows the innermost pair of pins to be moved between minor radii of 150 mm and 100 mm.

5.3.3 Data Acquisition

The rake probe is used for measuring both the floating potential and ion saturation current on STOR-M. The two measurements require different electronics, both of which are described below.

For measurements of the floating potential it is important that there is no loading of the circuit to which the floating pin is connected. This means that the cable over which the probe is connected to the data acquisition system must be short, long cables will load the circuit too heavily and cause the probe to collect electron current. The probe mounting position on STOR-M would require long cable to connect to the data acquisition system, and so the probe output cannot be directly connected to the data acquisition system. Instead, the signals are brought to a 16-channel 50 Ω cable driver. These cable drivers are built around an LM6181 Current Feedback Amplifier, which has a 100 MHz bandwidth and can drive up to 100 pF loads without oscillating. The cable drive circuit used has unity gain and is shown in Figure 5.13.

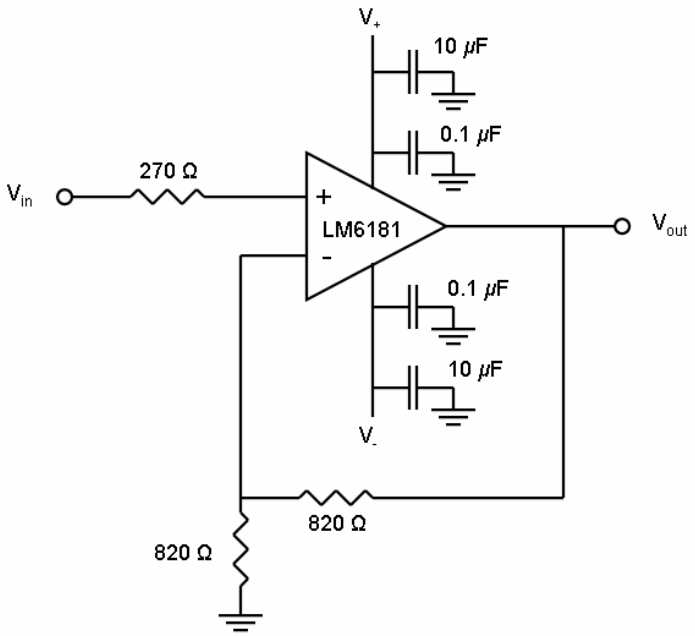

Figure 5.13: Cable driver circuit used to send the rake probe output signals to the data acquisition system.

For ion saturation current measurements, the probe tips must be negatively biased. This is done using a 100 V, 500 mA power supply. The power suppy biases the probe

tips to -75 V. A 47 Ω current sensing resistor is placed in series with the probe tip on the power supply side and the voltage drop across the resistor is measured. The wiring diagram is shown in .

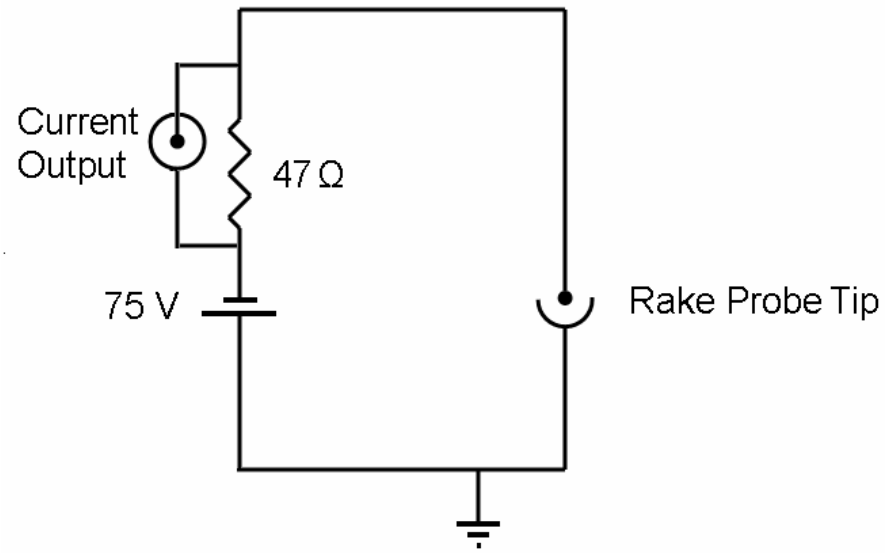

Figure 5.14: Schematic of the circuit used to measure the ion saturation current with the rake probe.

The outputs of the cable drivers and the current sensing resistors are sent to two National Instruments BNC-2110 terminal blocks. Each terminal block is connected to a National Instruments PCI-6133 on a 100-pin shielded cable. Each of these cards is capable of simultaneous sampling of 8 analog inputs at 2.5 megasamples per second (MS/s) with 14-bit resolution and has 16 MS of memory [117]. The two cards are synchronized, allowing the system to simultaneously sample all 16 channels. These DAQ cards are controlled with a Labview program which allows selection of channels, sampling rate and the number of data points to collect.

Chapter 6

Results and Discussion

6.1 Introduction

In this chapter the experimental results of the experiments on STOR-M are described. In STOR-M modification to the parallel and perpendicular flow velocity profiles are observed with both turbulent heating and electrode biasing.

The results are presented as follows. Section 6.2 describes the normal Ohmic discharge in STOR-M. In section 6.3, the results with reversal of the toroidal magnetic field are presented. The results obtained during H-mode induced by turbulent hearing are presented in section 6.4. In section 6.5 the results for discharges with electrode biasing are discussed. Comparative results from CASTOR tokamak during normal Ohmic discharges and during discharges with positive electrode biasing are discussed in section 6.6.

6.2 Normal Ohmic Discharges in STOR-M

The plasma discharge in STOR-M occurs in four phases, the initial gas breakdown, current ramp up, quasisteady state with flat current and the discharge termination. The initial gas breakdown begins with pre-ionization, performed with a hot filament and an rf field. The hot filament system is always switched on while the RF field is triggered 1 ms before the application of the toroidal electric field. This pre-ionization provides seed electrons to be accelerated by the toroidal electric field which then produce more free electrons through collisional ionization of neutral particles. A -100 V bias is applied to the transformer by the bias bank (450 V, 20 mF). This is done to maximize the flux available for driving plasma current. The initial toroidal electric field is supplied by the

fast Ohmic capacitor bank (450 V, 200 mF) which causes the initial breakdown and current ramp up. Current ramp up takes about 8 ms, shortly after which the fast Ohmic capacitor bank is exhausted. The quasisteady state current is then maintained by the slow Ohmic capacitor bank (100 V, 10 F). During the discharge several parameters must be actively controlled. The plasma position is controlled by an active feedback system. The plasma density is maintained by a preprogrammed gas puffing circuit which controls a PV-10 piezoelectric valve, puffing additional hydrogen into the vacuum chamber. The discharge is terminated by a strong gas puff after about 40 ms to prevent excess runaway electrons which can damage the vacuum vessel and internal probes.

The quality of the discharge is very sensitive to impurities inside of the chamber. After opening the chamber to replace probes or other components it is necessary to condition the chamber wall which will have absorbed a significant amount of impurities when it is exposed to atmosphere. A DC glow discharge cleaning is an efficient way to clean the chamber wall. A stainless steel electrode (anode) is inserted into the chamber and the chamber wall serves as the cathode. A power supply (2000 V, 1.5 A) and capacitor bank (900 V, 1.25 mF) are used to apply a 450 V DC voltage to the anode which causes a weakly ionized plasma to form in the chamber. This arrangement results in the chamber wall being bombarded by ions which removes impurities from the wall. The impurities are then pumped out of the chamber. One hour of glow discharge cleaning followed by 24 hours of pumping followed by a few hundred conditioning discharges is generally sufficient to attain plasma performance which is suitable for experimentation.

In this experiment the sign convention under the right hand (r,ϕ,θ) coordinate system is as follows: the toroidal field B_ϕ is negative (clockwise when viewed from above), I_p is positive, the poloidal field B_θ is negative (downward at the outboard midplane), the electron diamagnetic drift direction ω_{*e} is positive and the ion diamagnetic drift direction ω_{*i} is negative. This configuration is shown in Figure 6.1.

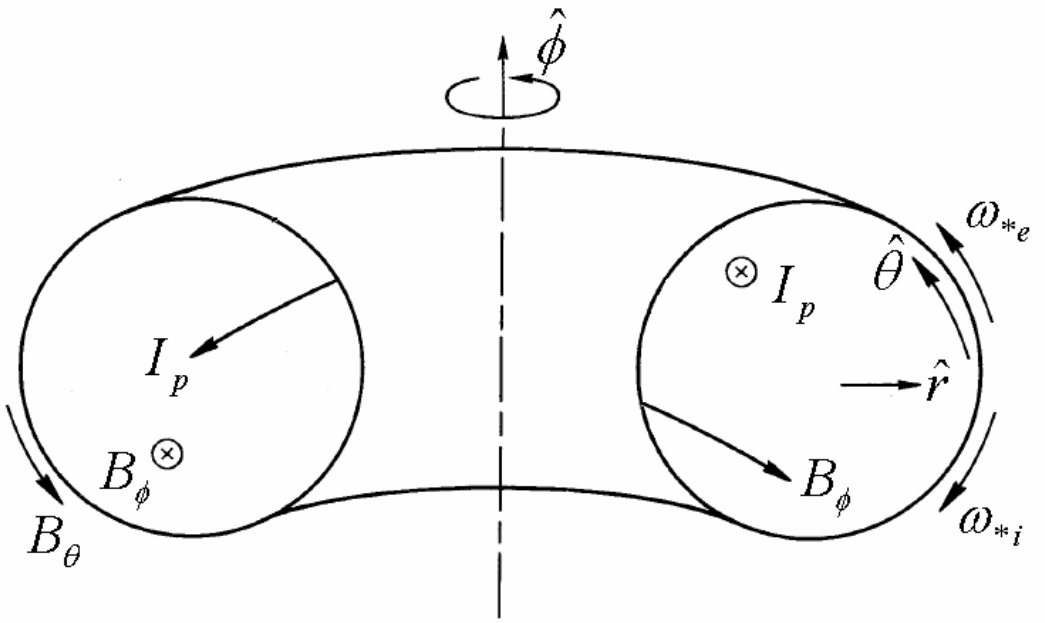

Figure 6.1: Drawing showing the orientation of various parameters for the normal configuration of STOR-M (adapted from Chen [11].)

The typical plasma discharge parameters (plasma current I_p, loop voltage V_l, line averaged electron density $\overline{n}_e$, horizontal displacement ΔH, H_α emission at the plasma edge, gas puffing voltage and the toroidal magnetic field B_ϕ) are shown in Figure 6.2.

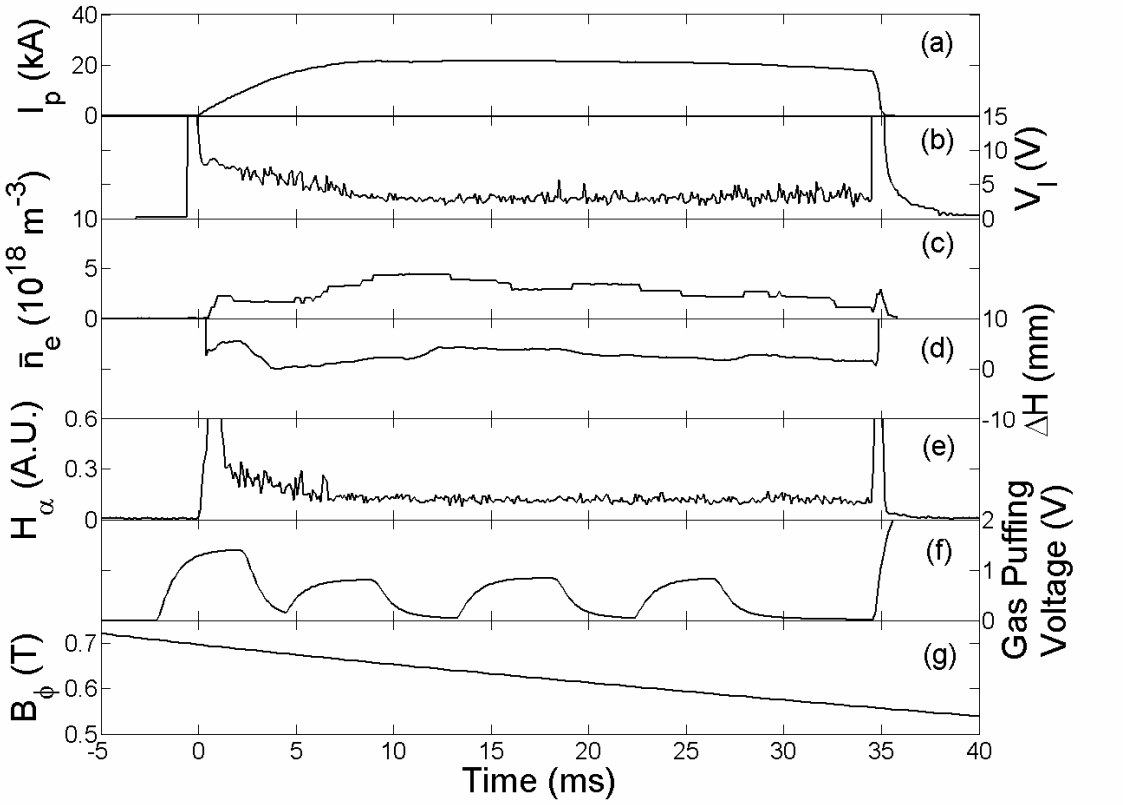

Figure 6.2: Waveforms of a typical Ohmic discharge. (a) Plasma Current. (b) Loop voltage. (c) Line averaged density. (d) Horizontal displacement. (e) H_α emission. (f) Gas puffing voltage. (g) Toroidal magnetic field.

The average electron temperature T_e can be estimated from the neoclassical resistivity and the confinement time τ_E can then be calculated from the ratio of the stored energy in the plasma to the input power. The plasma resistivity $\eta_{||}$, average electron temperature T_e and energy confinement time τ_E for an Ohmic discharge are shown in Figure 6.3. During the quasisteady state of the discharge, the plasma resistivity $\eta_{||}$ is about 2.5×10^{-6} Ω·m, the average electron temperature T_e is around 210 eV and the energy confinement time is peaks at around 1 ms and decreases through the discharge due to the decrease in plasma density.

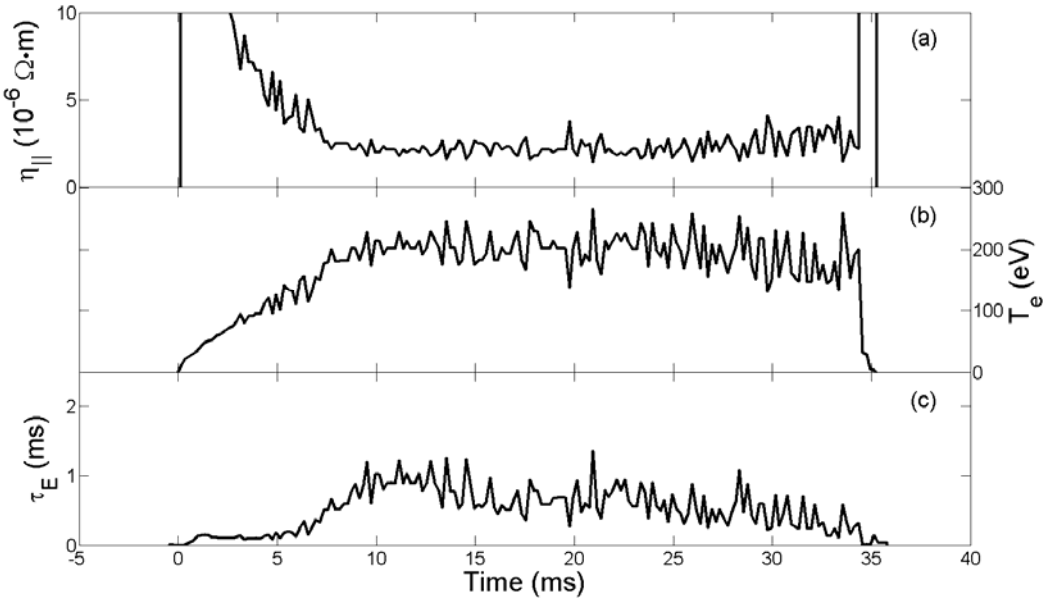

Figure 6.3: Waveforms of (a) parallel plasma resistivity, (b) average electron temperature, and (c) energy confinement time during an Ohmic discharge.

The proud tip on the Gundestrup probe is swept between -80 V and 20 V in order to measure the I-V characteristic curve for the plasma. The probe was moved between r = 135 mm and r = 100 mm over a number of discharges in order to obtain the radial profile of the electron temperature T_e (see Figure 6.4). From the electron temperature T_e, the ion sound speed c_s from the plasma can be found and used with the measured Mach numbers (Figure 6.7) in order to determine the absolute velocity of the parallel and perpendicular flow (Figure 6.8).

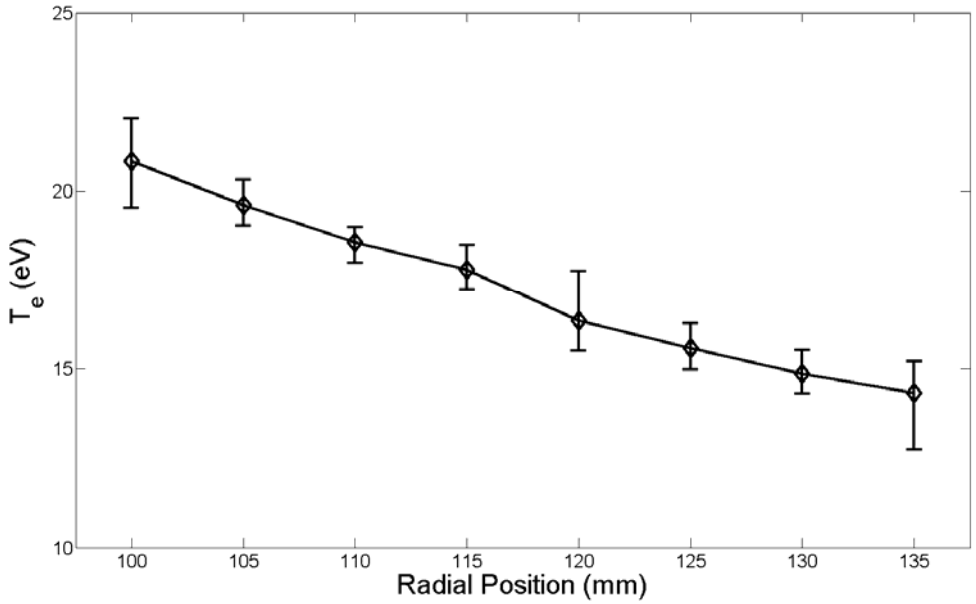

Figure 6.4: Radial profile of the electron temperature measured in the plasma edge.

The parallel and perpendicular plasma flow Mach number is measured using the Gundestrup probe. The raw signals collected by the Gundestrup probe at $r = 115$ mm are shown in Figure 6.5. The polar plot of the collected ion saturation current over a 1 ms period during the quasisteady state of the discharge is shown in Figure 6.6. It is important to note the large asymmetry in the current collected by the collectors at 90° and 270° versus the rather small asymmetry between the collectors at 0° and 180°. Qualitatively, this indicates a large parallel flow velocity and a negligible perpendicular flow velocity. This is quantitatively seen in the analyzed data below.

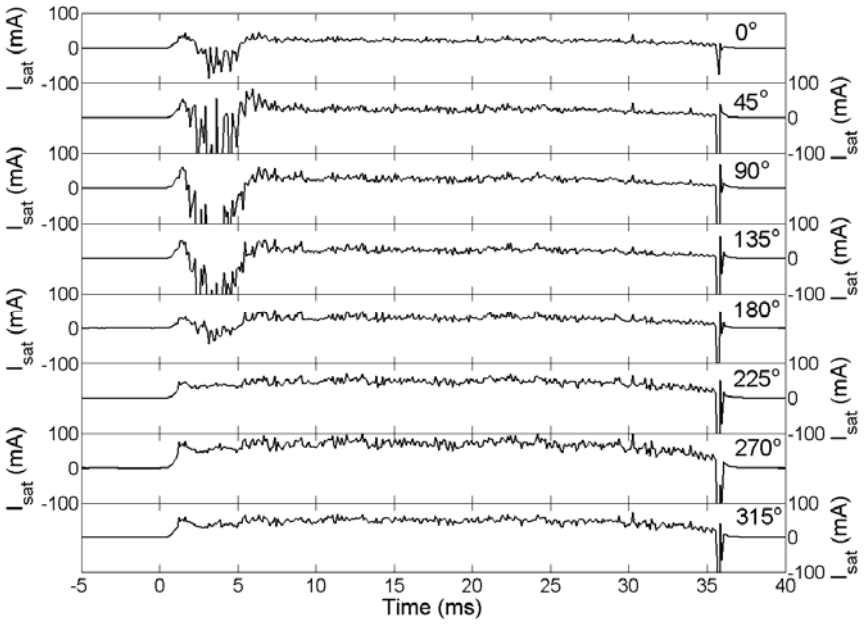

Figure 6.5: Waveforms of the ion saturation current collected by the Gundestrup probe. The labeled angles indicate the inclination of each collector to the magnetic field. These data are taken at r = 115 mm.

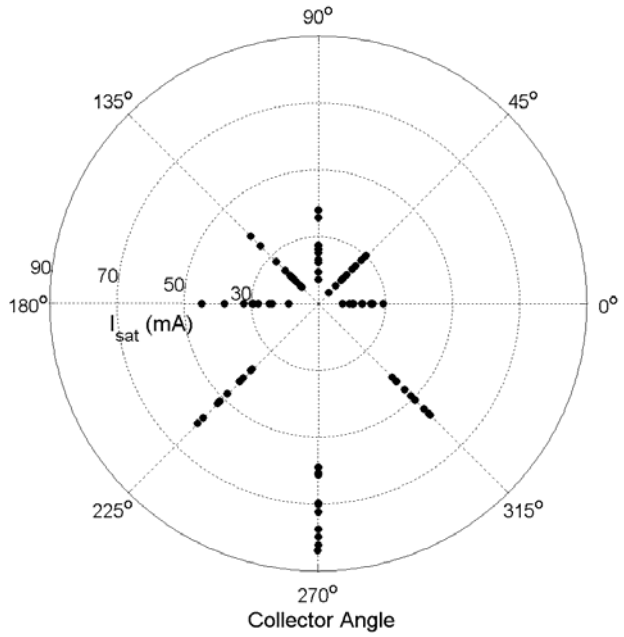

Figure 6.6: Polar diagram of the ion saturation current collected by the Gundestrup probe for 10 time segments between t = 20 and 21 ms during the flat top of an Ohmic discharge at r = 115 mm.

The Gundestrup probe was moved between r = 135 mm and r = 100 mm at 5 mm intervals over a series of discharges. The parallel flow Mach number $M_{||}$ (Figure 6.7a) takes a nearly constant value near 0.35 at all radial locations. The perpendicular plasma flow Mach number $M_{\perp}$ (Figure 6.7b) is essentially 0 at all radial locations during the Ohmic discharge.

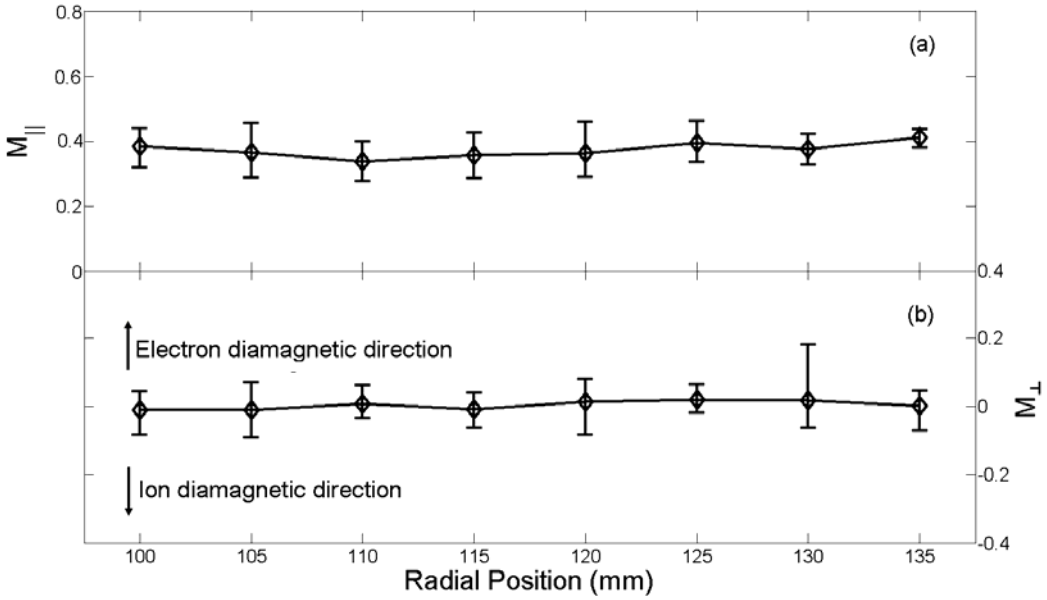

Figure 6.7: Radial profile of (a) the parallel flow Mach number and (b) the perpendicular flow Mach number during an Ohmic discharge.

The absolute velocity profiles of the flows (Figure 6.8) show that there is no shear in the flow. It is therefore unlikely that the plasma flow velocity plays any role in confinement during Ohmic discharges on STOR-M.

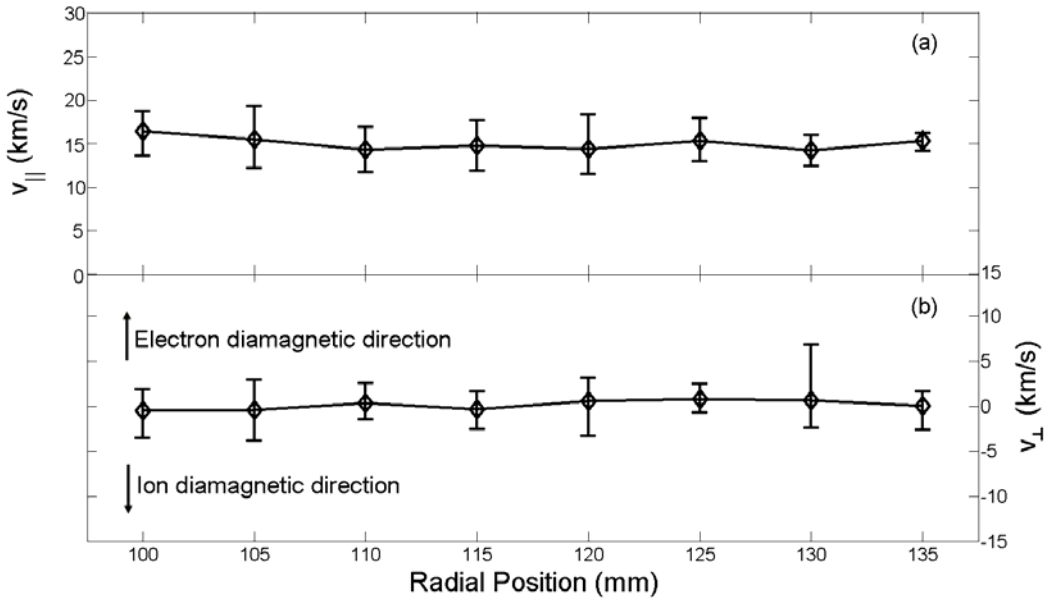

Figure 6.8: Radial profile of (a) the parallel flow velocity and (b) the perpendicular flow velocity during an Ohmic discharge.

6.3 Toroidal Magnetic Field Reversal

In order to investigate the dependence of the flow direction on the orientation of the toroidal magnetic field and plasma current (parallel vs antiparallel) the direction of the toroidal magnetic field is reversed. This is accomplished by switching the connection of the TF coils to the capacitor bank. Additionally, the direction of the horizontal stray field compensation is reversed by reversing the polarity of the compensation circuit in the control room. In this configuration the current and magnetic field are in the same direction. In this experiment the sign convention under the right hand (r, ϕ, θ) coordinate system is as follows: the toroidal field B_ϕ is negative (counter-clockwise when viewed from above), I_p is negative, the poloidal field B_θ is negative (downward at the outboard midplane), the electron diamagnetic drift direction ω_{*e} is negative and the ion diamagnetic drift direction ω_{*i} is positive. This configuration is shown in Figure 6.9.

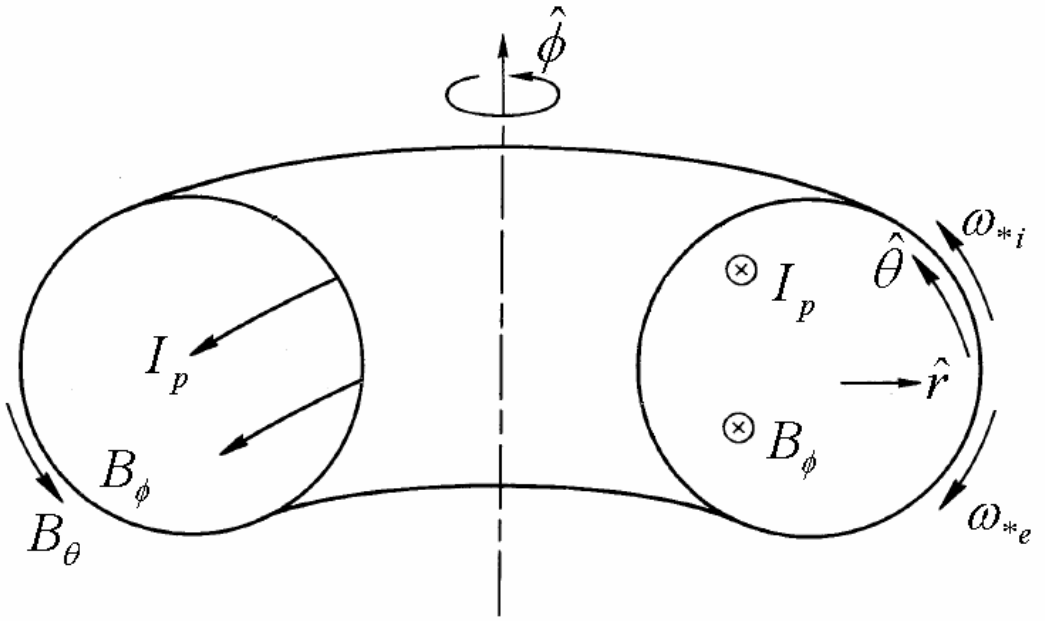

Figure 6.9: Drawing showing the orientation of various parameters for the reversed magnetic field configuration of STOR-M (adapted from Chen [11]).

The typical plasma discharge parameters (plasma current I_p, loop voltage V_l, line averaged electron density $\overline{n}_e$, horizontal displacement ΔH and H_α emission at the plasma edge) are shown in Figure 6.10. The only significant difference in the discharge parameters with the reversal of B_ϕ is that the discharge duration is typically shorter. For the normal configuration the discharge duration is typically 35 ms whereas with the reversed B_ϕ the discharge duration is typically 27 ms. This is likely due to slight differences in the magnetic geometry that results in the plasma position being more difficult to control.

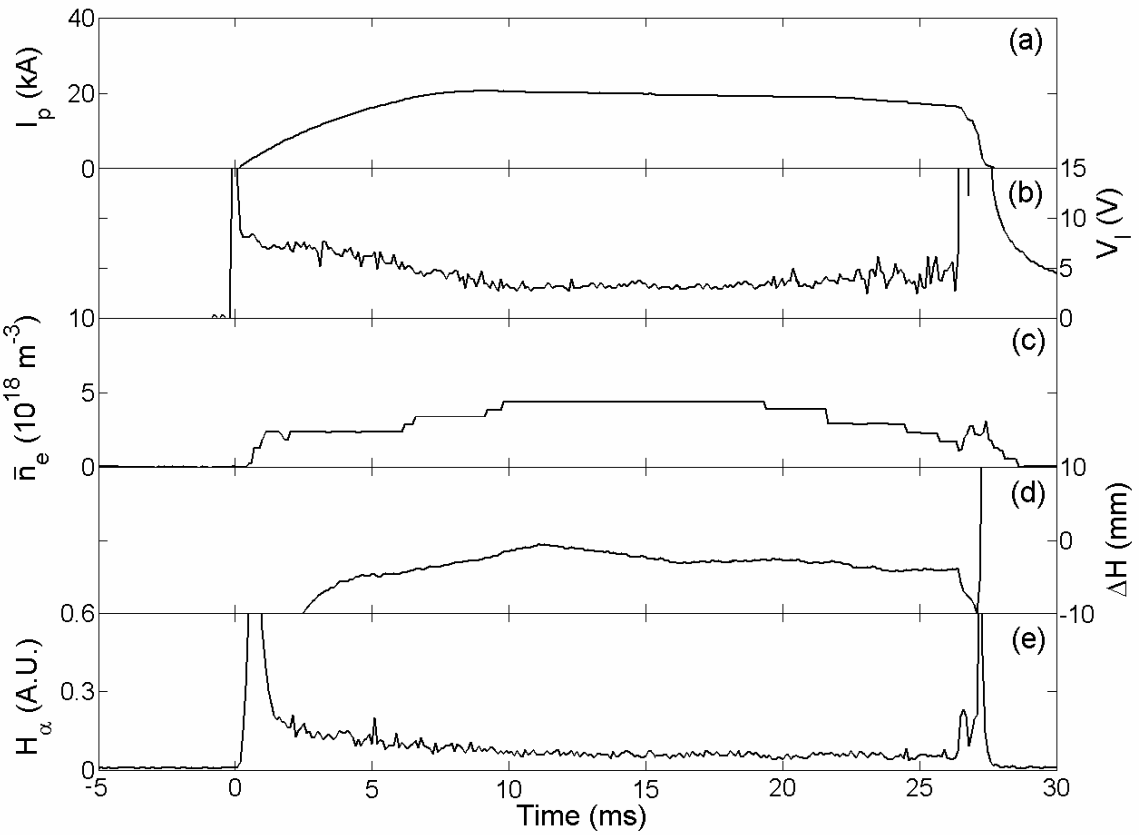

Figure 6.10: Waveforms of a typical discharge with reversed toroidal magnetic field. (a) Plasma Current. (b) Loop voltage. (c) Line averaged density. (d) Horizontal displacement. (e) H_α emission.

The plasma flow Mach numbers for the parallel and perpendicular flow are shown in Figure 6.11 and the absolute velocity are shown in Figure 6.12. The parallel flow velocity is of the same magnitude and direction as during the normal configuration. This indicates that the parallel flow direction is independent of the direction of B_ϕ. The perpendicular flow velocity profile shows a slightly positive value of approximately 2.5 km/s (electron diamagnetic drift direction) compared with the observation of no perpendicular flow during the normal configuration. However, the two measured perpendicular velocity profiles agree to within their experimental uncertainties.

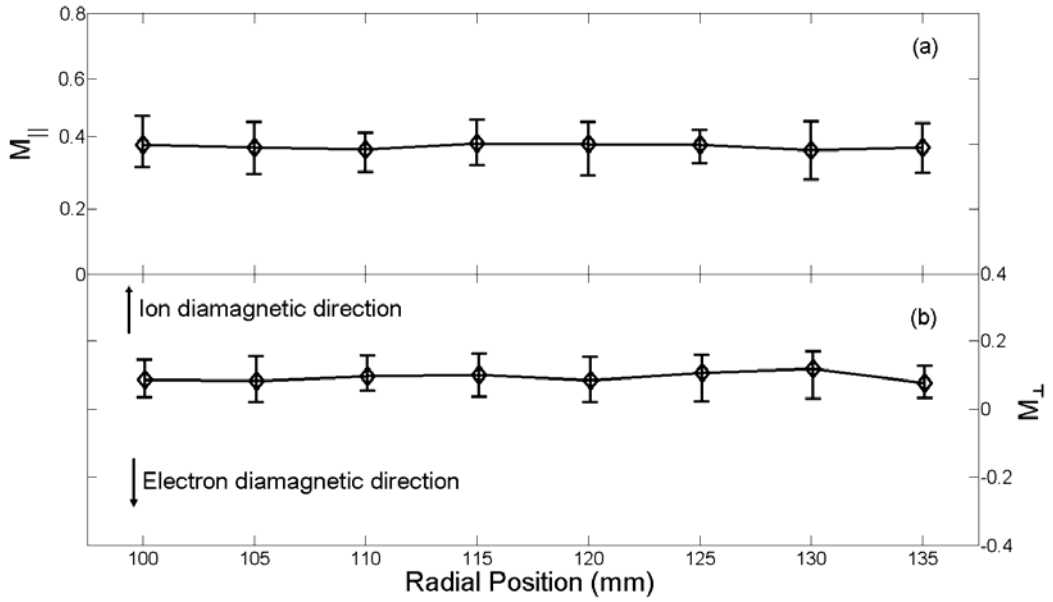

Figure 6.11: Radial profile of (a) the parallel flow Mach number and (b) the perpendicular flow Mach number during an Ohmic discharge with the toroidal magnetic field reversed.

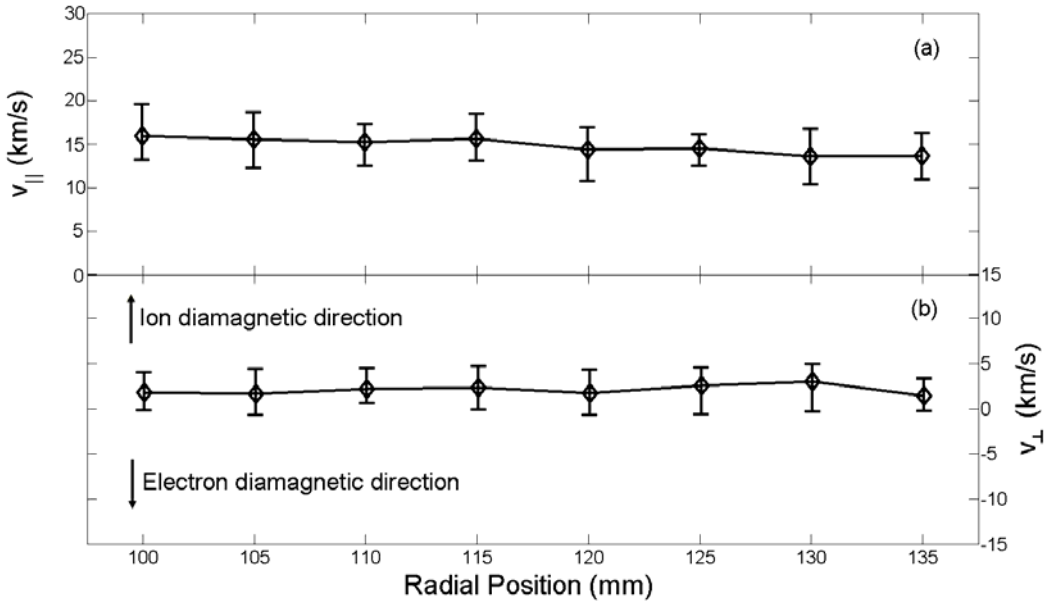

Figure 6.12: Radial profile of (a) the parallel flow velocity and (b) the perpendicular flow velocity during an Ohmic discharge with the toroidal magnetic field reversed.

It is observed that the orientation of B_ϕ has no effect on the parallel flow velocity and at most a slight effect on the perpendicular flow velocity. This supports the idea that the parallel flow direction is determined by the plasma current direction.

6.4 Improved Ohmic Confinement Induced by Turbulent Heating

Turbulent heating is a process through which a nearly collisionless plasma can be heated through an enhanced plasma resistivity caused by the application of a short, intense current pulse. The current pulse lasts around 100 μs and is much shorter than the anomalous magnetic diffusion time ($\tau_R = \mu_0 a^2/\eta$) of about 1 ms [30]. The current is deposited to a skin depth which is of the order of the ion skin depth which is 5 cm in STOR-M [118]. The edge region of the tokamak plasma is preferentially heated. The TH pulse can also excite various short wavelength electrostatic instabilities, including the ion acoustic instability.

A TH pulse was applied to the plasma during the plateau phase of the Ohmic discharge approximately 14.5 ms after the initiation of the discharge. The orientation of the toroidal magnetic field and plasma current are as shown in Figure 6.1. For this experiment the TH capacitor bank was charged to 650 V which resulted in a TH current of 12 kA superimposed on the 22 kA Ohmic current. This regime was chosen as it produced consistent results; larger TH currents resulted in occasional disruptions while smaller currents did not consistently produce observable H-modes. The typical discharge parameters (plasma current I_p, loop voltage V_l, line averaged electron density $\overline{n}_e$, horizontal displacement ΔH, and H_α emission) for the TH experiment are shown in Figure 6.13.

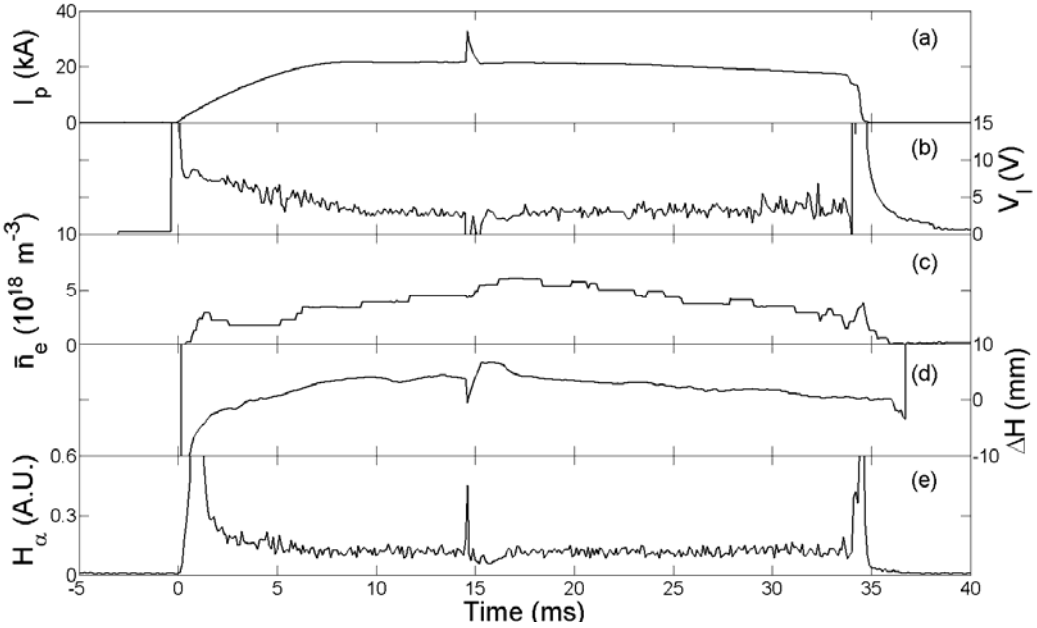

Figure 6.13: Waveforms of a typical discharge with a TH pulse applied at 14 ms. (a) Plasma Current. (b) Loop voltage. (c) Line averaged density. (d) Horizontal displacement. (e) H_α emission.

It can be seen that following the application of the TH pulse there is a decrease in the loop voltage caused by a decrease in the plasma resistivity. Concurrently there is an increase in the line averaged electron density from 4.4×10^{18} m^{-3} immediately before the TH pulse to 6.0×10^{18} m^{-3} after the TH pulse. The density increase lasts for approximately 3 ms and is consistent with an improvement in particle confinement. A decrease in H_α emission for approximately 2 ms also occurs following the TH pulse which is consistent with a reduction in the energy transport out of the plasma edge. This leads to a reduction in the ionization and recombination of hydrogen in the plasma edge. These observations are consistent with H-mode behaviour.

The plasma resistivity $\eta_{||}$, electron temperature T_e and energy confinement time τ_E are shown in Figure 6.14. It is observed that following the application of the TH pulse there is a decrease in the plasma resistivity $\eta_{||}$ from approximately 2.2×10^{-6} Ω·m to 1.5×10^{-6} Ω·m. Also, there is an increase in the electron temperature T_e from 210 eV before the TH pulse to 260 eV following the TH pulse. The energy confinement time τ_E

increases from the Ohmic value of about 1 ms to 2.4 ms after the TH pulse which corresponds to an improvement value *H* of 2.4.

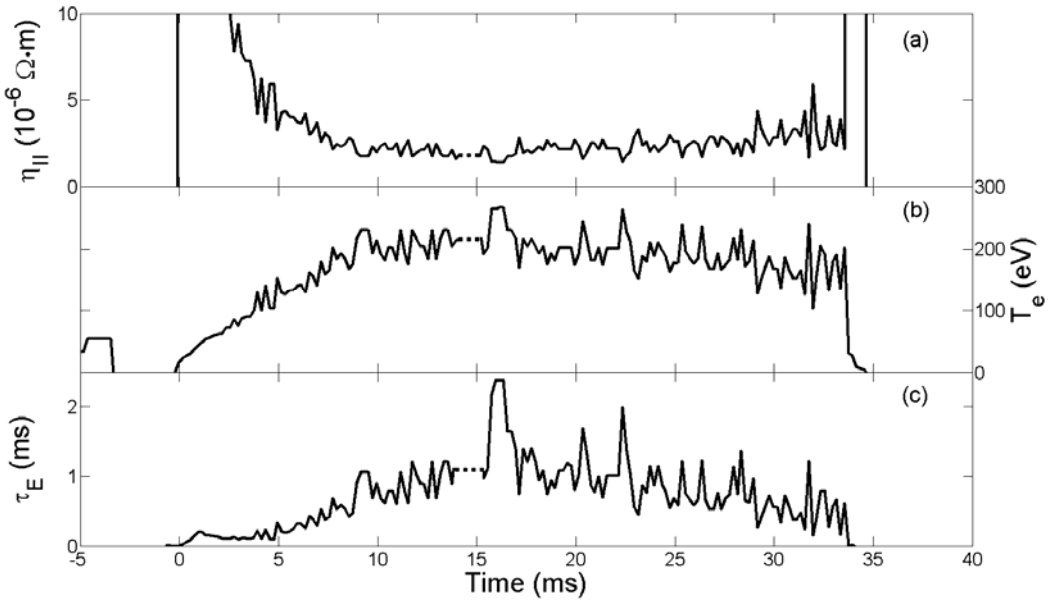

Figure 6.14: Waveforms of (a) parallel plasma resistivity, (b) average electron temperature, and (c) energy confinement time during a discharge with a TH pulse applied at 14 ms. The dashed segments of the lines indicate the time over which the data is not reliable due the effect of the TH pulse on the loop voltage (see Figure 6.13).

Figure 6.15 shows the m = 2 Mirnov coil signal ($\dot{\tilde{B}}_\theta$) and the fluctuating components of the floating potential ($\tilde{V}_f$) and ion saturation current ($\tilde{I}_{sat}$) both measured with the rake probe at r = 110 mm. A strong suppression of the m = 2 mode is observed following the TH pulse. $\tilde{V}_f$ and $\tilde{I}_{sat}$ are similarly suppressed following the TH pulse.

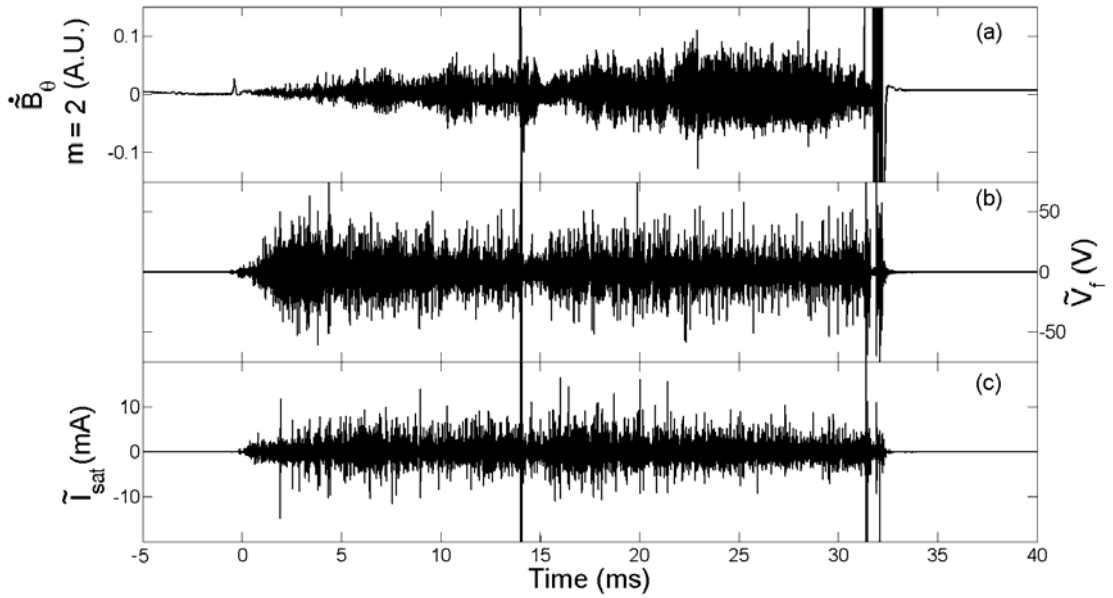

Figure 6.15: Waveforms of (a) m = 2 Mirnov coil signal and fluctuating components of the (a) floating potential and (b) ion saturation current for a discharge with a TH pulse at t = 14 ms.

The edge electron density profile is shown in Figure 6.16. One row of the rake probe (8 pins) is biased to -75 V to collect the ion saturation current from which the electron density can be deduced. It is evident that there is an increase in the density gradient following the TH pulse with the density at r = 110 mm increasing from 5.7 × 10^{17} m^{-3} during the Ohmic phase of the discharge to a maximum of 12.4 × 10^{17} m^{-3} 1.8 ms after the TH pulse representing a 2.2 fold increase in the density. Outside of r = 130 mm in the SOL the density decreases following the TH pulse. This indicates the existence of an edge transport barrier (ETB) just inside of the limiter ($r < a$). At 1.5 ms after the TH pulse the density profile begins to fall back to the profile it held during the Ohmic phase of the discharge. The edge density profile begins to return back to the Ohmic profile about 1 ms before the line averaged density begins to return to normal. This indicates that the core density remains elevated for a longer period of time than does the edge density. This is supported by previous observations in STOR-M [30].

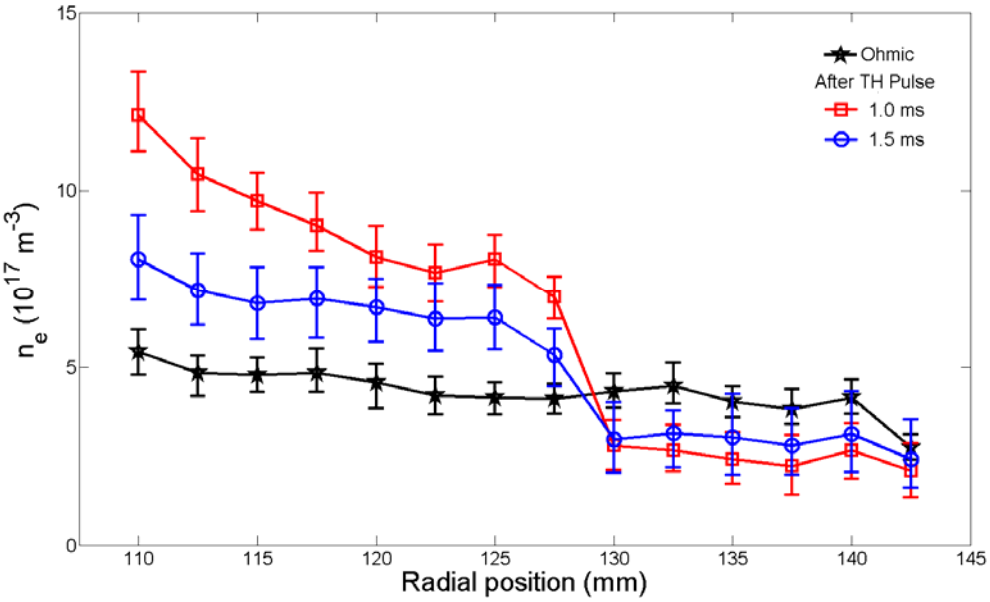

Figure 6.16: Radial profile of the edge electron density during the Ohmic phase of the discharge (black line), 1.0 ms after the TH pulse (red line) and 1.5 ms after the TH pulse (blue line).

The second row of the rake probe is allowed to float in the plasma to measure the floating potential. The radial profile of the floating potential during the Ohmic discharge and at several times following the application of the TH pulse is shown in Figure 6.17. It is observed that following the TH pulse the plasma adopts a more negative floating potential at all positions inside of the plasma edge (r = 120 mm) while outside of the edge the floating potential becomes slightly positive.

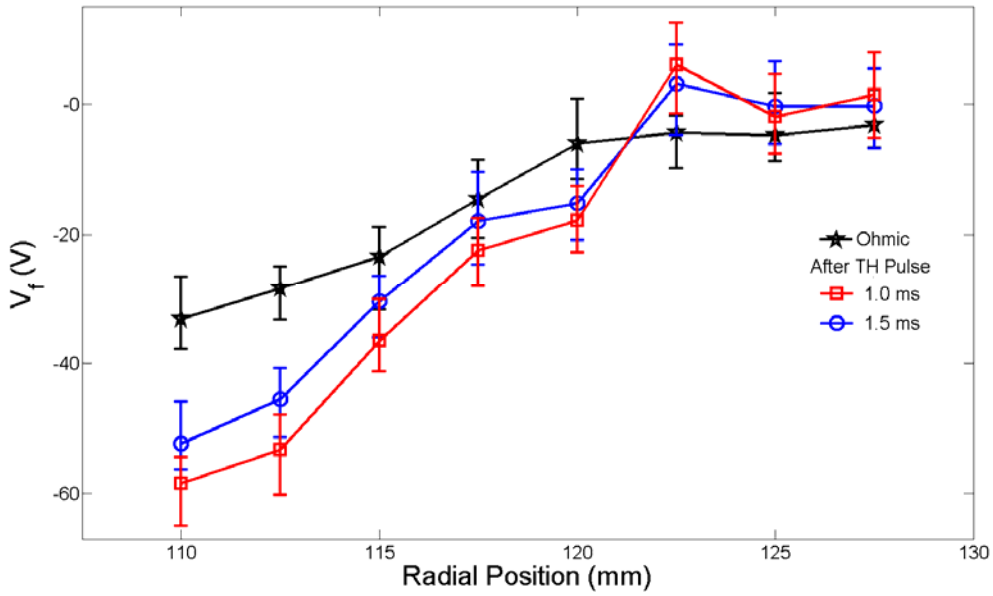

Figure 6.17: Radial profile of the floating potential during the Ohmic phase of the discharge (black line), 1.0 ms after the TH pulse (red line) and 1.5 ms after the TH pulse (blue line).

The plasma potential during the Ohmic phase of the discharge and at 1.5 ms after the TH pulse are shown in Figure 6.18a. After the TH pulse the plasma potential increases from about 50 V to 65 V outside of r = 117.5 mm and decreases from 45 V to 35 V inside of r = 112.5 mm. The result is that there is a substantial increase in the gradient of the plasma potential between r = 112.5 mm and r = 117.5 mm. Since the radial electric field can be expressed as $E_r = -\partial V_p / \partial r$ it follows that in this region the radial electric field becomes more negative, as is shown in Figure 6.18b. As will be shown below, the E_r profile qualitatively agrees with the perpendicular flow velocity profile.

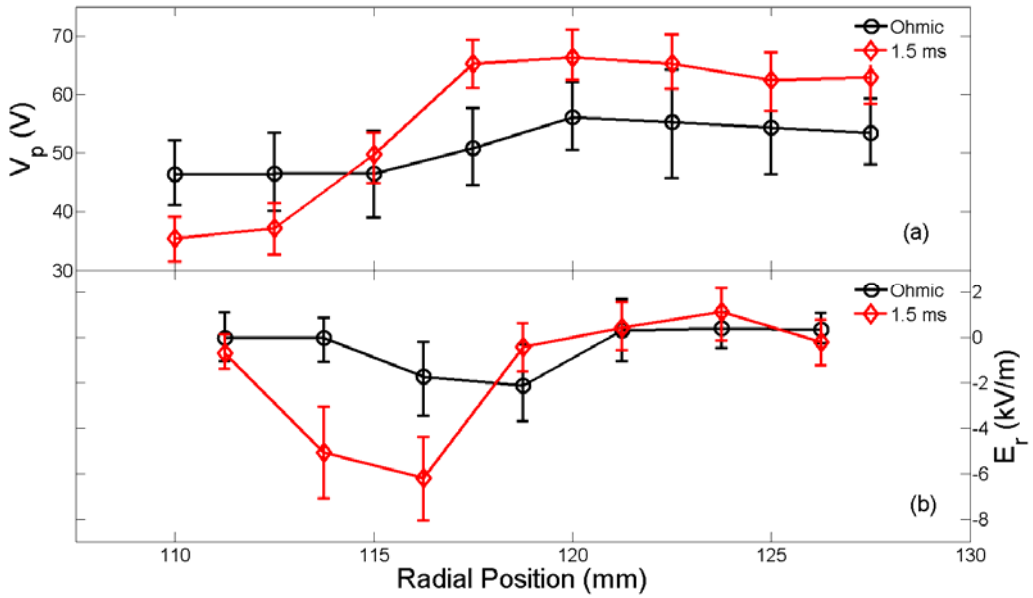

Figure 6.18: Radial profile of the (a) plasma potential and (b) radial electric field during the Ohmic phase of the discharge (black line) and 1.5 ms after the TH pulse (red line).

The evolution of the radial profile of the perpendicular flow Mach number is shown in Figure 6.19. The flow is initially accelerated in the electron diamagnetic drift direction at all radial locations from r = 105 mm to r = 125 mm. At r = 100 mm and between r = 130 mm and r = 135 mm the flow is mostly unaffected by the TH pulse. By 1.5 ms after the TH pulse the flow assumes a profile with a strong velocity shear between r = 110 mm and r = 125 mm with the flow being in opposite directions on either side of 118 mm. After 1.5 ms the flow begins to return to the profile it held during the Ohmic phase of the discharge. Using the profile of the electron temperature inferred from swept measurements with the proud tip of the Gundestrup probe (Figure 6.4) the flow Mach numbers are expressed as absolute velocities in Figure 6.20. It is observed that the magnitude of the perpendicular flow velocity becomes as large as 25 km/s in the electron diamagnetic drift direction following the TH pulse.

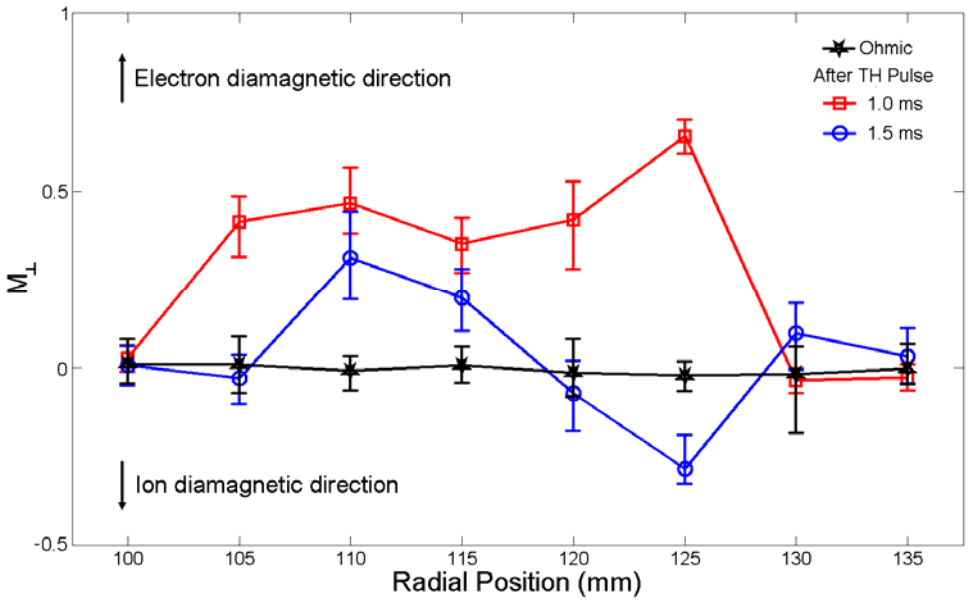

Figure 6.19: Radial profile of the perpendicular flow Mach number during the Ohmic phase of the discharge (black line), 1.0 ms after the TH pulse (red line) and 1.5 ms after the TH pulse (blue line).

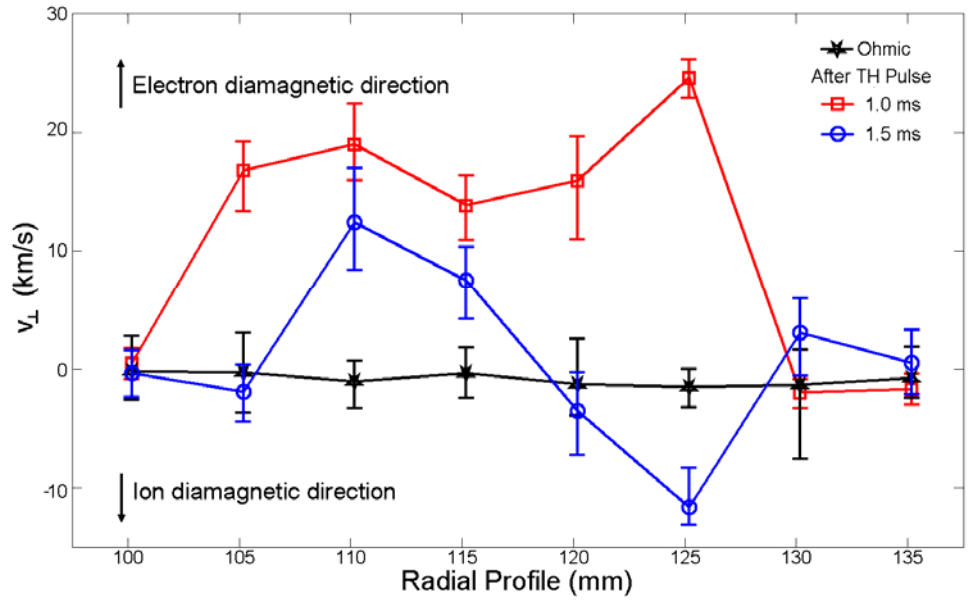

Figure 6.20: Radial profile of the perpendicular flow velocity during the Ohmic phase of the discharge (black line), 1.0 ms after the TH pulse (red line) and 1.5 ms after the TH pulse (blue line).

The evolution of the parallel flow Mach number is shown in Figure 6.21 and the parallel flow velocity in Figure 6.22. Following the TH pulse the radial profile of the parallel flow is significantly altered compared with the profile during the Ohmic phase of the discharge. Initially the flow is accelerated in the direction of the toroidal magnetic field with the flow at all positions inside of r = 115 mm reversing direction. At 100 mm the flow becomes nearly sonic ($M_{||} \approx 0.75$) 1.0 ms after the TH pulse. By 1.5 ms after the TH pulse the parallel flow begins to return to the profile it had during the Ohmic phase of the discharge.

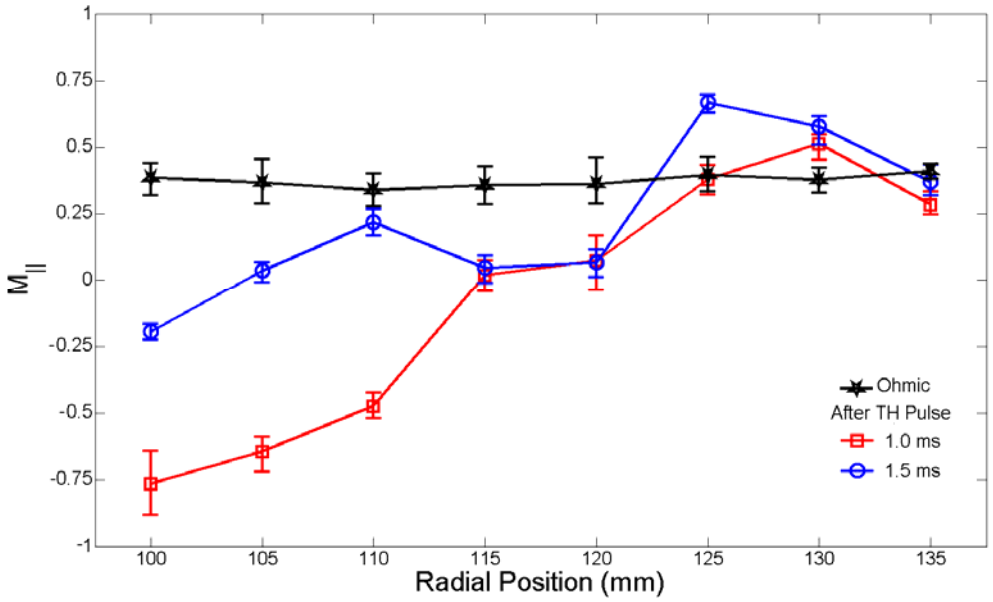

Figure 6.21: Radial profile of the parallel flow Mach number during the Ohmic phase of the discharge (black line), 1.0 ms after the TH pulse (red line) and 1.5 ms after the TH pulse (blue line).

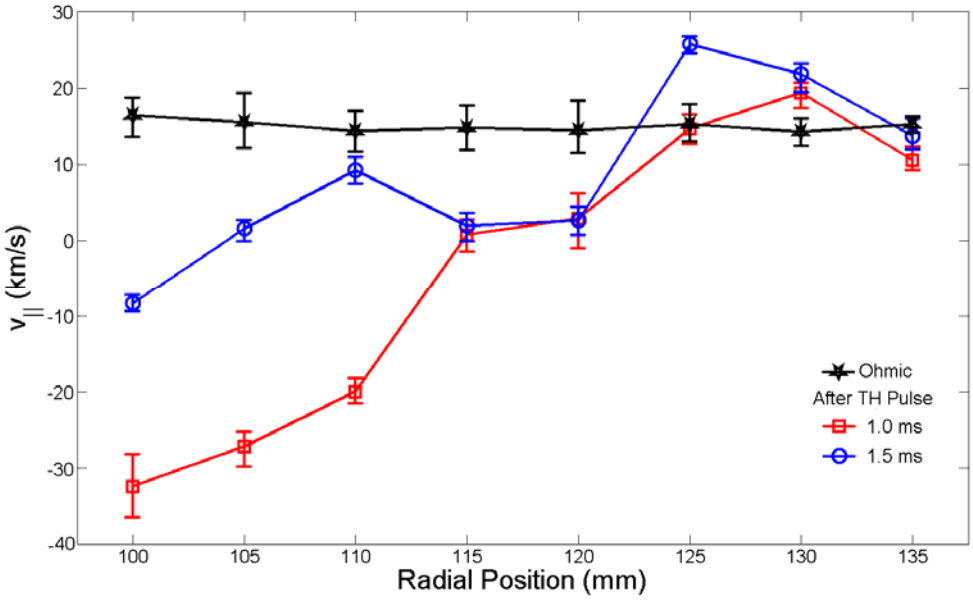

Figure 6.22: Radial profile of the parallel flow velocity during the Ohmic phase of the discharge (black line), 1.0 ms after the TH pulse (red line) and 1.5 ms after the TH pulse (blue line).

H-mode induced by turbulent heating has also been observed on the HT-6M tokamak [119]. The results from HT-6M qualitatively agree with the observations on STOR-M, notably an enhancement in the sheared radial electric field and poloidal flow. Observations on HT-6M also indicate that a radially sheared Reynolds stress may be the dominant mechanism in the formation of the poloidal flow and E_r shear [88].

6.5 Electrode Biasing

The observation of significant modifications to the plasma potential and radial electric field during H-mode on many machines led to the idea of directly altering the electric field by means of a biased electrode inserted into the plasma. For the electrode biasing experiments on STOR-M a cylindrical stainless steel electrode is positioned between minor radii of r = 82 mm and 105 mm. For positive biasing experiments the capacitor bank is charged to +500 V. For experiments with negative biasing no changes in the plasma parameters are observed. The bias was applied to the electrode 12.5 ms after the initiation of the discharge. The typical discharge parameters (plasma current I_p,

loop voltage V_l, line averaged electron density $\overline{n}_e$, horizontal displacement ΔH, H_α emission and electrode current I_b) for a discharge with +500 V electrode biasing are shown in Figure 6.23 .

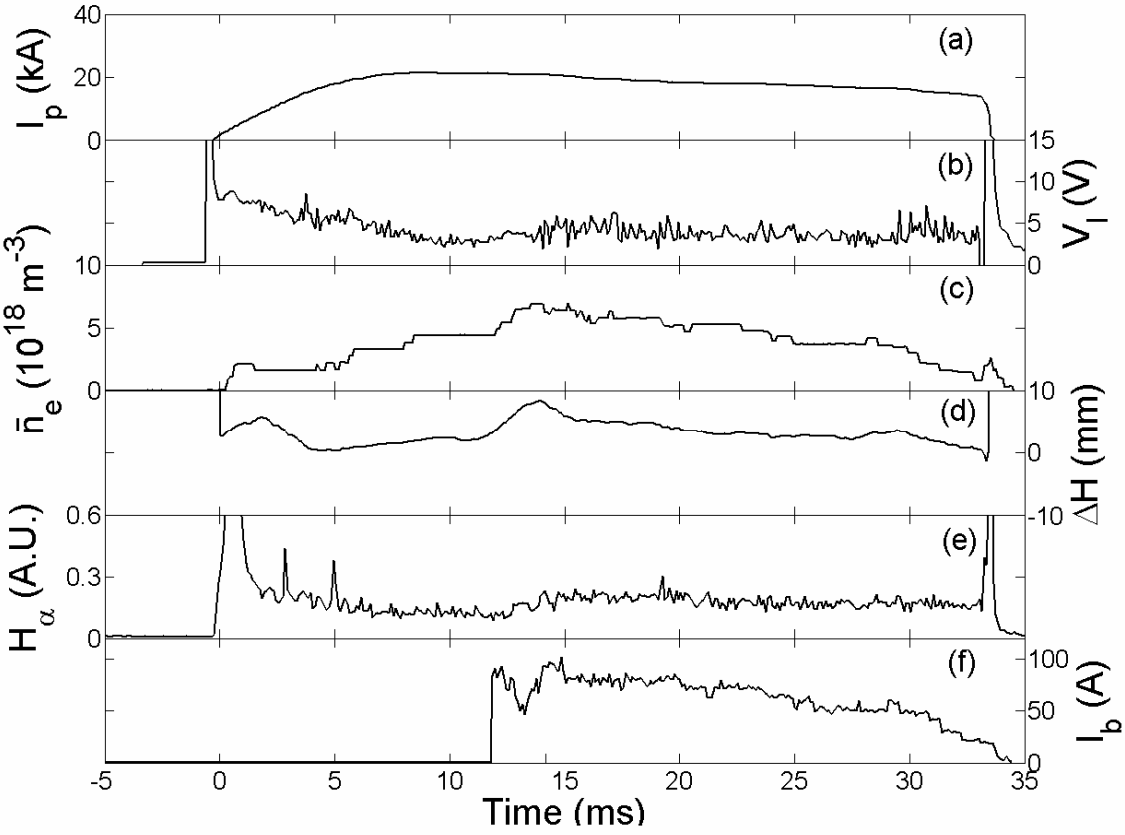

Figure 6.23: Waveforms of a typical discharge with +500 V electrode biasing applied at 12.5 ms. (a) Plasma Current. (b) Loop voltage. (c) Line averaged density. (d) Horizontal displacement. (e) H_α emission. (f) Electrode biasing current.

During the electrode biasing phase the loop voltage increases from 3 V to 5 V. The plasma density increases by 50% to 6.9 × 10^{18} m^{-3} indicating an improvement in particle confinement. H_α emission increases by about 70% during the electrode biasing phase which indicates an increase in edge recycling during the biasing phase. The biasing electrode draws approximately 82 A of current during the initial part of the biasing phase. The drawn current begins to decrease with the plasma density toward the end of the discharge.

The plasma resistivity $\eta_{||}$, average electron temperature T_e and energy confinement time τ_E for a discharge with +500 V electrode biasing are shown in Figure 6.24. The plasma resistivity increases from 2.2×10^{-6} Ω·m to 3.2×10^{-6} Ω·m during the biasing phase. The average electron temperature T_e decreases from 210 eV to 150 eV during the biasing phase. The energy confinement time τ_E decreases from about 1 ms during the Ohmic phase to 0.75 ms during the biasing phase. The energy confinement during the biasing phase degrades while the particle confinement improves, as indicated by the increase in the line average density $\overline{n}_e$ (see Figure 6.23c).

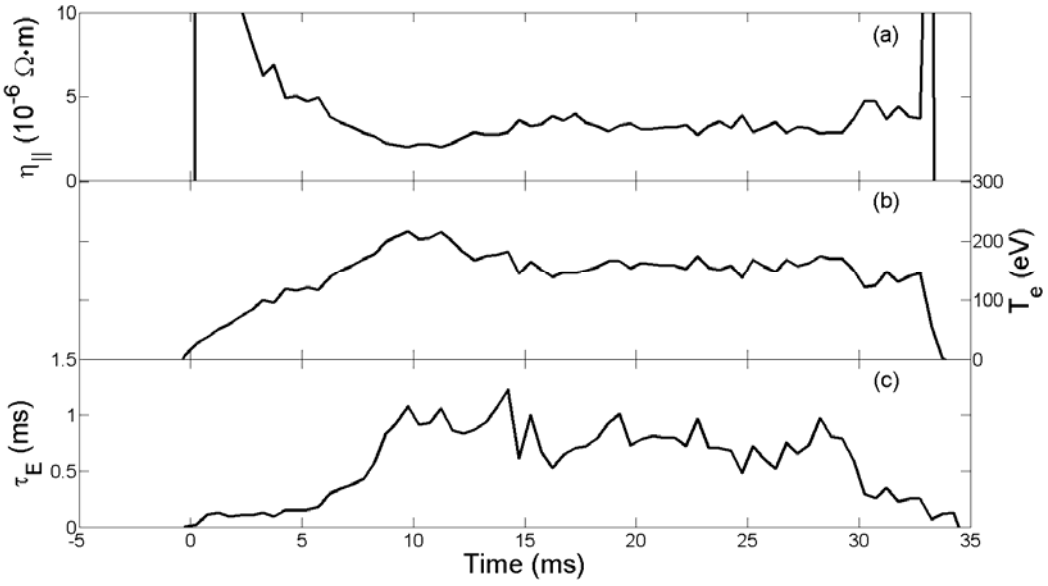

Figure 6.24: Waveforms of (a) parallel plasma resistivity, (b) average electron temperature, and (c) energy confinement time during a discharge with +500 V electrode biasing applied at 12.5 ms.

During the biasing phase the edge density (Figure 6.25) increases mildly compared with the edge density increase observed with the application of a 12 kA TH pulse. The edge density increase is between 20% and 30% in the range over which the edge density is measured. The line averaged density increase is larger during the +500 V biasing phase indicating that most of the density increase must occur inside of r = 110 mm.

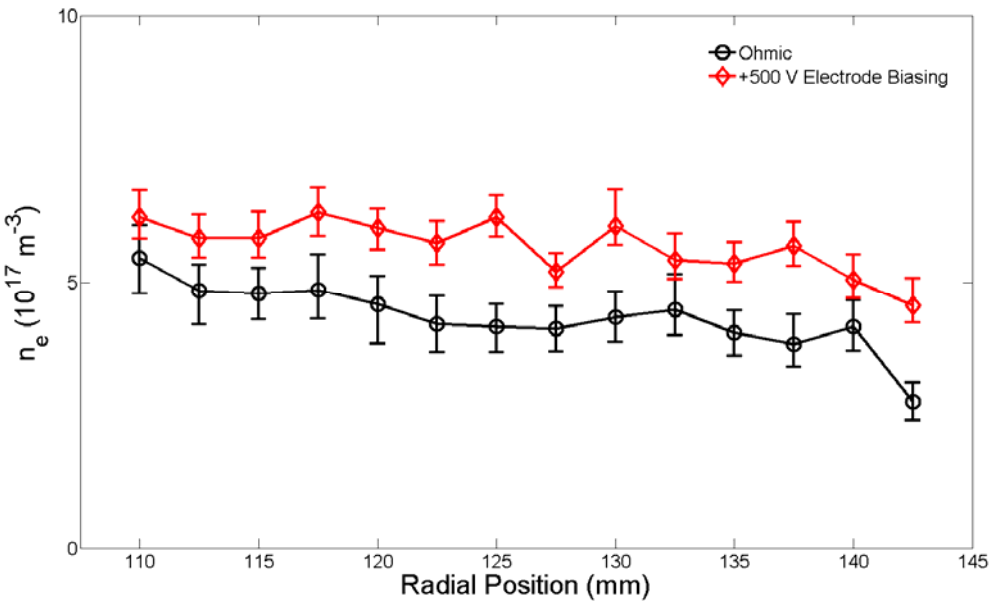

Figure 6.25: Radial profile of the edge electron density during the Ohmic phase of the discharge (black line) and during the biasing phase (red line) .

Figure 6.26 shows the floating potential V_f, plasma potential V_p and radial electric field E_r during both the Ohmic and biasing phases. During the biasing phase the plasma floating potential V_f is significantly perturbed. Figure 6.26a shows that the floating potential at r = 110 mm increases from -33 V during the Ohmic phase to 85 V during the electrode biasing phase and from -5 V to 58 V at r = 127.5 mm. The plasma potential V_p (Figure 6.26b), estimated from the floating potential and the electron temperature also shows significant alteration during the biasing phase. Figure 6.26c shows the electric field E_r, estimated from the plasma potential during both the Ohmic and biasing phases. The electric field is significantly modified during the biasing phase. Rather than having a negative well between 115 and 120 mm, the electric field is positive throughout the plasma edge taking a value of ~3 kV/m at all points except at r = 123.75 where there is a slight dip. The modified electric field indicates that the flow profile in the plasma edge may also be modified during the biasing phase.

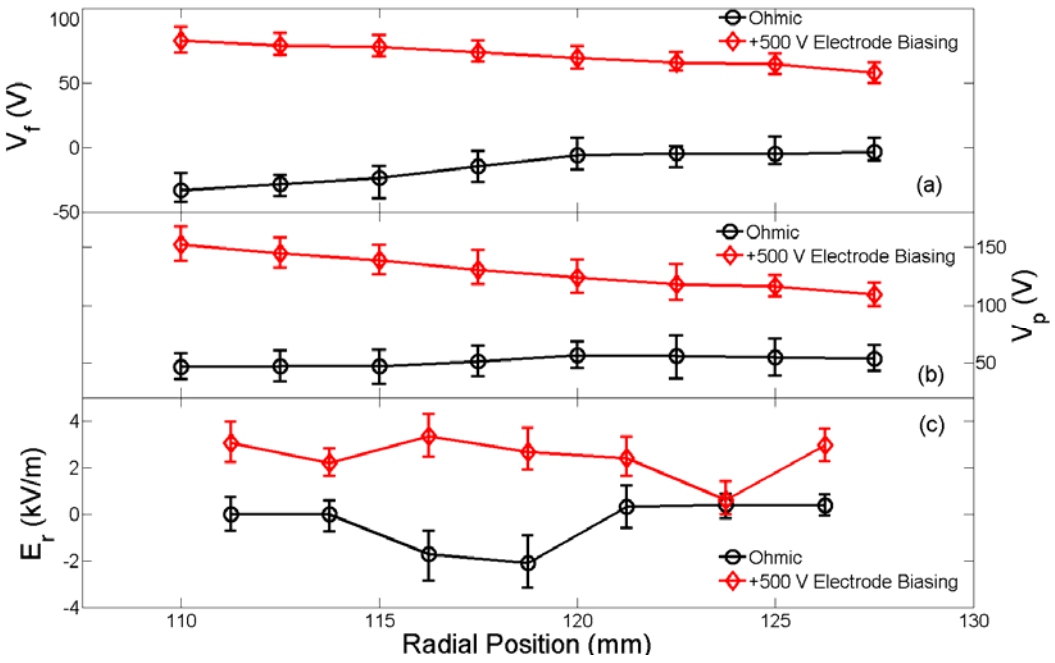

Figure 6.26: The radial profile of the (a) floating potential, (b) plasma potential and (c) radial electric field. The black lines indicate the profiles during the Ohmic phase and the red lines indicate the profiles during the biasing phase.

The parallel and perpendicular Mach number profiles are shown in Figure 6.27 for both the Ohmic and biasing phases. The velocity profiles are shown in Figure 6.28. During the biasing phase the parallel flow velocity (Figure 6.28a) is reduced but maintains a similar profile shape. This reduction could be at least qualitatively explained by a contribution due to the $E_r \times B_\theta$ velocity which is in the direction of B_ϕ. At r = 100 mm the parallel flow velocity is reduced from 15 km/s to 7.5 km/s. The perpendicular flow velocity profile is also modified during the biasing phase. The perpendicular flow velocity increases from an approximately constant value of -8 km/s between r = 100 mm and 120 mm to 13 km/s at r = 135 mm.

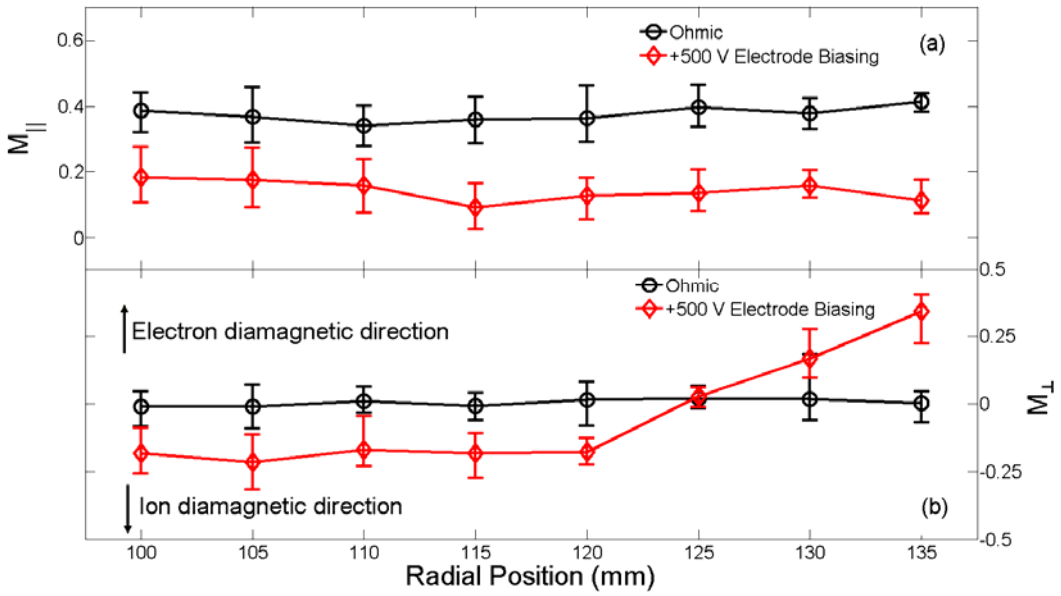

Figure 6.27: The radial profiles of (a) the perpendicular flow Mach number and (b) the parallel flow Mach number. The black lines indicate the profiles during the Ohmic phase of the discharge and the red lines indicate the profiles during the biasing phase.

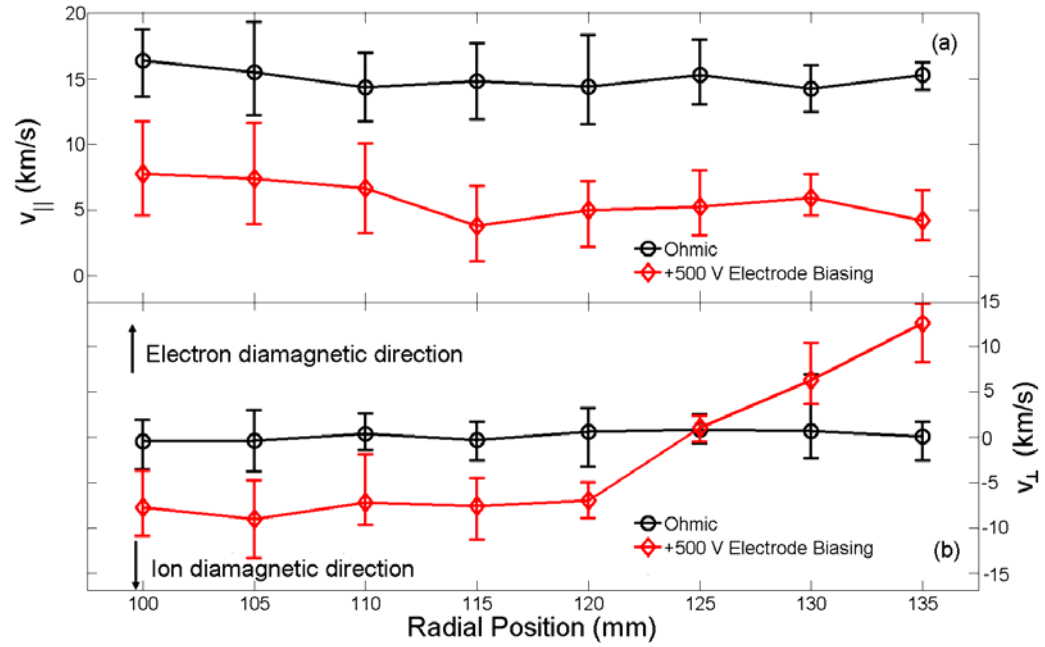

Figure 6.28: The radial profiles of (a) the perpendicular flow velocity and (b) the parallel flow velocity. The black lines indicate the profiles during the Ohmic phase of the discharge and the red lines indicate the profiles during the biasing phase.

Observations during the +500 V electrode biasing experiments indicate that several of the characteristics of H-mode are induced, while others are not. The line averaged density shows a significant increase, as does the edge electron density, however the loop voltage and H_α emission increase during the electrode biasing phase. This indicates that while the particle confinement time appears to increase, the energy confinement time actually decreases.

6.6 Results from CASTOR Tokamak

CASTOR (Czech Academy of Sciences Torus) is a relatively small tokamak. It has a major radius of 40 cm and a minor radius (limiter radius) of 85 mm. The plasma parameters for these experiments were toroidal magnetic field $B_\phi \approx 1.0$ T, plasma current $I_p \approx 10$ kA, loop voltage $V_l \approx 2.5$ V, line-averaged electron density $n_e \sim 1 \times 10^{19}$ m^{-3} and a discharge duration $t_d \approx 25$ ms. CASTOR was operated in two regimes: with and without electrode biasing. The biasing electrode is a mushroom-shaped graphite electrode with a surface area of 27 cm^2 and is biased relative to the vacuum vessel. The typically biasing voltage for these experiments was +100 V, applied between 15 ms and 20 ms during the discharge with the electrode positioned at a minor radius of 50 mm. Electrode biasing was also carried out at +150 V and +200 V, however not all of the diagnostics were used at these voltages.

CASTOR is equipped with a variety of diagnostic probes. These include an 8 collector Gundestrup probe with round collecting surfaces, a rake probe with two rows of 12 pins and a poloidal probe ring consisting of 96 Langmuir probe tips, 16 Mirnov coils and 16 Hall sensors. There are additional diagnostics such as a bolometer and reflectometer which are not used in this analysis.

Measurements were made during the normal Ohmic and electrode biasing discharges on CASTOR. The main plasma parameters for bias voltages of +100 V, +150 V and +200 V are shown in Figure 6.29, Figure 6.30 and Figure 6.31, respectively. In these figures, the time evolution of the plasma current, loop voltage, line averaged plasma density, biasing voltage and biasing current are shown. It is observed that with all biasing voltages the density increases during the biasing phase. The density increases throughout the biasing phase and this increase is more rapid, and hence larger for larger

biasing voltages. For +100 V biasing the density increase is only sufficient to hold the density constant during the biasing phase when it would otherwise be decreasing (see Figure 6.29). The density at the end of biasing phase during +150 V biasing is ~1.1 times the density at the beginning of the biasing phase (see Figure 6.30). For +200 V biasing the density increases to ~1.75 times the density at the start of the biasing phase (see Figure 6.31). In all cases the density begins decreasing rapidly at the end of the biasing phase. The current drawn by the electrode during biasing is about -9.3 A for +100 V biasing, -10.8 A for +150 V biasing and -11.2 A for +200 V biasing and remains almost constant during the biasing phase. There is an increase in the H_α emission during the biasing phase which is larger for larger biasing voltages. After the biasing phase the H_α emission returns to the level it held without biasing.

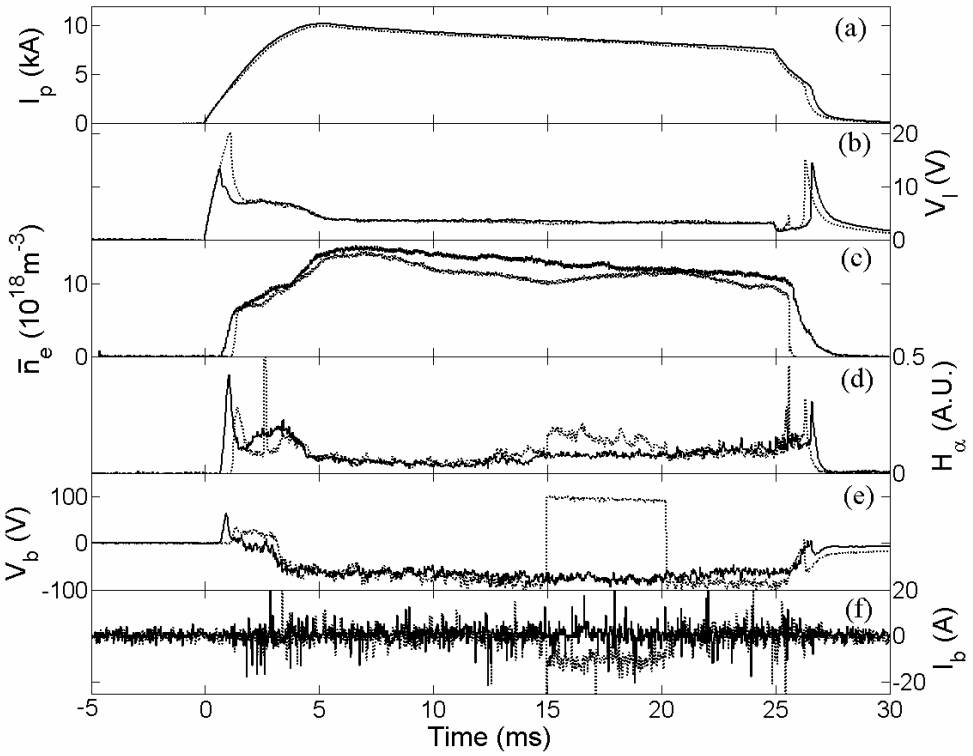

Figure 6.29: Comparison of the main discharge parameters on CASTOR during a normal Ohmic discharge (solid line) and a discharge with +100 V biasing with the biasing electrode at r = 50 mm between 15 and 20 ms (dashed line). (a) Plasma current; (b) loop voltage; (c) line average density; (d) H_α emission; (e) biasing electrode voltage; and (f) biasing electrode current.

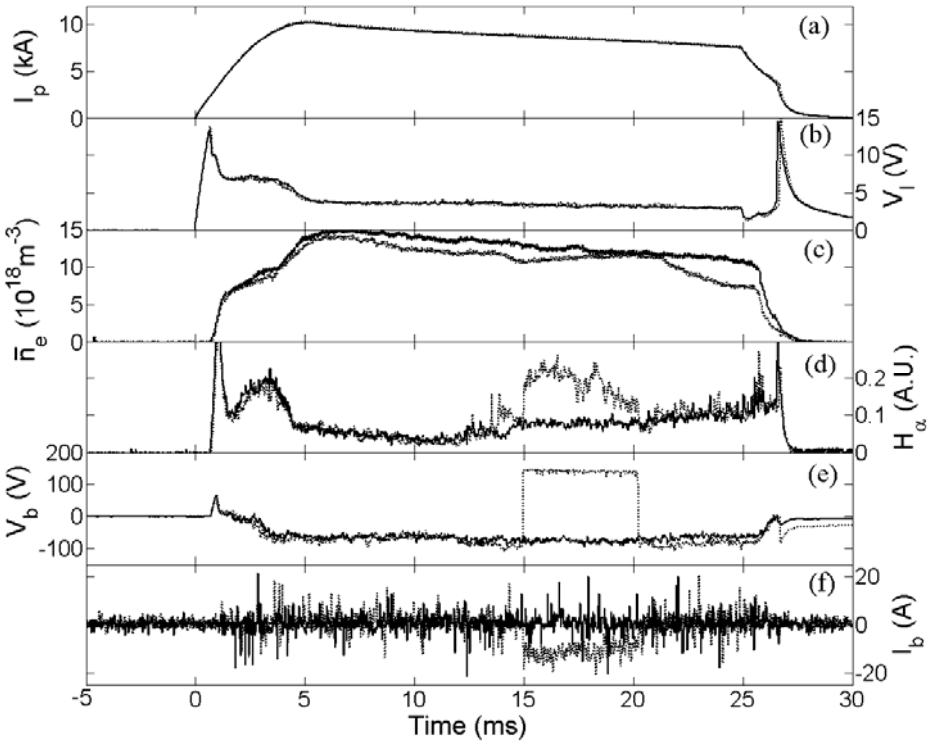

Figure 6.30: Comparison of the main discharge parameters on CASTOR during a normal Ohmic discharge (solid line) and a discharge with +150 V biasing with the biasing electrode at r = 50 mm between 15 and 20 ms (dashed line). (a) Plasma current; (b) loop voltage; (c) line average density; (d) H_α emission; (e) biasing electrode voltage; and (f) biasing electrode current.

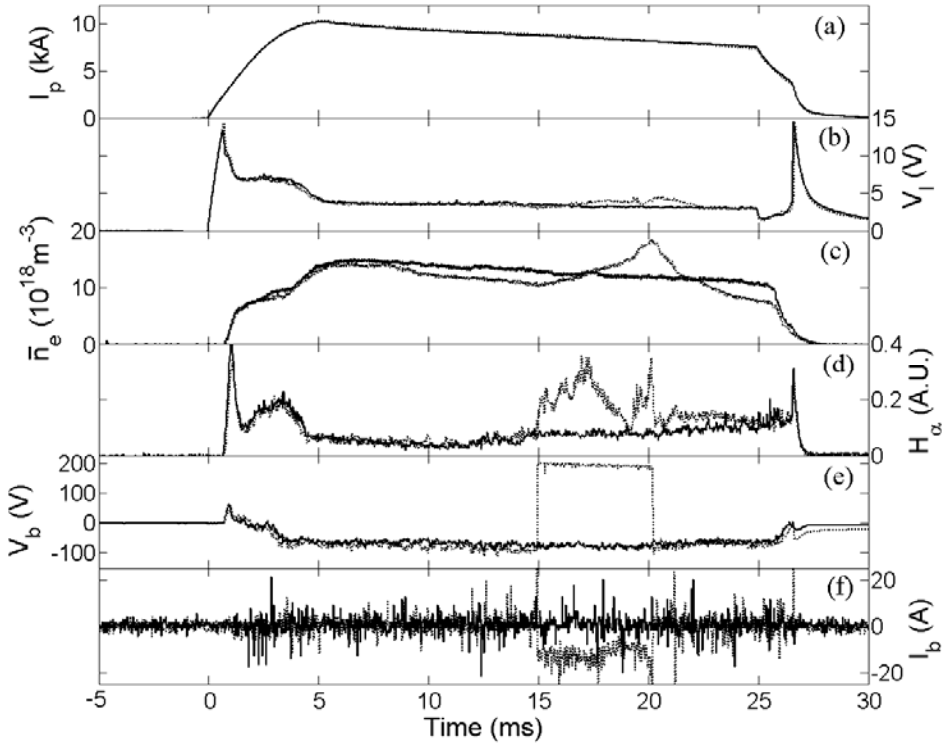

Figure 6.31: Comparison of the main discharge parameters on CASTOR during a normal Ohmic discharge (solid line) and a discharge with +200 V biasing with the biasing electrode at r = 50 mm between 15 and 20 ms (dashed line). (a) Plasma current; (b) loop voltage; (c) line average density; (d) H_α emission; (e) biasing electrode voltage; and (f) biasing electrode current.

Figure 6.32a shows the electron temperature during discharges with +100 V and +200 V electrode biasing. Both discharges show a decrease in the electron temperature during the biasing phase from the 90 eV temperature during the Ohmic phases of the discharges. The discharge with +100 V electrode biasing shows only a small temperature reduction of 5 eV to 85 eV. The discharge with +200 V electrode biasing shows a more significant reduction of the electron temperature to 79 eV. Following the termination of the electrode bias the temperature during the discharge with +200 V electrode biasing drops further to 71 eV. Several milliseconds after the termination of the electrode bias the electron temperature begins to return to the temperature held prior to the application of the bias. The energy confinement time (shown in Figure 6.32b) appears to increases mildly from 1.0 ms during the Ohmic phase to 1.2 ms during the +100 V biasing phase which is maintained after the termination of the bias until the end of the discharge.

During the +200 V biasing phase the confinement time initially falls to 0.85 ms but then begins to increase up to 1.4 ms by the end of the biasing phases. After the termination of the bias the confinement time falls to 0.8 ms but recovers to the Ohmic value of 1 ms before the end of the discharge.

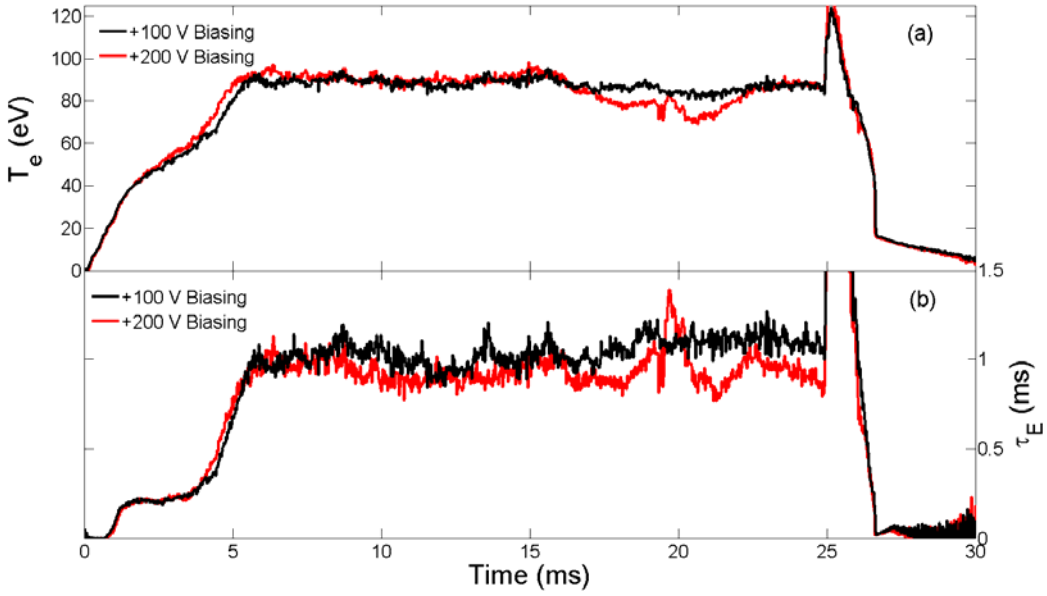

Figure 6.32: Comparison of the (a) electron temperature and (b) energy confinement time for a discharge with +100 V electrode biasing (black line) and with +200 V biasing (red line) between 15 and 20 ms.

The radial profile of the floating potential, electric field and edge density are measured using a rake probe. The floating potential and electric field are measured by floating the probe tips with respect to the vacuum chamber and measuring the voltage difference between the tips and the chamber. The measurement of the edge density requires operating the rake probe in two modes: swept mode and ion saturation mode. In the swept mode a sawtooth voltage (500 Hz ,75 V amplitude, -35 V DC offset) is applied to the probe tips and the current drawn by the probes is measured and the I-V characteristic is obtained. The electron temperature is determined by fitting the I-V characteristic curve with an exponential function. The radial profile of the electron temperature is shown in Figure 6.36. In ion saturation mode the tips are biased to -100 V

where they collect the ion saturation current. By knowing the value of the ion saturation current, the electron temperature in the vicinity of the probe and the surface area of the probe tip the plasma density can be determined.

In Figure 6.33 the radial profiles of the floating potential measured at different biasing voltages are shown. Without biasing (V_b = 0 V), the plasma floating potential is near zero outside the limiter (r > 85 mm) and has a slight positive bump in the vicinity of the limiter, between 80 and 85 mm. Inside of r = 80 mm the floating potential remains constant at about +13 V to about 65 mm at which point it begins to decrease. For the biasing cases the profile is similar to the unbiased case for r > 80 mm, but inside of that position they increase dramatically compared with the unbiased case. For +100 V electrode biasing the floating potential increases up to about +105 V at r = 60 mm. For +150 V biasing the floating potential increases up to +130 V at r = 65 mm and up to about +165 V for the +200 V biasing.

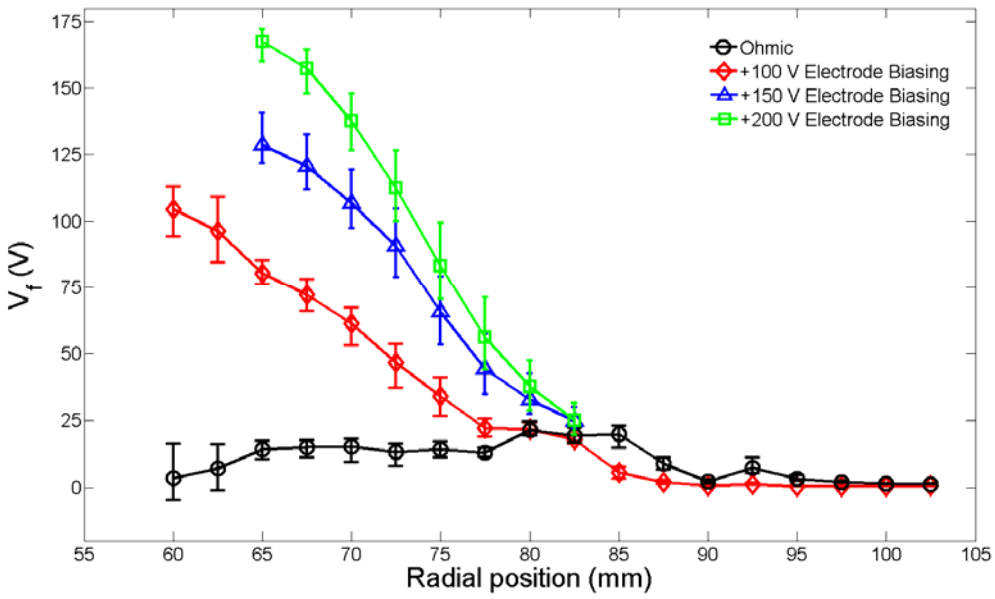

Figure 6.33: Radial profile of the floating potential during a normal Ohmic discharge (black line) and during electrode biasing for biasing voltages of +100 V (red line), +150 V (blue line) and +200 V (blue line).

The profiles of the radial electric field are shown in Figure 6.34. For the unbiased case, the electric field is positive in the scrape-off layer and increases up to the limiter position and then begins to decrease becoming about -2 kV/m at r = 60 mm. For the biasing cases the electric field remains positive throughout the measured range. For +100 V biasing the electric field increase continuously inward to about r = 64 mm where it takes a value of 6 kV/m and then begins to decrease. The electric fields for +150 V and +200 V electrode biasing peak at 72 mm at 9.5 kV/m and 11 kV/m respectively.

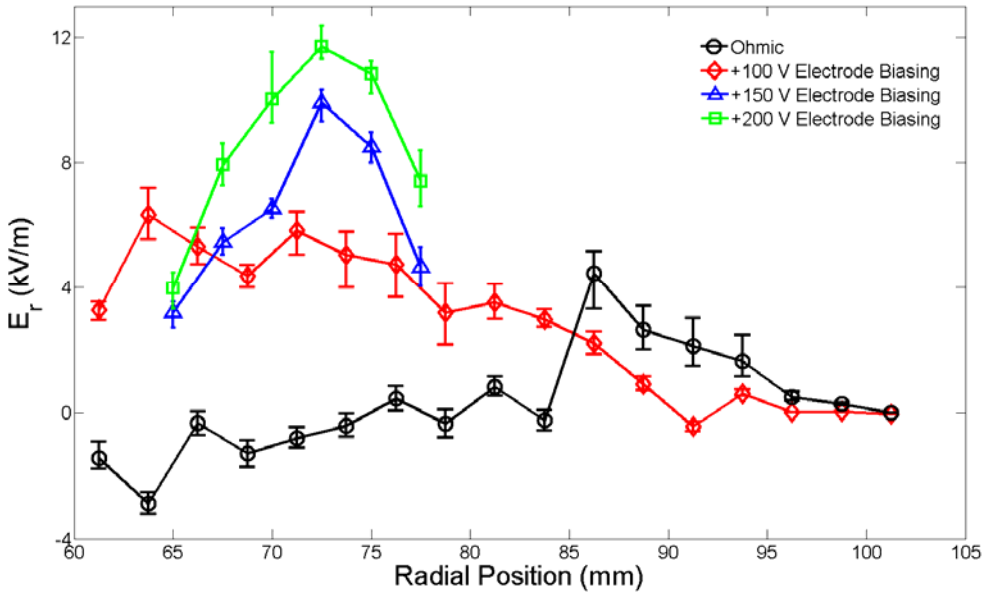

Figure 6.34: Radial profile of the radial electric field during a normal Ohmic discharge (black line) and during electrode biasing for biasing voltages of +100 V (red line)), +150 V (blue line) and +200 V (blue line).

The temperature profile, inferred by fitting the I-V curve obtained by sweeping the voltage on the probe tips, is shown in Figure 6.36. An example of the fitting is shown in Figure 6.35 for T_e = 17.5 eV. This profile is used to determine the edge plasma density which is measured using the rake probe tips to collect ion saturation current.

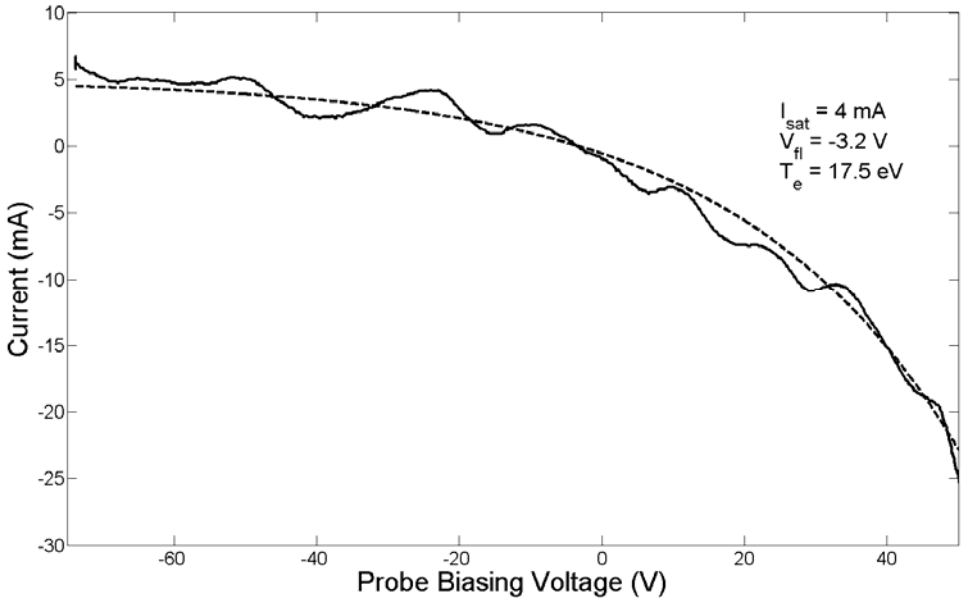

Figure 6.35: Fitting of the I-V characteristic measured with the rake probe (solid line) with a model I-V curve (dashed line). Parameters for the fitted line are shown.

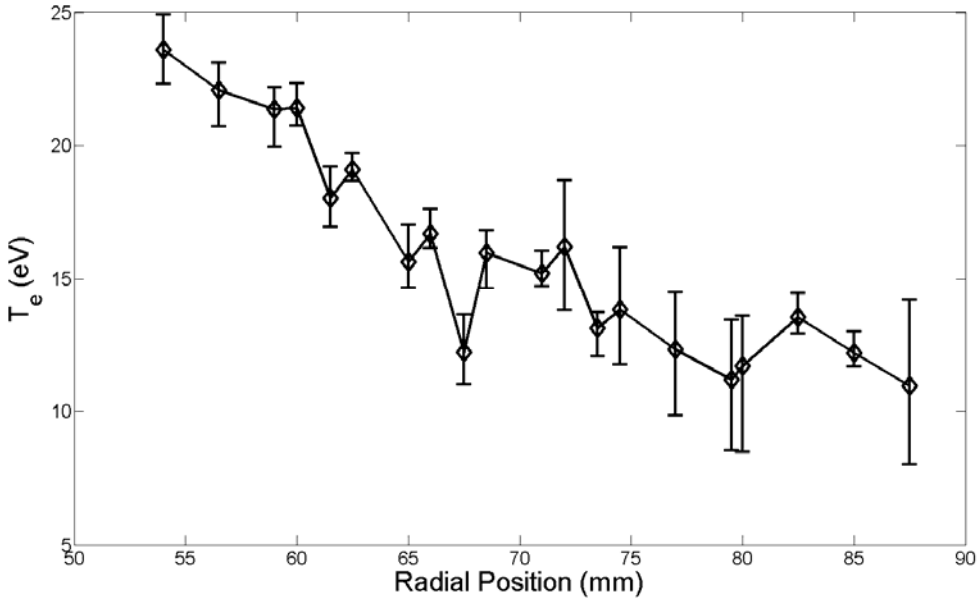

Figure 6.36: Radial profile of the electron temperature inferred from the fitting of the I-V characteristic measured with the rake probe.

The edge plasma density for the unbiased case and for +100 V electrode biasing is shown in Figure 6.37. At all radial locations the density is larger during the biasing phase. The plasma density is about 2.5 times larger at $r = 60$ mm during electrode biasing than during the Ohmic discharge.

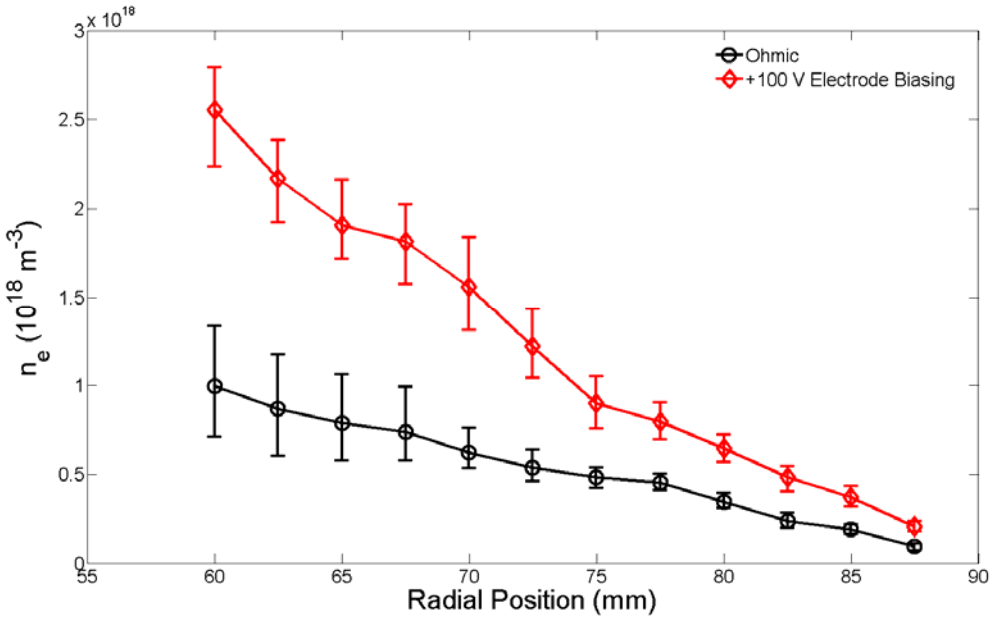

Figure 6.37: Comparison of the edge electron density during normal Ohmic mode (black line) and during +100 V electrode biasing (red line).

The plasma flow velocity in the edge of CASTOR was measured with an 8 collector Gundestrup probe. The collectors were oriented such that none of the collectors faced perpendicular to the magnetic field (Figure 6.38), avoiding the region in which the model of Van Goubergen is invalid [95]. The raw signals acquired by the 8 collectors are shown in Figure 6.39.

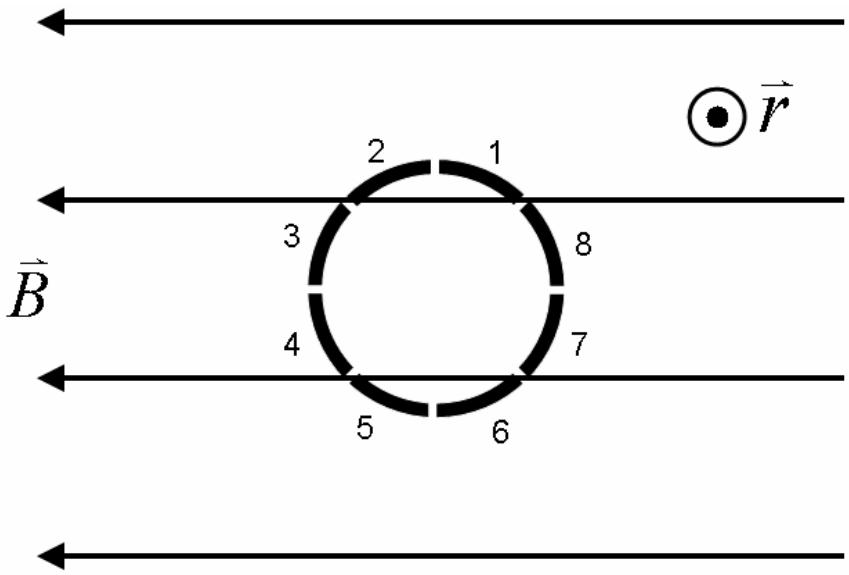

Figure 6.38: Orientation of the Gundestrup probe collectors on CASTOR tokamak relative to the toroidal magnetic field as viewed from the outside of the vacuum chamber.

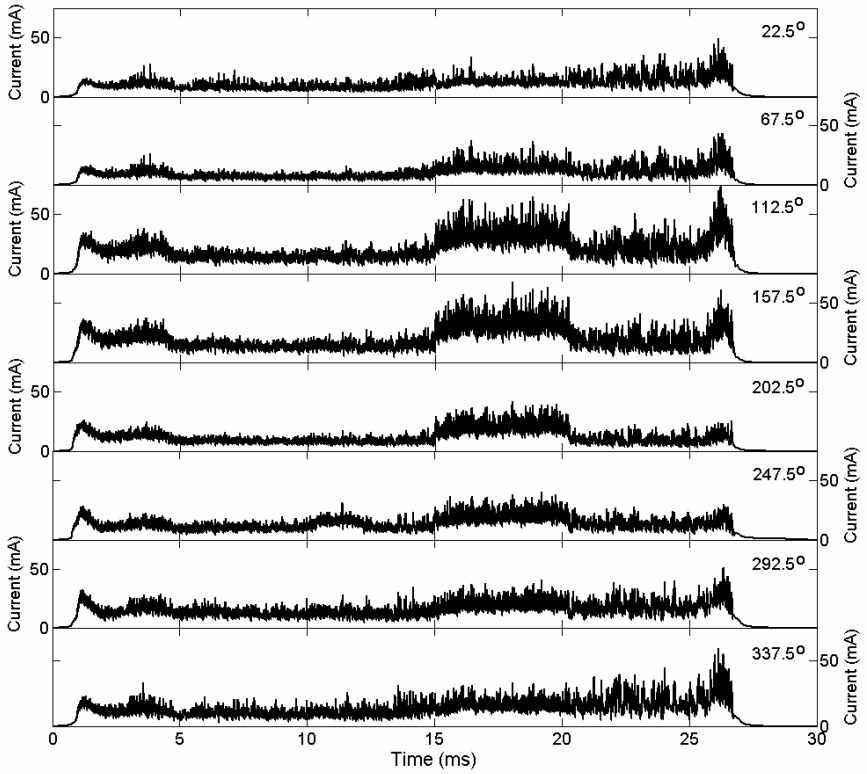

Figure 6.39: The ion saturation current collected by the eight collectors of the Gundestrup probe on CASTOR for a discharge with +100 V electrode biasing between 15 and 20 ms.

The radial profiles of the parallel flow without biasing and with +100 V electrode biasing are shown in Figure 6.40. For both the biased and unbiased cases, the parallel flow is in the direction of the magnetic field and plasma current. Without biasing the parallel flow velocity is seen to be largest at r = 60 mm, the innermost position at which it was measured. The flow steadily decreases from 5 km/s at r = 60 mm until there is virtually no flow at the limiter position. For the biased case, the parallel flow velocity is about twice as large at r = 60 mm (10 km/s) and increases slightly to 13 km/s at r = 67.5 mm and then begins to slowly decrease to 11.5 km/s at r = 77.5 mm. The flow then abruptly decreases to 2.5 km/s at r = 80 mm and decreases further to 1.5 km/s at the limiter position.

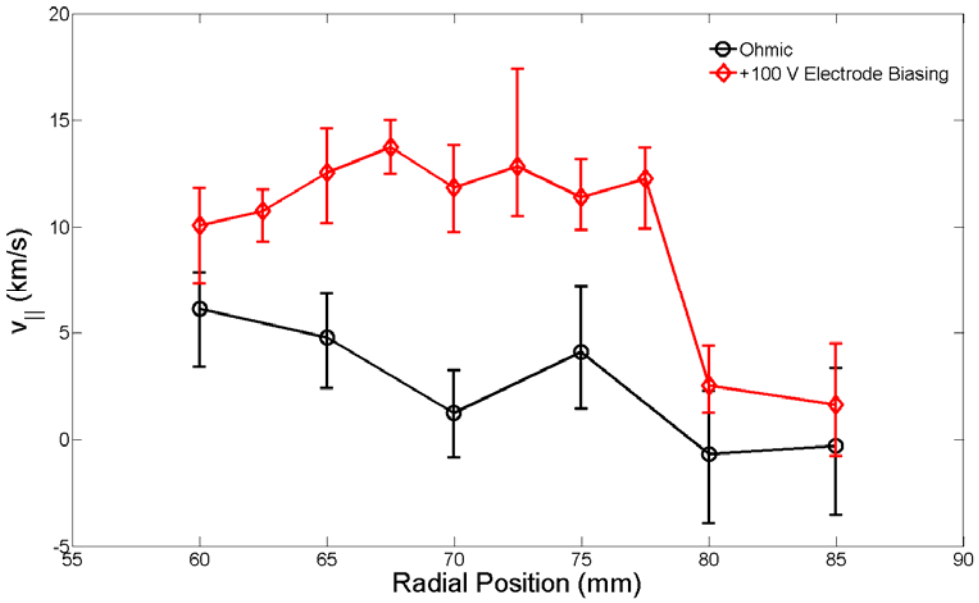

Figure 6.40: Comparison of the radial profile of the parallel flow velocity for the normal Ohmic mode (black line) and with +100 V electrode biasing (red line).

Figure 6.41 shows the radial profiles of the perpendicular flow without biasing and with +100 V electrode biasing. For the unbiased case, the perpendicular flow is -5 km/s at r = 60 mm, which corresponds to a flow in the electron diamagnetic drift direction. The flow velocity increases and becomes zero at r = 65 mm. The flow velocity continues to increase up to about 4 km/s at r = 80 mm and decreases slightly to 2

km/s at the limiter position. For the biased case, the flow is in the ion diamagnetic drift direction at all radial locations. The flow velocity decreases from 6 km/s at r = 60 mm to 3 km/s at r = 67.5 mm and begins to increase up to 8.5 km/s at r = 80 mm and then decreases to 7 km/s at the limiter position.

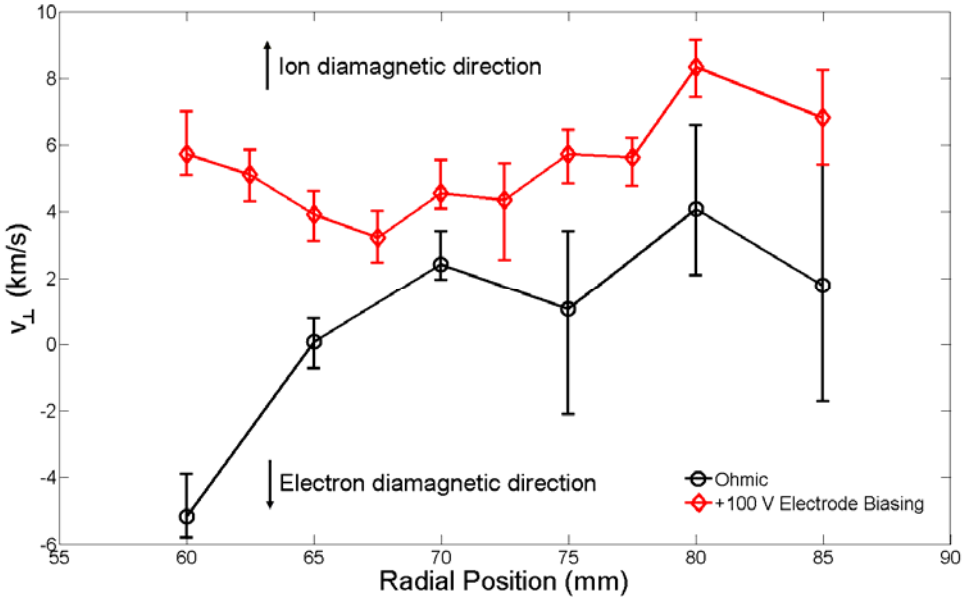

Figure 6.41: Comparison of the radial profile of the perpendicular flow velocity for the normal Ohmic mode (black line) and with +100 V electrode biasing(red line).

The poloidal $\vec{E}\times\vec{B}$ drift during +100 V biasing inferred from the measurement of the radial electric field with the rake probe is shown in Figure 6.42 along with the flow velocity measured by the Gundestrup probe. The two flow velocities agree well for the region between r = 60 mm and 77.5 mm but deviate significantly for the region outside of r = 77.5 mm where the Gundestrup probe measurement shows an increasing flow velocity and the $\vec{E}\times\vec{B}$ drift shows a sharp decrease to less than 1 km/s at r = 78.75 mm followed by an increase up to 2 km/s at the limiter position.

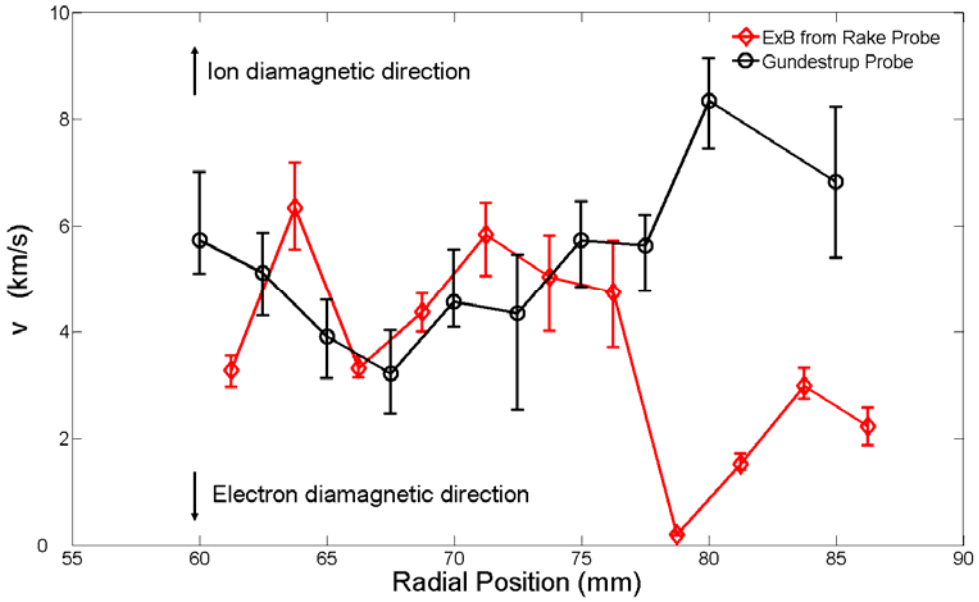

Figure 6.42: Comparison of the radial profile of the perpendicular flow velocity measured with the Gundestrup probe (black line) and inferred from the radial electric field (red line) during +100 V electrode biasing.

The observations on CASTOR are qualitatively similar to those on STOR-M. The electrode biasing phase shows several characteristics of H-mode, notably an increase in the line averaged electron density which indicates an improvement in particle confinement. There is, however, an increase in the H_α emission indicating increased edge recycling, a sign of reduced confinement at the plasma edge. On CASTOR this may be due to the low biasing voltages as H-mode has been observed at higher biasing voltages with larger current drawn by the electrode [120]. The modifications to the flow profile between STOR-M and CASTOR during positive biasing are similar. It is important to note that since B_ϕ is in the opposite direction in CASTOR that for a given E_r, the $\vec{E}_r \times \vec{B}_\phi$ drift direction is opposite to that in STOR-M.

Chapter 7

Summary and Conclusions

7.1 Summary of Current Results

A Gundestrup probe was used to make plasma flow velocity measurements during a series of experiments in STOR-M (normal Ohmic discharges, reversed toroidal magnetic field discharges, turbulent heating discharges and electrode biasing discharges). The measurements were made in the plasma edge between r = 100 mm and 135 mm in 5 mm intervals. The probe head was modified to allow flow measurements further inside the plasma edge by removing the proud tip after it was damaged during initial experiments. Additionally, a 16 pin rake probe and necessary electronics were constructed to provide time correlated measurements of the floating potential and ion saturation current profiles in the plasma edge.

The parallel and perpendicular flows have been measured during four types of discharge modes in the STOR-M tokamak and during two types of discharge modes in the CASTOR tokamak using Gundestrup probes. On the STOR-M tokamak it is observed that the parallel flow velocity shows no dependence on the direction of the toroidal magnetic field relative to the current direction; the parallel flow is always observed to be in the current direction during Ohmic discharges. The perpendicular flow velocity shows at most a weak dependence on the toroidal magnetic field direction, likely due to the reversal of the direction of the $\vec{E}_r \times \vec{B}_\phi$ drift. During the TH induced H-mode a narrow shear layer in the perpendicular velocity develops in the edge region of the plasma. This produces an edge transport barrier, resulting in improved energy and particle confinement, a reduction in magnetic, electrostatic and density fluctuations and a reduction in H_α emission. The parallel flow velocity profile is also significantly

modified, with the flow direction reversing inside the plasma edge and flow velocities as fast as 33 km/s being observed at the innermost observed locations (r = 100 mm). During the electrode biasing discharges it is observed that the perpendicular flow is accelerated in the $\vec{E}_r \times \vec{B}_\phi$ direction with a shear in the flow developing outside of the plasma edge in the SOL ($r > a$). The parallel flow is decelerated during the biasing phase while the flow profile retains a similar shape as during the Ohmic phase of the discharge. It is observed that the particle confinement improves during the biasing phase while the energy confinement is degraded. H_α emission increases during the biasing phase. As such, no H-mode behaviour is observed, though the behaviour of the plasma during the biasing phase is clearly different than during the Ohmic phase.

On the CASTOR tokamak, results similar to those on STOR-M are obtained. During the Ohmic phase of the discharge the parallel flow velocity is observed to be in the current direction inside the plasma edge, though the flow speed is considerable slower than on STOR-M. The perpendicular flow exhibits different behaviour than that observed on STOR-M during normal Ohmic discharges. The perpendicular flow velocity on CASTOR is non-zero everywhere except at r = 65 mm where the perpendicular flow direction reverses, being in the ion diamagnetic drift direction for r > 65 mm and the electron diamagnetic drift direction for r < 65 mm. During the biasing phase of the discharge it is observed that there is an increase in the particle confinement at all biasing voltages (+100 V, +150 V and +200 V), while energy confinement is unaffected at +100 V and +150 V but is degraded at +200 V. It is observed that the H_α emission increases at all biasing voltages. During the biasing phase the parallel flow is accelerated in the current direction at all radial position, the most significant change occurring at r < 77.5 mm. The perpendicular flow is also strongly modified, being accelerated in the ion diamagnetic drift direction at all radial locations. No regions of significant velocity shear are observed. The plasma behaviour during the biasing phase is similar to that observed on STOR-M.

7.2 Conclusions and Recommendations for Future Work

The Gundestrup probe is currently installed on STOR-M and the data analysis software is available to make plasma flow velocity measurements in the edge of the

STOR-M tokamak. The probe can be used for flow measurements during the ongoing experiments on STOR-M. Measurements of the plasma flow velocity during H-mode discharges with both tangential and vertical compact torus injection would be useful in understanding the physics of the interaction between the tokamak plasma and the compact torus plasma. A new biasing electrode with more radially localized geometry may allow H-mode to be achieved using the electrode biasing by creating a stronger shear in E_r and hence in the poloidal flow. Plasma flow velocity measurements during such an H-mode would be useful in determining why the current electrode is ineffective at inducing H-mode and the observation of increased H_α emission during the present electrode biasing experiments. Additionally, the Gundestrup probe's electronics could be modified to allow for integration with the 2.5 MHz NI PCI-6133 data acquisition cards that are now available. This would allow highly time resolved measurements of both the radial electric field and the plasma flow velocity which may allow the causality of L-H transition in STOR-M to be observed.

Additional diagnostic measurements during the L-H transition would also be useful in its understanding. Several systems are available to do this on STOR-M that would require little or no modification. The 2-mm microwave scattering system could be used to measure density fluctuations at positions in STOR-M that are inaccessible to Langmuir probes ($r < \sim 100$ mm). Additional a so-called triple Langmuir probe [37] could be used to make highly time resolved electron temperature measurements in the edge region of the plasma during the L-H transition and during the subsequent H-mode. A circuit to allow a swept voltage to be applied to the rake probe could be constructed to allow measurements of the profile of the electron temperature. These temperature measurements would make estimates of the plasma potential more accurate and would provide information about modifications to the edge temperature profile during the H-mode.

References

[1] K. Miyamoto, *Plasma Physics for Nuclear Fusion* (The MIT Press, 1987).

[2] J. Wesson, *Tokamaks* (3rd Ed., Clarendon Press, 2004).

[3] K. Niu, *Nuclear Fusion* (Cambridge University Press, 1979)

[4] J.D Lawson, Proc. Phys. Soc. B, **70**, 6 (1957).

[5] JET Press Release (1997)

[6] International Fusion Research Council, *Nucl. Fusion*, **45**, A1 (2005)

[7] T. Fujita, *et. al.*, *Nucl. Fusion*, **39**, 1627 (1999)

[8] B. B. Kadomtsev, *Plasma Phys. Control. Fusion*, **30**, 2031 (1988)

[9] University of Illinois at Chicago Nuclear Issues Briefing Paper No. 69 (June 2005)

[10] F. F. Chen, *Plasma Physics and Controlled Fusion* (2nd Ed., Plenum Press, 1984)

[11] F. F. Chen, *Plasma Physics and Controlled Fusion* (1st Ed., Plenum Press, 1974)

[12] D. L. Jassby, *Nucl. Fusion*, **17**, 309 (1977)

[13] V. E Golant, and V. I. Fedorov, *RF Plasma Heating in Toroidal Fusion Devices* (Consultants Bureau, 1989)

[14] J.W Connor, and H.R. Wilson, Plasma Phys. Control. Fusion, **36**, 719 (1994).

[15] J. G. Cordey, *et. al.*, *Nucl. Fusion*, **45**, 1078 (2005)

[16] Annual Report of the EURATOM/UKAEA Fusion Programme 2003/04 (June 2004)

[17] F. Wagner *et. al*, *Phys. Rev. Lett.*, **49**, 1408 (1982)

[18] C.M. Greenfield, D.P. Schissel, B.W Stallard *et al.*, Phys. Plasmas **4**, 1596 (1997).

[19] ITER Organization: *http://www.iter.org*

[20] K.H. Burrell, *Phys. Plasmas*, **6**, 4418 (1999)

[21] R. J. Groebner, K. H. Burrell, and R. P. Seraydarian, *Phys. Rev. Lett.*, **64**, 3015 (1990)

[22] S. Jachmich, G. Van Oost, R. R. Weynants, and J. A. Boedo, *Plasma Phys. Control. Fusion*, **40**, 1105 (1998)

[23] J. Gunn, J. Stöckel, J. Adamek, I. Duran, J. Horacek, M. Hron, K. Jakubka, L. Kryska, F. Zacek, and G. Van Oost, *Czech. J. Phys.*, **51**, 1001 (2001)

[24] C. C. Petty, M. R. Wade, J. E. Kinsey, D. R. Baker, and T. C. Luce, *Phys. Plasmas*, **9**, 128 (2002)

[25] C. S. MacLatchy, C. Boucher, D. Poirer, and J. P. Gunn, *Rev. Sci. Instrum.*, **63**, 3923 (1992).

[26] W. Zhang, C. Xiao, and A. Hirose, *Phys. Fluids B*, **5**, 3961 (1993)

[27] O. Mitarai, C. Xiao, L. Zhang, D. McColl, W. Zhang, G. Conway, A. Hirose, and H. M. Skarsgard, *Nucl. Fusion*, **36**, 1335 (1996)

[28] C. Xiao, K. K. Jain, W. Zhang, and A. Hirose, *Phys. Plasmas*, **1**, 2291 (1994)

[29] S. Sen, C. Xiao, A. Hirose, and R. A. Cairns, *Phys. Rev. Lett.*, **88**, 185001 (2002)

[30] W. Zhang, *Improved Ohmic Confinement Induced by Turbulent Heating and Electrode Biasing in the STOR-M Tokamak* (PhD. Thesis, University of Saskatchewan, PPL137, 1993)

[31] O. Mitarai, S. W. Wolfe, A. Hirose, and H. M. Skarsgard, *Plasma Phys. Control. Fusion*, **27**, 395 (1985)

[32] G. D. Conway *et al.*, *Progress Report 1995/96* (Plasma Physics Laboratory, University of Saskatchewan, 1996)

[33] M. Enaami-Khonsaari *et al.*, *Plasma Physics Laboratory Report* (Plasma Physics Laboratory University of Saskatchewan, PPL86, 1986)

[34] W. Zhang, C. Xiao, G. D. Conway, O. Mitarai, A. Sarkissian, H. M. Skarsgard, L. Zhang, and A. Hirose, *Phys. Fluids B*, **4**, 3277 (1992)

[35] M. Enaami-Khonsaari, *Modelling and Control of Plasma Position in the STOR-M Tokamak* (PhD. Thesis, University of Saskatchewan, PPL112, 1990)

[36] J. Morelli, *Plasma Position Control in the STOR-M Tokamak: A Fuzzy Logic Approach* (PhD. Thesis, University of Saskatchewan, 2003)

[37] I. H. Hutchinson, *Principles of Plasma Diagnostics* (2nd Ed., Cambridge University Press, 2002)

[38] F. F. Chen, *Lecture Notes on Langmuir Probe Diagnostics*, IEEE-ICOPS Meeting (2003)

[39] N. Hershkowitz, in *Plasma Diagnostics, Discharge Parameters and Chemistry*, edited by O. Auciello and D. L. Flamm (Academic Press, 1989) Vol. 1

[40] R. J. Goldston, *Plasma Phys. Control. Fusion,* **26**, 87 (1984)

[41] The TFTR Group, *Phys. Plasmas*, **2**, 2366 (1995)

[42] M. Malacarne ,C Ripwell, P. A. Duppurex, A. W. Edwards, R. D. Gill, R. S. Granetz, F. Simonet, J. Snipes, and A. Weller, *Plasma Phys. Control. Fusion*, **29**, 1675 (1987)

[43] The JT-60 Team, *Plasma Phys. Control Fusion,* **30**, 1405 (1988)

[44] F. Wagner *et al.*, *Phys. Plasmas*, **12**, 072509 (2005)

[45] T. Fukuda *et al.*, *Nucl. Fusion*, **37**, 1199 (1997)

[46] W. Zhang, C. Xiao, G. D. Conway, O. Mitarai, A. Sarkissian, H. M. Skarsgard, L. Zhang, and A. Hirose, *Phys. Fluids B*, **4**, 3277 (1992)

[47] I. H. Hutchinson, R. S. Granetz, A. Hubbard, J. A. Snipes, T. Sunn Pederson, M. Greenwald, B. LaBombard, and the Alcator Group, *Plasma Phys. Control. Fusion*, **41**, A609 (1999)

[48] Y. Xu, C.-X., Yu, *Phys. Plasmas*, **5**, 2317 (1998)

[49] R. J. Taylor, M. L. Brown, B. D. Fried, H. Grote, J. R. Liberati, G. J. Morales, and P. Pribyl, *Phys. Rev. Lett.*, **63**, 2365 (1989)

[50] R. R. Weynants, *et. al.*, *Nucl. Fusion*, **32**, 837 (1992)

[51] R. D. Bengston, K. W. Gentle, J. Jancarik, S. S. Medley, P. Nielson, and P. Phillips, *Phys. Fluids*, **18**, 710 (1995)

[52] Y. Nishida, A. Hirose, and H. M Skarsgard, *Phys. Rev. Lett.*, **38**, 653 (1977)

[53] K. Ida, S. Hidekuma, Y. Miura, T. Fujita, M. Mori, K. Hoshino, N. Suzuki, T. Yamauchi and the JFT2-M Group, *Phys. Rev. Lett.*, **65**, 1364 (1990)

[54] R. J. Groebner, K. H. Burrell, and R. P. Seraydarian, *Phys. Rev. Lett.*, **64**, 3015 (1990)

[55] R. J. Taylor, M. L. Brown, B. D. Fried, H. Grote, J. R. Liberati, G. J. Morales, and P. Pribyl, *Phys. Rev. Lett*, **63**, 2365 (1989)

[56] R. R. Weynants, G. Van Oost, *Plasma Phys. Control. Fusion*, **35**, B177 (1993)

[57] T. S. Hahm, and K. H. Burrell, *Phys. Plasmas*, **3**, 427 (1996)

[58] H. Bilgari, P. H. Diamond, and P. W. Terry, *Phys. Fluids B*, 2, 1 (1989)

[59] R. E. Waltz, G. D. Kerbel, J.Milovich, and G. W. Hammett, *Phys. Plasmas*, 2, 2408 (1995)

[60] R. R. Dominguez, and G. M. Staebler, *Phys. Fluids B*, 5, 3876 (1993)

[61] B. A. Carreras, K. Sidikman, P. H. Diamond, P. W. Terry, and L. Garcia, *Phys. Fluids B*, 4, 3115 (1992)

[62] X. H. Wang, P. H. Diamond, and M. N. Rosenbluth, *Phys. Fluids B*, 4, 2402 (1992)

[63] K. H. Burrell, *Phys. Plasmas*, 4, 1499 (1997)

[64] S. Chandrasekhar, *Hydrodynamic and Hydromagnetic Stability*, (Dover, 1981)

[65] E. Kim, and P. H. Diamond, *Phys. Plasmas*, **9**, 4530 (2002)

[66] F. Jenko, W. Dorland, M. Kotschenreuther, and B. N. Rogers, *Phys. Plasmas*, **7**, 1904 (2000)

[67] K. C. Shaing, and E. C. Crume Jr., *Phys. Rev. Lett.*, **63**, 2369 (1989)

[68] A. B. Hassam, T. M. Antonsen Jr., J. F. Drake, and C. S. Liu, *Phys. Rev Lett.*, **66**, 309 (1991)

[69] P. H. Diamond, and Y. –B. Kim, *Phys. Fluids B*, **3**, 1626 (1991)

[70] K. C. Shaing, and E. C. Crume, Jr., *Phys. Rev. Lett.*, **63**, 2369 (1989)

[71] K. C. Shaing, and E. C. Crume, Jr., *Phys. Fluids B*, **2**, 1492 (1989)

[72] K. Avinish, P. K. Kaw, and R. Singh, *Phys. Plasmas*, **4**, 2316 (1997)

[73] M. G. Shats, D. L. Rudakov, B. D. Blackwell, G. G. Borg, R. L. Dewar, S. M. Hamberger, J. Howard, and L. E. Sharp, *Phys. Rev. Lett.*, **77**, 4190 (1996)

[74] K. C. Shaing, A. Y. Aydemir, R. Hiwatari, W. A. Houlberg, Y. Ogawa and M. C. Zarnstorff, *Phys. Rev. Lett.*, **83**, 3840 (1999)

[75] T. E. Stringer, *Phys. Rev. Lett.*, **22**, 770 (1969)

[76] M. N. Rosenbluth, and J. B. Taylor, *Phys. Rev. Lett.*, **23**, 367 (1969)

[77] T. H. Stix, *Phys. Fluids*, **16**, 1260 (1973)

[78] S. P. Hirshman, *Phys. Fluids*, **21**, 224 (1978)

[79] A. B. Hassam, and R. M. Kulsrud, *Phys. Fluids*, **21**, 2271 (1978)

[80] V. A. Vershkov, *J. Nucl. Mater.*, **145-147**, 611 (1987)

[81] A. V. Chankin, *J. Nucl. Mater.*, **162-164**, 208 (1989)

[82] A. B. Hassam, and J. F. Drake, *Phys Fluids B*, **5**, 4022 (1993)

[83] A. G. Peeters, *Phys. Plasmas*, **5**, 2399 (1998)

[84] D. R. McCarthy, J. F. Drake, P. N. Guzdar, and A. B. Hassam, *Phys. Fluids B*, **5**, 1188 (1993)

[85] A. B. Hassam, and T. M. Antonsen, Jr., *Phys. Plasmas*, **1**, 337 (1994)

[86] C. Hidalgo, C. Silva, M. A. Pedrosa, E. Sanchex, H. Fernandes, and C. A. F. Varandas, *Phys. Rev. Lett.*, **83**, 2203 (1999)

[87] M. Vergote, M. Van Schoor, Y. Xu, S. Jachmich, M. Hron, and J. Stöckel, *Czech. J. Phys.*, **55**, 389 (2005)

[88] Y. H. Xu, C. X. Yu, J. R. Luo, J. S. Mao, B. H. Liu, J. G. Li, B. N. Wan, and Y. X. Wan, *Phys. Rev. Lett.*, **84**, 3867 (2000)

[89] I. H. Hutchinson, *Phys. Fluids*, **30**, 3777 (1987)

[90] I. H. Hutchinson, *Phys. Rev. A.*, **37**, 4358 (1988)

[91] I. H. Hutchinson, *Phys. Fluids*, **31**, 2728 (1988)

[92] B. J. Peterson, J. N. Talmadge, D. T. Anderson, F. S. B Anderson and J. L. Shohet, *Rev. Sci. Instrum.*, **65**, 2599 (1994)

[93] V. Antoni, D. Desideri, E. Martines, G. Serianni, and L Tramontin, *Nucl. Fusion*, **36**, 1561 (1996)

[94] R. Back, and R. Bengtson, *Rev. Sci. Instrum.*, **68**, 1 (1997)

[95] H. Van Goubergen, R. R. Weynants, S. Jachmich, M. Van Schoor, G. Van Oost and E. Desoppere, *Plasma Phys. Control. Fusion*, **41**, L17 (1999)

[96] P. C. Stangeby, *Phys. Plasmas*, **2**, 702 (1995)

[97] P. C. Stangeby, A. V. Chankin, *Phys. Plasmas*, **2**, 707 (1995)

[98] I. H. Hutchinson, *Phys. Plasmas*, **3**, 6 (1996)

[99] J. P. Gunn, C. Boucher, P. Devynck, I. Duran, K. Dyabilin, J. Horacek, M. Hron, J. Stöckel, G. Van Oost, H. Van Goubergen, and F. Zacek, *Phys. Plasmas*, **8**, 1995 (2001)

[100]P. Peleman, (private correspondence, 2004)

[101] P. Peleman et al., *29th EPS on Plasma Phys. and Contr. Fusion*, Montreux, ECA 26B, P2.216 (2002)

[102] UHV Design Ltd.: *http://www.uhvdesign.com*

[103] *CRC Handbook of Chemistry and Physics* (82nd Ed. CRC Press, 2001)

[104] Rembar, Molybdenum Technical Info: *http://www.rembar.com/Molybdenum.htm*

[105] General Electric Advanced Ceramics: http://www.advceramics.com

[106] MatWeb Material Property Data : http://www.matweb.com

[107] *Operating Instructions* (Kepco BOP Full Rack Bipolar Power Supply, PPL326, 1999)

[108] *Operating Instructions* (DataRoyal Model F230 Waveform/Sweep Generator, PPL167, 1986)

[109] P. Sicard, C. Boucher, A. Litnovsky, and J-.P, St-Germain, *Rev. Sci. Instrum.*, **76**, 2005 (013505-1)

[110] *Specifications* (Analog Devices 5B40 & 5B41, 2004)

[111] *Specifications* (Analog Devices 5B Series 16 Channel Backplane, 2005)

[112] *Operating Instructions* (LeCroy Model 8212 Data Logger, 1983)

[113] *Operating Instructions* (LeCroy Model 8800A 32 Kilosample Memory Module, 1984)

[114] *Operating Instructions* (LeCroy Model 8901A CAMAC-to-GPIB Interface, 1997)

[115] *Specifications* (Huntington® Rotary/Linear Feedthrough, 2001)

[116]*Data Sheet* (Saint Gobain Ceramics Combat® Boron Nitride Solid Grade AX05, 2005)

[117] *Data Sheet* (National Instruments S Series DAQ, 2005)

[118] H. de Kluiver, N. F. Perepelkin, and A. Hirose, *Phys. Rep.*, **199**, 281 (1991)

[119] Y. Xu, C.-X. Yu, J. R. Luo, J. S. Mao, B. H. Liu, J.G. Lie, Y. F. Liang, Y. X. Ji, and Z. W. Wu, *Phys. Plasmas,* **5**, 2317 (1998)

[120] G. Van Oost, J. P. Gunn, A. Melnikov, J. Stöckel, and M. Tendler, *Czech. J. Phys.*, **51**, 957 (2001)